MICROCOPY RESOLUTION TEST CHART
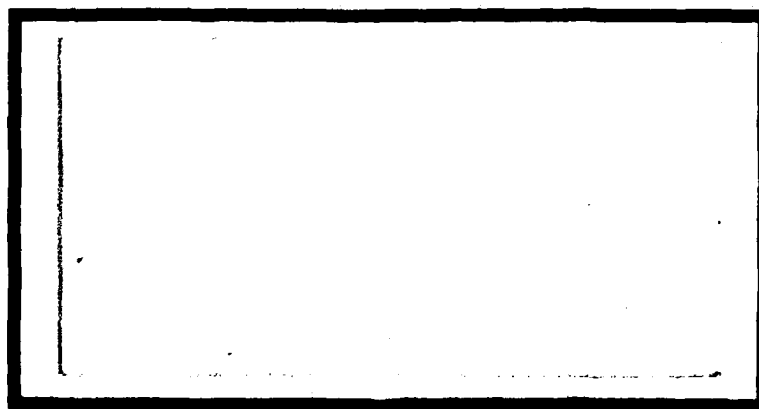
AD A090302

DDC Cy

B.S.

LEVEL II

DTIC
SELECTE
OCT 9 1980
S D

C

UNITED STATES AIR FORCE

AIR UNIVERSITY

AIR FORCE INSTITUTE OF TECHNOLOGY

Wright-Patterson Air Force Base, Ohio

80 9 30 020

AFIT/DS/PH/80-1

LEVEL II

CATHODOLUMINESCENCE CHARACTERIZATION
OF ION IMPLANTED GaAs

DISSERTATION

AFIT/DS/PH/80-1 √

Milton L. Cone
Major   USAF

(14)

CATHODOLUMINESCENCE CHARACTERIZATION

OF ION IMPLANTED GaAs

by

Milton L. Cone B.S., M.S.

Major   USAF

Approved:

Robert L Hengehold	_20 May 1980_
Chairman	
Theodore E Luke	_20 May 1980_
Yoon Soo Park	_21 May 1980_
John Jones Jr	_21 May 1980_
John M Borky	_28 May 1980_

Accepted:

J. S. Przemieniecki   28 May 1980

Dean, School of Engineering

CATHODOLUMINESCENCE CHARACTERIZATION

OF ION IMPLANTED GaAs

DISSERTATION

Presented to the Faculty of the School of Engineering

of the Air Force Institute of Technology

Air University

in Partial Fulfillment of the

Requirements for the Degree of

Doctor of Philosophy

by

Milton L. Cone, B.S., M.S.

Major   USAF

March 1980

Preface

The unique properties of GaAs make it possible to construct integrated circuit devices that are impossible in Si. The Air Force Avionics Laboratory/AADR has been developing this technology for a number of years. The difficulty of introducing dopants by diffusion has lead ion implantation to play an increasing role in the fabrication process. The present production technique for high performance devices is to fabricate large quantities and select those few that meet the desired specifications. Having a nondestructive technique that can be used to characterize the implantation process during fabrication of the device so as to reject faulty device structures can save valuable time as well as money. Depth-resolved cathodoluminescence is a process that can be used for this purpose. This research develops and verifies a model of cathodoluminescence in ion implanted GaAs. This model can now be used as a tool for further study of ion implanted GaAs. This is the first step in developing cathodoluminescence as a tool for deducing the shape of the ion implanted depth profile in semiconductor materials.

I would like to thank my advisor, Dr. R. L. Hengehold, for suggesting the investigation of this area. This advice, support, and prodding throughout this effort are the primary reasons this dissertation was ever completed. I owe a special debt to Drs. Y. S. Park, B. J. Pierce, T. Luke, P. E. Nielsen, and J. Jones, Jr. who came to my rescue at several critical times during the analysis. I am also grateful for the timely and skilled assistance given me by Jim Miskimen, Ron Gabriel and George Gergal of the AFIT physics laboratory staff and for the superb typing by Jill Rueger.

I would also like to give a very special thanks to my wife, Char-
lene, and children, Derrick and Catherine. They sacrificed much more
than I in order to obtain this goal.

Contents

List of Figures

List of Tables

AFIT/DS/PH/80-1

Abstract

Depth-resolved cathodoluminescence was used to study ion implanted
GaAs. This was done in a two step process. First a model for the
luminescence from ion implanted GaAs was developed. This model includes
a detailed Monte Carlo simulation of electrons penetrating into GaAs.
The result of this calculation is a prediction of luminescent intensity
as a function of electron beam energy. This calculation differs from
preceeding ones in that the ion implanted profile is specifically in-
cluded in the analysis. Second, the model was validated by a suitable
experiment that confirms the theoretical predictions.

The luminescence measurements were made on Mg ions implanted into
epitaxial GaAs. Mg was chosen since it had not been previously studied
in epitaxial GaAs.

The results of this research include the identification of many of
the lines in the Mg implanted GaAs spectrum from 1.32 ev to 1.52 ev, a
study of the effect of changing the current of the electron beam on the
spectra and a comparison of the theoretical and experimental luminescence
curves. These results show that changing the current density at the
sample surface dramatically changes the spectra and that good agreement
exists between the theoretical and experimental luminescence curves.

I. Introduction

Overview

There is an increasing emphasis on the use of GaAs as a follow-on to silicon in electronic devices. This has occurred for two reasons. First, some of the properties of GaAs such as a higher mobility and larger band gap allow important improvements (higher frequency and temperature operation) in the performance of classical devices. Second, some of the characteristic features of GaAs give rise to physical phenomena such as a high frequency instability (Gunn effect) and light emission in the visible and IR by carrier recombination. These phenomena have recently been used in such types of devices as microwave oscillators and amplifiers, light emitting diodes, and lasers. The difficulty of introducing dopants into GaAs by diffusion and a desire to use shallower device structures has led to an increasing role for ion implantation as the means for introducing these dopants into GaAs.

This work is important to the U.S. Air Force since it is involved in the use of GaAs as a follow-on to silicon for semiconductor components. The primary interest is in using GaAs in microwave and optoelectronic devices. Having a nondestructive technique that can be used to characterize the semiconductor device "in situ" before further processing can save the Air Force valuable time as well as money.

In order to improve the understanding of the basic implantation process and to predict the effect on device behavior of variations in the implantation process, several diagnostic techniques have been developed. In general, except for electrical measurements using the Hall technique,

1

radio-tracer sectioning, and static and transient C-V measurements, these techniques use either photons, ions, or electrons as a probe and luminescence, x-rays, electrons, gamma rays, or ions as the profile sensing mechanism. They include Rutherford scattering, ESCA (Electron Spectroscopy for Chemical Analysis), Auger spectroscopy, SIMS (Secondary Ion Mass Spectroscopy), and PRP (Proton Resonance Profiling) just to name a few. Reference (11) explains how some of these techniques can be used. All of these techniques suffer from one or more of the following limitations:

1. They destroy the sample either by bombardment with high energy particles or successive layer removal in order to obtain depth information about the impurity implant.

2. The technique requires a p-n junction be formed and several samples be tested for one profile.

3. Suitable reactions are necessary for the implanted species.

4. The profiling process requires one or more days to complete.

5. The equipment for the analysis is very expensive.

A technique that can be used for profiling which eliminates the above problems would be extremely useful. Such a technique could allow routine testing of device structures in an early fabrication phase, thus avoiding further processing on defective ones. This would save considerable time and money in fabricating circuits from GaAs. One such process is depth-resolved cathodoluminescence. This process uses a beam of electrons to excite carriers in the target that then recombine radiatively. By using low current densities and low beam energies (20 keV or less) the sample is not altered. The test equipment necessary for the

technique is not very expensive compared to some of the other profiling techniques listed above. Depth-resolved cathodoluminescence does not require a p-n junction be formed or more than one sample tested in order to obtain the implant profile versus depth into the sample. While there is a requirement for the implant species to be optically active in order to be used for cathodoluminescence, this is not a practical limitation since the common implant species in GaAs are optically active after annealing. (Only if the profile is desired before optical activation of the sample (annealing) takes place is cathodoluminescence limited.) Lastly, the profiles can be done extremely fast with the proper test set-up. By automatically sweeping the electron beam voltage and processing the resulting data on an online computer, the profile can be obtained in minutes.

Cathodoluminescence on GaAs has been performed by many authors, some of which are listed in references (1-6, 11-16). Especially Dumoulin[5] observed changes that indicated that cathodoluminescence could be used as a technique to obtain depth profiles of the dopant in ion implanted GaAs. His results were qualitative, however quantitative results have also been attempted[7, 9, 18, 19, 21]. None of these quantitative efforts have been concerned with the cathodoluminescence from ion implanted semiconductors. This current study tries to establish a quantitative basis for cathodoluminescence from such implanted semiconductors. This is the first step in developing cathodoluminescence as a tool for deducing the shape of the ion implanted depth profile in semiconductor materials.

Summary of the Research

The objective of this research is to develop and verify a model describing cathodoluminescence in ion implanted GaAs. This was accomplished in a two step process. First, a model for the luminescence from ion implanted GaAs was developed. This model differs from preceding ones in that the implanted ion distribution is specifically included in the analysis. The result of this portion of the research was used to predict the luminescent intensity as a function of the electron beam energy for a specific ion implanted profile. Second, the model was validated by a suitable experiment that confirms the theoretical predictions. This constitutes the forward problem, that is, predicting the luminescence assuming a known implant profile. The inverse problem of predicting the implant profile versus depth given the luminescence curve has not been attempted and constitutes an area for future work.

The luminescence measurements were made on Mg ions implanted in epitaxial GaAs. Epitaxial GaAs was used since it is the highest purity GaAs available and hence there are fewer transitions competing with the Mg line. Mg was chosen since it has not been previously studied in GaAs epilayers and since theoretical studies[20] of Mg ion penetration into GaAs indicate it should penetrate to a depth comparable to that of the electron beams being used.

The results of this research include the identification of many of the lines in the Mg implanted GaAs spectrum from 1.32 eV to 1.52 eV, a study of the effect of changing the current density of the electron beam on the spectra and a comparison of the theoretical and experimental luminescence curves. These results show that changing the current density

4

at the sample surface dramatically changes the spectra, and that good
agreement exists between the theoretical and experimental luminescence
curves.

The principal conclusion of this research is that the model presented
here of the cathodoluminescence experiment can be used to accurately pre-
dict the relative intensity of the ion implanted line in epitaxial GaAs.

Organization of Dissertation

The remaining chapters of this dissertation describe the model, the
experiment, and present results, conclusions, and recommendations. In
Chapter II the analytical model for cathodoluminescence is developed.
This model consists of three parts. The first part is a Monte Carlo
simulation of electrons penetrating into GaAs. This simulation provides
the information necessary to determine the generation function for elec-
tron-hole pairs. The electron-hole pairs diffuse through the GaAs before
recombining. Thus the development and solution of the appropriate dif-
fusion equation is covered in the second section of Chapter II. The
third section contains a discussion of the equation used to calculate the
luminescence versus beam voltage, $L(V)$, curves. This equation considers
the shape of the implanted ion profile, the excess carrier density pre-
dicted by the solution to the diffusion equation, and the absorption
coefficient of the emitted radiation. In addition, all $L(V)$ curves
derived from the ion implant are normalized to the $L(V)$ curve for a
uniform implant. This normalization removes variations in the experi-
mental data that might be expected to occur from run to run. This makes
the comparison of experimental and analytical results easier. Next, a

5

study of how the L(V) curves vary as the diffusion length, surface recombination velocity, absorption coefficient and impurity profile are changed. The chapter concludes with a summary of how the calculation is performed.

In Chapter III the experimental system and the procedures used to verify the model are described. The experimental system necessary to verify the model requires certain features in order to get any kind of consistent results. These features include: an electron beam which can be easily and repeatedly controlled, a beam current density which must be uniform across the sample, and an optical system which should be insensitive to small variations in position. In the first section a description is given of an existing cathodoluminescence system and how it was modified to meet these particular requirements. The following section contains a review of the previous work with Mg doped and implanted GaAs. All previous work has been with substrate quality GaAs. This is the first report of extensive measurements on Mg implanted epitaxial GaAs. The final section of Chapter III contains a list of the samples available for testing, how they were made and how they were processed before testing.

The results obtained using the system described in Chapter III and the comparison of analytical and experimental L(V) curves comprise Chapter IV. First, the spectrum from Mg ion implanted GaAs is analyzed. Various lines between 1.3 and 1.5 eV are identified. It is shown how depth resolved cathodoluminescence can be used to identify lines by determining where the concentration of the impurity is maximum. Next, a study is conducted of the spectral variation with current density. A possible explanation for this variation is given. The reason that this variation

6

is important to depth resolved cathodoluminescence is discussed and the proper action taken to minimize its impact is given. The L(V) curves are presented in the third section. In the final section the analytical and experimental L(V) curves are compared. The physical parameters chosen for the analytical curves are justified based on other workers' results.

Conclusions based on this work and recommendations for future work are presented in the last chapter. The main conclusion is that a basis for quantitative cathodoluminescence has been established. The recommendations generally concern improvements in the experimental facilities and the theoretical model.

II. The Model

In order to analytically determine the luminescent intensity as a function of the electron beam energy, the following processes need to be considered. The electron beam loses energy to the GaAs by creating electron-hole pairs; thus the method of calculating the rate of energy loss with depth is important here as this determines the generation function for electron-hole pairs. The electron-hole pairs just created then diffuse through the crystal before recombining. As far as the luminescence curve is concerned, the position where the electrons and holes recombine is important, not the position where they were generated. The actual luminescence that emerges from the surface can then be calculated. This requires that both absorption of the recombination radiation and the density of recombination centers be considered.

The luminescence versus beam voltage, L(V), curve can be calculated by either a completely analytical approach, or by a numerical approach. The analytical approach has been followed by Gergely[18], Wittry and Kyser[7, 8, 9], Rao Sahib and Wittry[19], and Fano[21]. Gergely assumed a depth-dose curve and solved the diffusion equation for the excess carrier density. Given that the recombination centers were uniform in depth, he was able to integrate the excess carrier expression to find the L(V) curve.

Wittry/Kyser and Rao Sahib/Wittry determined L(V) curves by solving the diffusion equation using the Green's function determined by van Roosbroeck[22]. In reference (19) the luminescence intensity is assumed proportional to the excess carrier density raised to some power between 1 and 2, while in reference (9) the power is assumed to be 1.

8

Fano[21] takes a different approach. He solves for the integral of the product of the energy lost by electrons within the crystal and the average depth of the energy loss. He assumes a model in which surface effects are more important than bulk effects and comes up with a Boltzmann-like equation that he can solve analytically.

The numerical solutions are based on either a numerical solution of the Boltzmann equation[23, 24] or a Monte Carlo approach[25, 26, 27]. None of the authors who used numerical techniques calculated L(V) curves. As they were all motivated by electron microprobe work, they usually calculated the spatial distribution of x-ray production in solid targets. Their principal result of interest is the calculation of the rate at which electrons lose energy as they penetrate a solid target (called energy loss or depth-dose curves).

The Boltzmann equation approach takes the transport equation,[24, 39]

$$\frac{\partial}{\partial s}[\sin\theta f(x,\theta,s)] = - \cos\theta\frac{\partial}{\partial x}[\sin\theta f(x,\theta,s)] + \frac{1}{\lambda(s)} \frac{\partial}{\partial\theta}\sin\theta\frac{\partial}{\partial\theta}[f(x,\theta,s)]$$

and solves for $f(x,\theta,s)$, the electron distribution function. In this equation, x is the depth into the crystal, s is the path length of the electron, θ, the angle the electron makes with the normal to the surface, and λ is the transport mean free path. A complete solution for $f(x,\theta,s)$ gives the complete history of electron transport in the specimen. Since energy depends only on the path length traveled and not on the depth, the path length, s, gives the energy of the beam at depth x headed in the θ direction. From here the depth-dose curve can be calculated, then the diffusion equation solved for the excess carrier density and the L(V) curve calculated.

9

The Monte Carlo approach uses a Monte Carlo technique to determine the depth-dose function. Using the depth-dose curve as a forcing function, the diffusion equation is solved for the excess carrier density. The L(V) curve can be found by integrating the product of the excess carrier density and the recombination center density over depth. It is possible to solve the problem through to the L(V) curve using Monte Carlo techniques.

An analytical approach was rejected for this study since the parameters on electron beam penetration into GaAs are not readily available. This means that either a Monte Carlo simulation or a transport equation solution would be required to provide the necessary information to evaluate the theory. The Monte Carlo equation approach was selected because there exists a bigger body of literature and the results are better documented than for the Boltzmann equation approach. The Monte Carlo analysis also has the advantage of being more conceptually transparent than the transport equation approach. In addition, this approach makes data interpretation and program modification easier. Of the two Monte Carlo approaches, i.e. total or partial simulation, the total Monte Carlo simulation was ruled out because the scattering cross sections necessary are not readily available and because the partial simulation requires much less computer time to execute.

This chapter is divided into three parts. In the first part, the Monte Carlo analysis of electrons penetrating into GaAs is developed. This includes a section describing the past work on electron penetration into solids, a section describing how the Monte Carlo calculation was performed, and a section of results where the Monte Carlo analysis is

10

compared to other workers' results. In the next part of the chapter,
the diffusion equation is solved for the excess carrier density and the
L(V) curve is calculated. The appropriate diffusion equation is first
derived and then the computer programs that are used to evaluate the
excess carrier density and the L(V) curves are described. Finally, the
results of the L(V) calculation are presented in the form of graphs that
show how the L(V) curve varies as the diffusion length, surface recom-
bination velocity, absorption coefficient, and impurity profile are
changed. In the last part of this chapter the calculation procedure is
summarized for future easy reference.

Electron Penetration into GaAs: Background

The theoretical analysis of electron beam/target interaction falls
into three categories. These are: single, plural, and multiple scat-
tering of the electron beam, depending on whether there are one, a few
(less than 25), or many electron-atom interactions. This usage differs
from that of high energy scattering where single, plural, and multiple
scattering are synonymous with large, medium, and small angle scattering
respectively.

Single scattering results from elastic collisions between electrons
and atomic nuclei. The theoretical treatment starts with the classical
Rutherford formula. Various theories exist to take account of the screen-
ing effect of the electron cloud for the nucleus. The most frequently
applied corrections to Rutherford scattering are the Wentzel and the
Thomas-Fermi statistical model. The Wentzel model assumes an exponential
fall of the screening field. The Thomas-Fermi approach determines the
field for the atoms by considering the atomic electrons as a degenerate

11

gas. The potential so obtained is used within the first Born approxima-

tion to calculate the differential scattering cross section. Everhart[30]

used the single scattering assumption to develop a simplified theory for

the reflection of electrons from solids. The theory of plural scattering

has been discussed by Bothe[31, 32], Wentzel[33], Moliere[34], Lenz[35],

and Smith and Burge[36] among others. Cosslett and Thomas[37] have

reviewed these treatments in an attempt to explain their experimental

results. The experimental work reported by them in reference 37 showed

good agreement with Bothe's theory in the form due to Lenz. Bothe had

been able to give a formal solution for plural scattering on the basis

of a statistical approach called error theory. In Bothe's analysis he

assumed successive collisions to be statistically independent and ne-

glected large angle single scattering and energy loss. The problem with

Bothe's theory is that the two main equations are very difficult to

integrate. Lenz was able to integrate the first of Bothe's equations

and cast the second one in a form for numerical integration.

The multiple scattering theories were first developed by Bothe[32, 38], Bethe, Rose and Smith[39] and on slightly different lines by Goudsmit

and Saunderson[40], Lewis[41], Spencer[42, 43] and Meister[44]. Cosslett

and Thomas[45] have also discussed the multiple scattering theories,

where they compared the various approaches against measurements on

aluminum, copper, silver and gold. Bothe's approach is based on error

theory as is his plural scattering theory. The others are based on the

diffusion equation. Bethe, Rose, and Smith neglect energy loss and use

the Fokker-Planck approximation to the diffusion equation which neglects

large angle single scattering. Goudsmit/Saunderson, Lewis, Spencer, and

12

Meister included the energy loss, but only considered infinite targets where the source was assumed embedded in the target. These theories were moderately successful for high beam energies where the common assumption of small angle scattering holds. The attempts to modify the theory for energies in the 1 to 50 keV range were by Moliere[46] and Lenz[47]. All of these theories assume that the beam is normally incident to the target surface.

With the advent of larger computers, numerical solutions to the penetration problem have been more prevalent lately. Brown and Ogilvie[48] solve the Boltzmann transport equation numerically using the multiple scattering approach of Bethe, Rose and Smith. Later Brown, Wittry and Kyser[49] refined the calculations by considering different approximations over different path legnths. For instance, they use a single scattering approximation to the Boltzmann transport equation for short path lengths. The result of their calculation is a distribution function $f(x,\theta,S)$ that gives the probability that an electron which has traveled a distance between S and S + dS will have a position between x and x + dx below the specimen surface while at the same time its direction of travel makes an angle with the internal normal to the specimen surface of between θ and θ + dθ. The distribution function is then used to calculate physically observed results. An alternate approach is a Monte Carlo simulation. There are two kinds of simulations that may be employed. Direct simulation considers each collision an electron would have as it penetrates the target. The alternative is a "condensed" random walk where many electron-target collisions are condensed into one equivalent collision. Calculations of the latter have been performed

by Green[51], Bishop[52] and Shimizu et al[54]. Direct simulations have been made by Shimizu et al[54] and by Green and Leckey[55]. A detailed explanation of the interaction of 1 to 50 keV electrons with solids has yet to be achieved despite all of the theoretical activity cited above. One of the limitations in the application of the theoretical models to scattering experiments from solids lies in their reliance on adjustable parameters and in the fact that they provide little insight into the dynamics of the individual collision process involved. A purely analytical approach to the problem of electron scattering based on a consideration of individual scattering events would present formidable problems. Realistic boundary conditions are also very difficult (if not impossible) to handle theoretically. On the other hand, these problems are easily handled with a Monte Carlo analysis. The best agreement between experiment and theory for electrons penetrating into solids comes from a Monte Carlo analysis (see references 53 and 54). In addition, a Monte Carlo analysis has the intuitive appeal of being just as the theoretician pictures the experiment occurring. Thus, the results tend to be more transparent than in more obscure theoretical approaches.

Although a great deal of effort has been put into studying electron-beam penetration into solids comparitively little work has been done with crystalline solids. References that apply to GaAs are Stimler[56], Anderson[57], Klein[58], Schiller and Boulou[59], Norris et al[13], and Wittry and Kyser[60]. Stimler gives families of curves of the depth of electron penetration versus density of the solid with electron energy as a parameter. These curves are deduced from the data of Ehrenberg and King[61]. He only considers electron beams normal to

14

the surface and does not plot "depth-dose" curves (energy dissipation versus depth into the target). Anderson applies Spencer's[43] theoretical work for electrons released in an infinite medium to GaAs. While the boundary conditions are different (the target-vacuum interface in Anderson's case is at depth equals zero while Spencer's theory is for an infinite medium), Anderson calculates depth dose curves for 25, 50 and 100 keV beams anyway. He does not consider the effect of different angles of incidence on the target nor does he indicate what to do for voltages below 25 keV (Spencer's lowest energy).

Klein has attempted to develop a phenomenological model capable of describing all pertinent aspects of electron-beam penetration that will agree with experimental evidence wherever comparisons can be made. Klein assumes the electrons penetrate into the crystal without loss to a depth, R_B, the depth of complete diffusion, where they diffuse randomly in all directions, transferring energy to the medium at an exponentially decreasing rate along any radius vector of the sphere of excitation (see fig. 1). Klein's phenomenological curves reproduce Anderson's calculational results for GaAs. Schiller and Boulou use Klein's model to calculate depth-dose curves at beam energies lower than 25 keV. Again Klein's data ignores the effect of the angle of electron beam incidence on the target. Also ignored is the crystalline structure of the target since the results are the same for amorphous as well as crystalline materials.

Norris[13] et al present depth dose curves for electrons penetrating into GaAs at 45° incidence with energies of 5, 10, and 20 keV. These curves were obtained by scaling an experimentally determined high

15
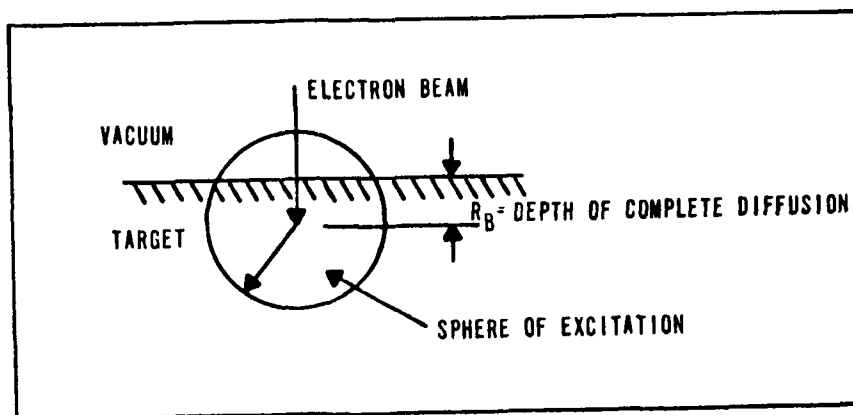
Fig. 1 Klein's Penetration Model

energy (2 MeV) curve to the low energy (a few keV) normal incidence
electron range. Their justification for this procedure is that the
depth-dose curve is approximately a universal curve that can be scaled
given a known electron range for a given incident electron energy. This
has only been established at keV energies and normal incidence but they
assume that the high energy curves can be scaled to the keV range for
various angles of incidence. Wittry and Kyser assume that the depth-
dose curve is Gaussian. They consider only normal incidence at 29 keV
and determine the mean and standard deviation from the transport cal-
culation made for them by Brown following the technique in reference
(48). They suggest that the parameters for other energies be obtained
by scaling the 29 keV data, by taking experimental data, or by calcula-
ting using the transport equation approach or a Monte Carlo technique.
The Monte Carlo technique is the approach chosen here.

Monte Carlo Analysis

    This section will begin with a summary of the Monte Carlo calcula-
tion, with certain parts of the calculation developed in detail. Then

16

a brief description of the computer programs used to perform the analysis will be given.

The electron energy loss curves (called depth-dose curves) for electron beams penetrating into GaAs were calculated using the standard Monte Carlo procedures as reviewed by Berger[50]. This procedure consists of condensing several elastic atomic collisions into one equivalent collision. The scattering angle is randomly chosen from a table of angles that is constructed from the multiple scattering theory of Goudsmit and Saunderson[40]. The length or amount of material the beam must go through to suffer the required number of elastic collisions is called the step size. The particular formulation used here takes into account the step size and the energy of the beam at the beginning of each step. Bethe's law as given in reference (62) is used to account for the energy loss in each step. The step size and location of the point of the scattering follow the method of Shimizu et al[53]. In this method, the step size is scaled according to the energy of the beam at the beginning of each step, the initial beam energy, and the initial step size. Given the angle through which the electron is going to scatter, the location of the scattering point, the energy of the electron at the beginning of the step, and the energy lost in the step, the trajectory and energy loss over that trajectory can be calculated. The energy loss curve is then calculated by dividing the thickness of the target into equal increments, called bins, and then calculating how much energy is lost in each bin. At this point, a more detailed discussion will be given on the angular distribution function, the step size, the method of random sampling and Bethe's energy loss law.

17

Goudsmit and Saunderson[40] studied the angular distribution of multiple-scattered particles. They derived the exact angular distribution function as a Legendre series,

$$A(\omega)\sin\omega d\omega = \sum_{k=0}^{\infty}(k + \tfrac{1}{2})\exp\{-\int_{0}^{s}G_k(s')ds'\}P_k(\cos\omega)\sin\omega d\omega \qquad (1)$$

where $G_k(s) = 2\pi N\int_{0}^{\pi}\sigma(\theta,s)\{1 - P_k(\cos\theta)\}\sin\theta d\theta$.

N is the number of atoms per unit volume, s is the path length traveled by the particle in that particular step, and $\sigma(\theta,s)$ is the single scattering cross section. Since the electrons do not lose much energy over any one step, the collision cross section is assumed constant over that particular step. Thus in equation (1),

$$\int_{0}^{s}G_k(s')ds' = \int_{0}^{\Delta s}G_k(s')ds' = C_k(s)\Delta s$$

The Goudsmit-Saunderson distribution applies to all angular deflections regardless of their magnitude. It can also be evaluated for any desired single scattering cross section. The cross section that is used here is the screened Rutherford cross section

$$\sigma(\theta,s) = (Z^2 e^4)/(p^2 v^2(1 - \cos\theta + 2\eta)^2) \qquad (2)$$

where Z is the equivalent atomic number (32 for GaAs), e is the electron charge, p is the electron momentum, v is the electron velocity, and η is a parameter that takes into account the screening of the nuclear charge by the orbital electrons. η is considered an adjustable parameter whose value can be approximately determined from a formula by Nigam et al[64],

$$\eta = \tfrac{1}{4}\{1.12(h/p)(Z^{1/3}/0.885a_o)\}^2 \qquad (3)$$

where a_o is the Bohr hydrogen radius and k is Planck's constant.

The path length, s, that the electron will travel is broken down into a number of steps, ΔS_i. The step size over which the angular distribution is to be calculated must be long enough to satisfy the treatment of multiple scattering and to obtain stable convergence of equation (1). On the other hand, ΔS_i should be as short as possible to improve the accuracy of the Monte Carlo calculation. Shinoda et al[63] have shown that by choosing the ith step size to be

$$\Delta S_i = \frac{E_i}{E_o} \Delta S_o \tag{4}$$

where E_i, the beam energy at the beginning of the ith step, is given by

$$E_i = E_{i-1} + \frac{dE}{ds}\bigg|_{E = E_{i-1}} \Delta S_i \tag{5}$$

the accuracy of the calculation is about the same in each step. The quantity ΔS_o is the first step length and must be given. This initial step size is hard to determine. Its value can be estimated from Coss-lett and Thomas[65] or taken as approximately the value for copper found by Shinoda et al[63]. As the initial step size is a parameter that is to be adjusted to improve agreement with experimental results, Shinoda's value for copper, .18 microns at 30 keV beam energy, will be used.

The procedure used to sample random variates from a distribution function with the use of pseudorandom numbers relies on the calculation of the cumulative probability distribution function (see any book on Monte Carlo, e.g. references 50 or 66)

$$F(x) = \int_{\infty}^{x} f(x')ds', \tag{6}$$

19

where f(x) is the distribution function to be sampled. In order to sample f(x):

(a) Compute F(x) for a dense set of x values over the range of f(x).

(b) By interpolation, find a set of x values such that

$$F(\tilde{X}_m) = (m - \tfrac{1}{2})/M \qquad m = 1,2\ldots M \qquad (6\text{-}A)$$

(c) Store the $F^{-1}(\tilde{X}_m)$ in computer memory.

(d) Choose a random number ρ.

(e) The desired f(x) is the one located at memory location i = integral part of ρM.

The Goudsmit and Saunderson distribution is used to determine the polar angle. The azimuthal angle is distributed from 0 to 2π provided the medium is isotropic and polarization is ignored.

The electrons are assumed to lose energy continuously. This is called the continuous slowing down approximation. In this approximation, the effects of straggling are ignored. Energy loss is usually given in terms of Bethe's law[67]. The particular form chosen for Bethe's law is given by Berger and Seltzer[62] following the formulation of Rohrlich and Carlson[68], it is

$$\frac{dE}{ds} = -\frac{2\pi N_a \rho r^2 mc^2}{\beta^2} \frac{Z}{A} \log \frac{\tau^2(\tau + 2)}{2(I/mc^2)^2} + F^-(\tau) - \delta \qquad (7)$$

$$F^-(\tau) = 1 - \beta^2 + [\tau^2/8 - (2\tau + 1)\log 2]/(\tau + 1)^2$$

where

mc^2 = rest energy of electron = 0.511 MeV

20

$$\tau = \text{kinetic energy in units of } mc^2$$

$$\beta = [\tau(\tau + 2)]^{\frac{1}{2}}/(\tau + 1) = \text{velocity}/c$$

$$Z = \text{atomic number}$$

$$A = \text{atomic weight}$$

$$\rho = \text{density}$$

$$I = \text{mean excitation energy}$$

$$\delta = \text{density effect correction}$$

$$N_a = \text{Avagardro's number}$$

$$r_o^2 = (e^2/mc^2)^2 = 7.904030 \times 10^{-26} \text{ cm}^2.$$

The density effect correction, δ, takes into account the reduction of the collision loss due to polarization of the medium. Based on the values given for copper, the density effect correction is negligible at these beam energies. The mean excitation energy, I, is chosen to conform to the recommendations of Berger and Seltzer[62]. They give an approximate formula for I which they call I_{adj} since it is slightly larger than the I defined in terms of oscillator strengths. It is the I_{adj} value that is used for this Monte Carlo calculation.

$$I_{adj} = Z (9.76 + 58.8 \ Z^{-1.19}) \tag{8}$$

For mixtures and compounds, the mean energy loss is assumed to be the sum of the losses in the constituent elements. Thus

$$\log I_{adj} = \frac{Z}{A}^{-1} \frac{1}{\rho} \sum_j \frac{Z_j}{A_j} \rho_i \log I_{adj,j} \tag{9}$$

and

$$Z/A = \frac{1}{\rho} \sum_j Z_j \rho_j / A_j$$

For GaAs, $Z = 32$, $\rho = 5.32$ gr. and $I_{adj} = 342.4$ ev.

Given the above values, the cumulative distribution function for multiple scattering of electrons in GaAs is calculated. The program that does this is called LMSD. It is used to evaluate a cumulative distribution function for each E_i as determined from equation (5) down to an E_i approximately equal to 1 keV. At this point, the velocity of the incoming electron becomes about the same as the velocity of the atomic electrons. The electron stopping formula [equation (7)] is no longer valid. Since the exact form is not known, an arbitrary interpolation procedure is used. Berger and Seltzer follow Nelms[69] and assume $(dE/ds) = 0$ at $E_i = 0$ and linearly interpolate from $E_i = 0$ to $E_i = 1$ keV. Here the same procedure is used. Next, a table of angles is constructed according to formula (6-A). These are stored on data cards for use in the next phase of the calculation.

The program used to calculate the energy loss versus depth curves is called EPIGA for electron penetration into GaAs. The main parts of the program are shown in figure (2). The program uses the cumulative distribution functions from LMSD and the GaAs parameters as inputs and calculates the energy loss versus depth curve called the DEDS curve. Its output is a table of the energy an average electron is expected to lose at that depth versus depth. Included in the output is the average energy loss versus depth for the backscattered as well as absorbed beams. The number of electrons backscattered and absorbed, the total number of electrons, the angle of incidence for the beam, the incident energy and total beam energy are then compared to make sure all of the energy is accounted for.

22

The intermediate steps in the calculation include calculating the
energy loss versus path length, the electron trajectory and the amount
of energy lost in each bin. The energy loss versus path length is the
same for all electrons. This is just another way of saying that strag-
gling has been ignored. This does not mean that all electrons have the
same energy loss at a particular depth. What it does mean is that all
electrons that have traveled through the same amount of GaAs have lost
the same amount of energy regardless of their respective depths. Next,
a matrix is formed that lines up the depth in the material with the
depth at which the particle scattered and the energy loss over that
step. The axis normal to the target surface is divided up into equal
increments called bins. Subroutine Score is then used to take this
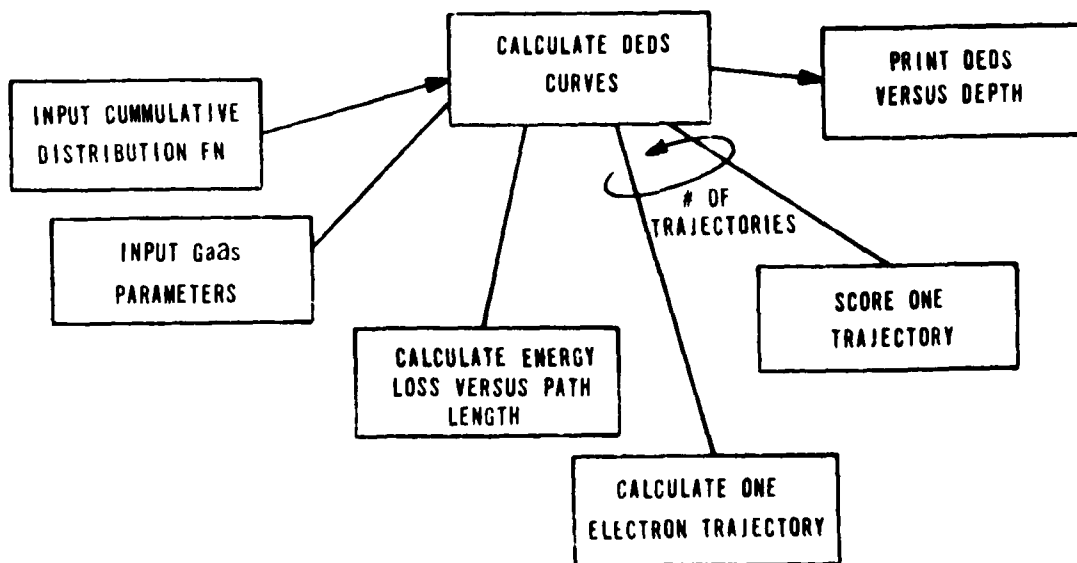
Fig. 2   Calculation of the Energy Loss Curve

matrix and decide how much energy is lost in each bin. A number of electron trajectories are computed and the average energy loss versus depth curve is calculated.

Results from the Program

In order to verify the EPIGA computer program, the results for electrons at 30 keV normally incident on Cu were checked against those of Shimizu[53]. The results of this check[70] verified that EPIGA is functioning properly.

As mentioned earlier n and ΔS_o are considered adjustable parameters that help match the results from the model to experimental results. Unfortunately, there is not a great deal of information on electron beam interaction with GaAs as contrasted to the work on Al, Cu, Ag, and Au. One data point that is available is the one reported by Wittry and Kyser[60]. They used a backscattered fraction of 0.33 for a 30 keV beam of electrons normally incident on GaAs. A number of runs with different combinations of n and ΔS_o showed that ΔS_o = .185 micron and n = .0054972 reproduce Wittry and Kyser's result. The Monte Carlo simulation predicted a backscattered fraction of 33.78%. An additional checkpoint is given by Klein[58]. He calculates the fraction of beam energy that should be backscattered for various elements and compounds. For a 30 keV beam of electrons normally incident on GaAs, he gets an energy loss fraction of 23.7%. The Monte Carlo result is 22.9% which agrees very well.

Figure (3) shows depth dose curves for a beam incident at 45° with energies of 5, 10, 15, 20 keV. Figure (4) is a least squares approximation by cubic splines with variable knots. The curve fit is performed

24
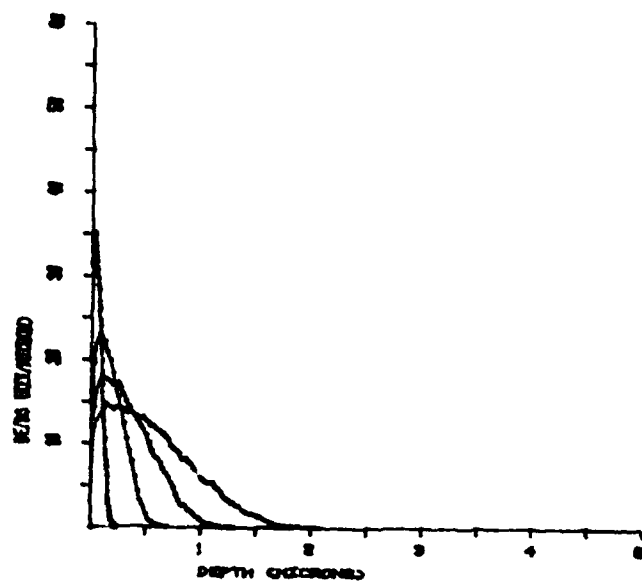
Fig. 3   Depth-Dose Curves at 45° for 5, 10, 15, 20 keV
         Beams— Raw Data
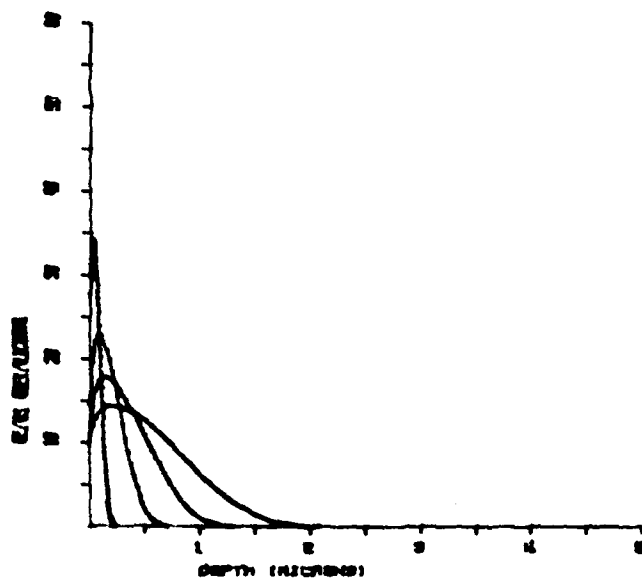
Fig. 4   Depth-Dose Curves at 45° for 5, 10, 15, 20 keV
         Beams--Smoothed Data

25

by subroutine ICSVKV, an IMSL subroutine. The curve is truncated whenever the tail of the least squares fit goes negative or turns up. The curve is also terminated when the raw data runs out. These curves can be compared to energy loss curves for Norris et al[13] shown in figure (5).
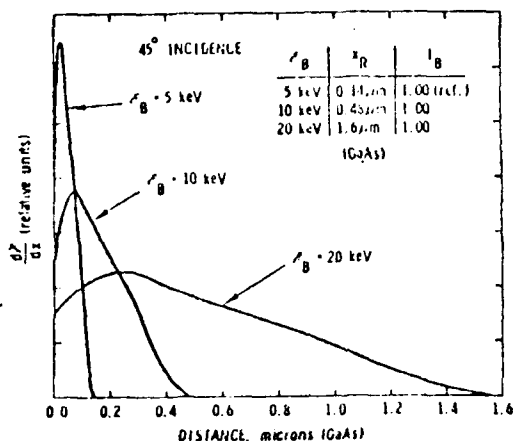
Fig. 5 Depth-Dose Curves - Norris et al[13]

The Monte Carlo analysis predicts a deeper penetration than the curves Norris derives. Martinelli and Wang[71] measured the depth that electron beams of normal incidence penetrate into GaAs. In their experiment, GaAs thin films were grown on $MgAl_2O_4$ spinel substrates. When the electrons had sufficient energy they caused the $MgAl_2O_4$ to glow when they struck it. By noting at what voltage the electron beam just penetrated through the GaAs into the $MgAl_2O_4$, and by knowing the thickness of the thin film, as well as correcting for the residual energy left in the beam in order to make the $MgAl_2O_4$ glow, they were able to establish

26

a depth of maximum penetration. Table I compares their results with those of this study. In all cases their range is greater than the one predicted here. There are several reasons for this. One reason is that the electrons had to have some energy left when they struck the $MgAl_2O_4$ substrate in order to be detected. While Martinelli and Wang corrected their data for this, the lower energy scattering is more isotropic than the higher energy scattering, the correction Martinelli and Wang apply overcorrects their range values, making them longer than they should be. Another reason is that the Monte Carlo data at the deepest penetration depths is subject to large statistical errors; there are not many electrons that make it to this depth. Finally, the lower energy loss rate was arbitrarily set. While this does not change the overall shape of the depth-dose curve much, it could affect the tail of the curve. In spite of these problems, the agreement is considered excellent.

Table I. Comparison of Martinelli and Wang's Experimental
Penetration Data to the Monte Carlo Analysis

Energy (keV)	M & W Maximum Depth (microns)	Monte Carlo Maximum Depth (microns)	% Difference
5	.283	.250	11.6%
10	.779	.725	6.9%
15	1.408	1.325	5.9%
20	2.142	2.125	.8%

The minor disagreement with Martinelli and Wang's data does not affect the rest of the calculation very much since at this depth the energy loss curve has dropped to a point where very few electron/hole pairs are being generated compared to shallower depths. Figure (6) shows the depth-dose curves for 5, 10, 20 and 30 keV beams at normal incidence.

27

Finally, figures (7), (8) and (9) are of the energy loss curves at
45° incidence for the remaining beam voltages used in the diffusion
calculation.

Calculation of the Excess Carrier Density and Recombination Radiation

The electron beam gives up its energy to the GaAs crystal by creating
electron/hole pairs and phonons. The electron/hole pairs then diffuse
away from the creation point, recombining at some other place in the
crystal. Some of the recombination radiation is given up as luminescence.
The goal of this study is to be able to calculate how the luminescent
intensity will vary with beam energy. If the excess carrier density,
density of available recombination states, and some exponential absorption
factor for the emitted radiation are known, the L(V) curve can be calcu-
lated. How that is done will be discussed in this section. The first
part is a derivation of the appropriate diffusion and L(V) equation.
Next comes an outline of the computer programs that were written to
solve these equations. This is followed by a results section that shows
how the L(V) curves change with various parameter changes. Last of all
is a summary of the L(V) calculation, reviewing briefly how all the
parts fit together.

Justification of Approach

The approach taken is to solve the one-dimensional diffusion equation
for the excess carrier density and then solve for the L(V) curve. In
this section, the approximations that are made in doing this, how likely
they are to be met, and in some cases, what alternatives are available,
will be discussed.

28
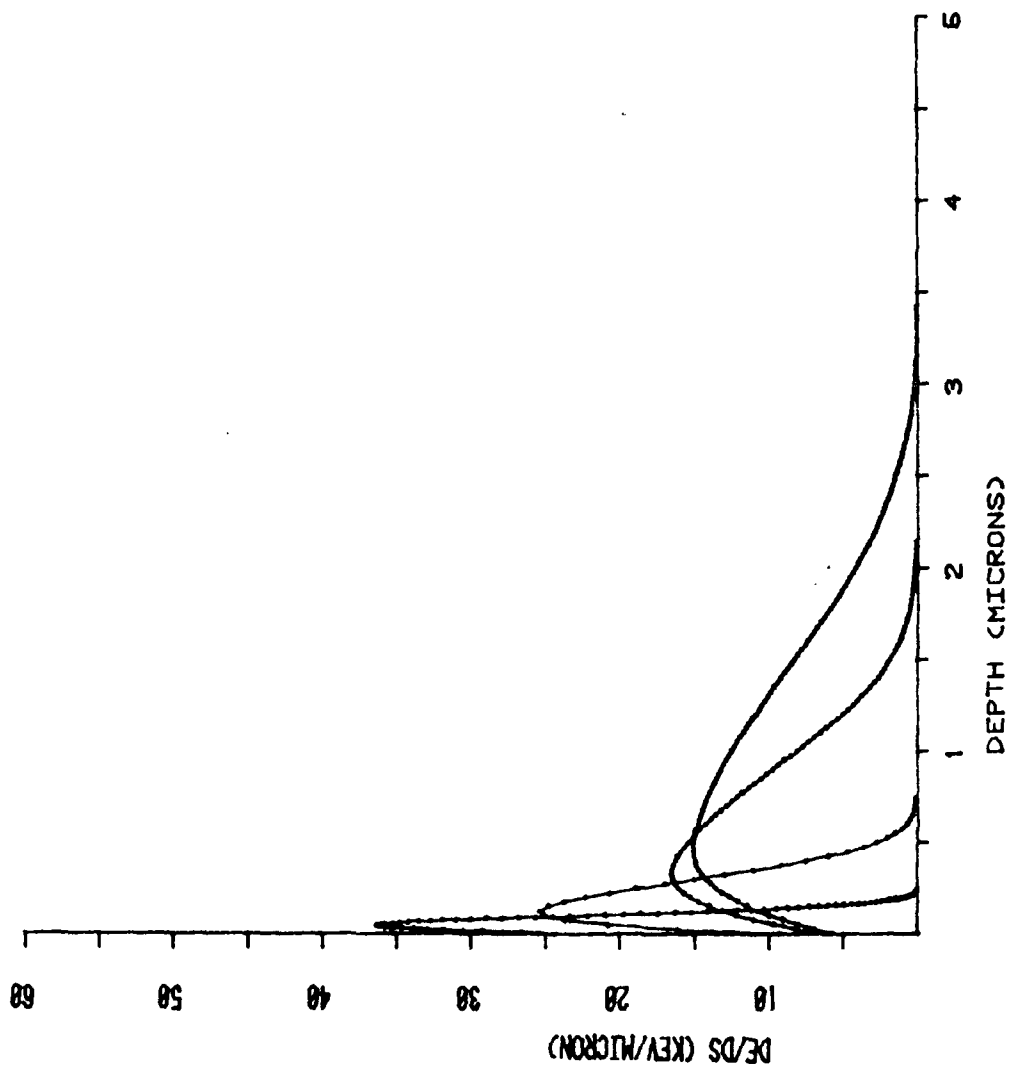
Fig. 6 Depth-Dose Curves at Normal Incidence for 5, 10, 20 and 30 keV Beams

29
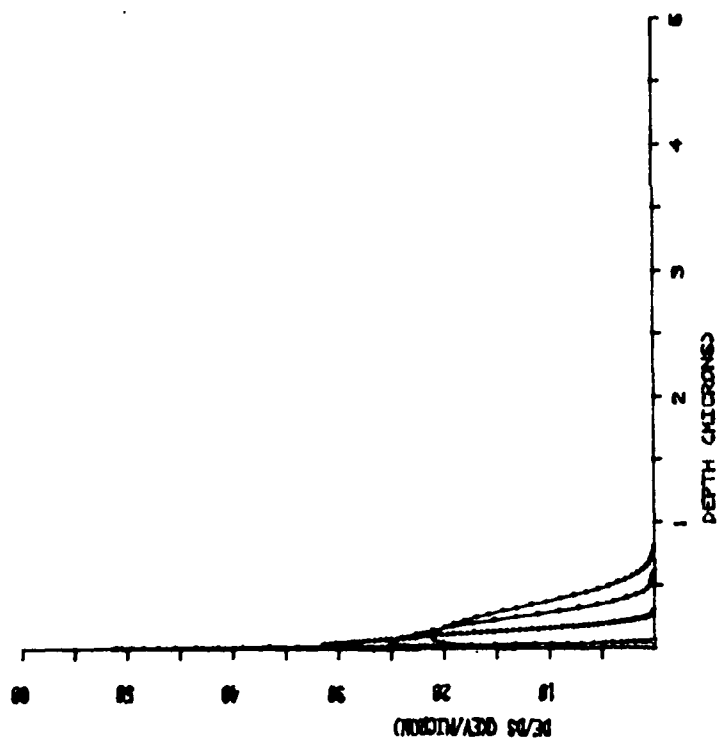
Fig. 7 Depth-Dose Curves at 45° for 2, 6, 9, 11 keV Beams
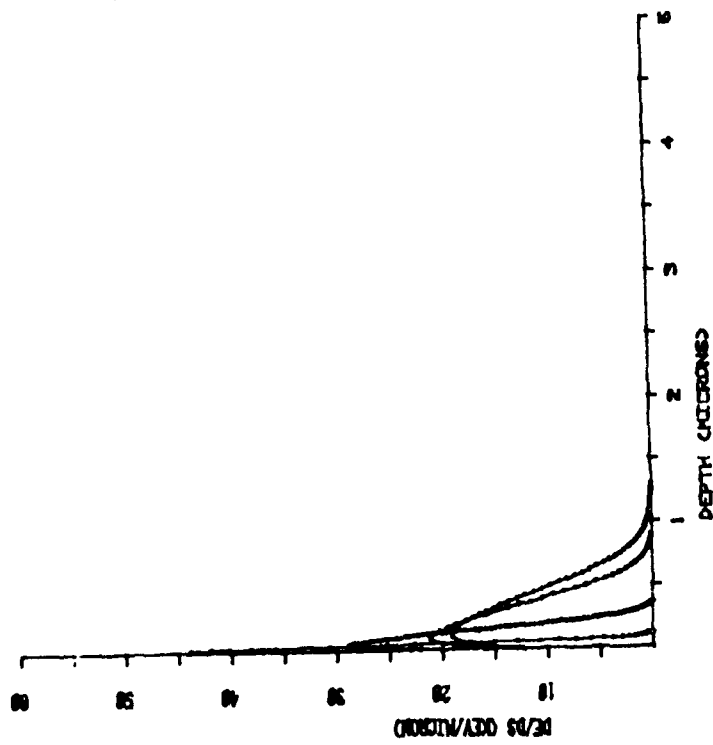
Fig. 8 Depth-Dose Curves at 45° for 3, 7, 12, 14 keV Beams

31

DEPTH (MICRONS)

DE/DX (KEV/U/CRON)
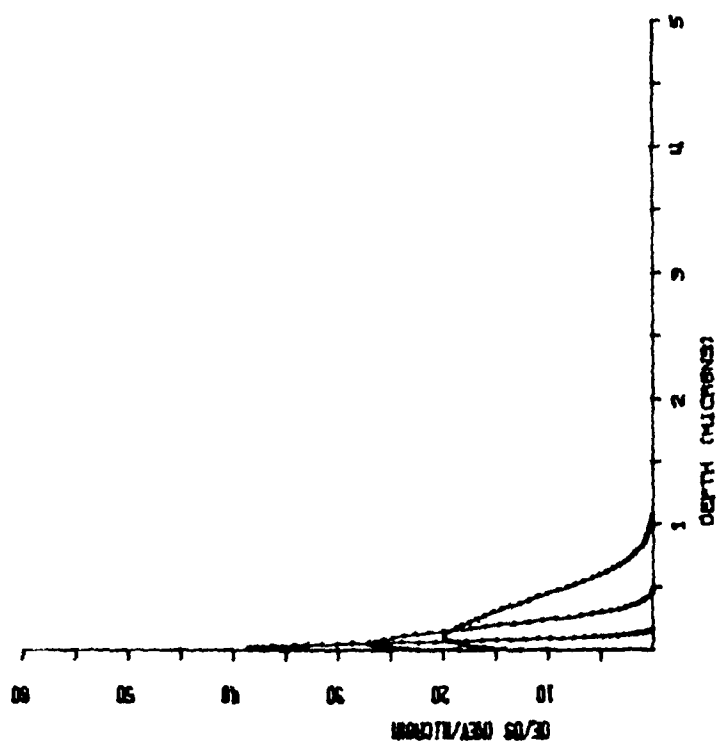
Fig. 9 Depth-Dose Curves at 45° for 4, 8, 13 keV Beams

32

Any elementary book on solid state theory or semiconductor physics will contain a discussion of the diffusion equation (see McKelvey[72] for instance). The diffusion equation can be written as[72]

$$-\nabla \cdot \vec{J}_p + g_p - p/\tau_p = \delta p/\delta t \qquad (10)$$

$$-\nabla \cdot \vec{J}_n + g_n - n/\tau_n = \delta n/\delta t \qquad (11)$$

with

$$\vec{J}_p = -D_p \nabla p + p\mu_p \vec{E} \qquad (12)$$

$$\vec{J}_n = -D_n \nabla n - n\mu_n \vec{E} \qquad (13)$$

the subscripts p and n refer to holes and electrons respectively. The $\vec{J}$'s are particle flux densities, the g's are generation rates, and the τ's are recombination rates. Equations (10) and (11) are frequently called the continuity equations. When (12) and (13) are substituted into (10) and (11), the results are

$$D_p \nabla^2 p + \nabla p \cdot \nabla D_p - \nabla \cdot (\mu_p p\vec{E}) + g_p - p/\tau_p = \delta p/\delta t \qquad (14)$$

$$D_n \nabla^2 n + \nabla n \cdot \nabla D_n + \nabla \cdot (\mu_n n\vec{E}) + g_n - n/\tau_n = \delta n/\delta t \qquad (15)$$

In equations (14) and (15) there is a term which depends on the depth dependence of the diffusion constant. In general, a variation in the diffusion constant of two orders of magnitude would be considered large, while n and p can vary over ten orders of magnitude in the same distance. Thus the term involving ∇D will be much less than the ∇^2 term. Consequently, the $\nabla n \cdot \nabla D_n$ and $\nabla p \cdot \nabla D_p$ can usually be ignored in the calculation.

33

Similarly, the spatial variation of τ_n and τ_p will be ignored. The lifetimes of holes and electrons is in general given by,[72]

$$\frac{1}{\tau} = \frac{1}{\tau_1} + \frac{1}{\tau_2} + \frac{1}{\tau_n} + \ldots \tag{16}$$

where τ_1, τ_2, τ_3 ... are the various individual radiative and non-radiative lifetimes. If τ is largely determined by the lifetimes associated with the implant, then it will be a function of depth. The quantum efficiency and radiative lifetime in p-type GaAs have been studied by Vilms and Spicer[73]. At 77°K they found bulk quantum efficiencies from 5 to 28%. This means that 5 to 28% of the recombination radiation went into radiative emission in the band which occurs from 0.1 ev below the band edge to the band edge. While they did not make measurements below 77°K, Biard, in a private communication to Vilms and Spicer, estimated the efficiency at 30%, substantially independent of temperature. It is not clear whether Biard intended that to mean down to 4.2 or not. For lower implant doses and higher anneal temperatures, the variation of the implant profile density over the background impurity density is expected to be less than two orders of magnitude. This observation is based on implant doses of less than 5×10^{13} cm^{-2}, anneal temperatures of 850° or greater, background impurity concentration of 1×10^{15} cm^{-2}, and the implant profiles for Mg[74]. The estimated change in the lifetime associated with radiative recombination through the implant species over about the first .7 of a micron is one and one-half orders of magnitude. Using Biard's 30% figure means that 70% of the recombination paths are non-radiative. These are assumed to be independent of the depth dependence of the implant species. Only about one-half of the remaining 30% of

34

the recombination paths is observed to come from the recombination path involving the implanted species. Thus the lifetime is a relatively weak function of depth and is assumed to be a constant independent of depth. Having a constant lifetime greatly reduces the length of computer time required to solve the diffusion equation.

The diffusion equation will also be restricted to one dimension. This assumes a wide parallel beam of electrons to be incident on the surface of the crystal. "Wide" is taken to mean several times the diffusion length of the electron/hole pairs. The dimensions of the crystal are much larger than the range of the incident electrons and the ambipolar diffusion length of the generated carriers. This makes the crystal appear semi-infinite. Charge balance or electrical neutrality is also assumed. This follows the discussion in McKelvey. Since the experiment is to be run at very low temperatures $(4.2\,°K-20\,°K)$ the thermal equilibrium values of electron density and hole density are almost zero compared to the excess carrier density. Thus the excess hole and electron densities are equal. The experiment is also conducted in steady-state so that all of the time derivatives are zero. The steady-state assumption also makes $g_p = g_n$ and $\tau_p = \tau_n$. Equations (14) and (15) come down to:

$$D_p \frac{d^2 \delta n}{dx^2} - \mu_p E_{int} \frac{d\delta n}{dx} - \mu_p \delta n \frac{dE_{int}}{dx} + g_n - \frac{\delta n}{\tau n} = 0 \qquad (16A)$$

$$D_n \frac{d^2 \delta n}{dx^2} + \mu_n E_{int} \frac{d\delta n}{dx} + \mu_n \delta n \frac{dE_{int}}{dx} + g_n - \frac{\delta n}{\tau n} = 0 \qquad (16B)$$

In these equations, δn is the excess electron density over the thermal equilibrium value and E_{int} is the internal electric field. Multiplying

35

(16A) by μ_n and (16B) by μ_p and adding eliminates both of the E_{int} terms. Dividing by $\delta n \, (\mu_n + \mu_p)$ yields,

$$\frac{D_p \mu_n + D_n \mu_p}{\mu_n + \mu_p} \frac{d^2 \delta n}{dx^2} - \frac{\delta n}{\tau n} + g_n = 0. \tag{17}$$

Defining $D* = \dfrac{D_p \mu_n + D_n \mu_p}{\mu_n + \mu_p}$ as the ambipolar diffusion constant results

in ambipolar transport equation,

$$D* \frac{d^2 \delta n}{dx^2} - \frac{\delta n}{\tau n} + g_n = 0 \tag{18}$$

This equation is the same even if $D*$ and τ_n are functions of depth.

L(V) Curve

Once the excess carrier density is found by solving equation (18), the luminescent emission can be found by integrating the rate of radiative recombination over the depth of the crystal. The rate of radiative recombination is proportional to the number of states through which the excess carriers can recombine and to the number of excess carriers. The number of states available for recombination for the free to bound Mg transition is the number of Mg ions with holes bound to them. As the excess carriers recombine, photons are emitted. These are reabsorbed as the radiation approaches the surface. Assuming an exponential absorption of the recombination radiation, the luminescence from the sample at one particular electron beam voltage can be found by summing the number of photons that reach the surface from those emitted at various depths in the crystal. This integral takes the form,

$$L(V) = \int_0^D BN(x) \, \delta n(x) \, \exp[-\alpha x] \, dx \tag{19}$$

where B is a constant that depends on the geometry of the experiment and the transition matrix element for recombination, $N(x)$ is the density of available states for recombination, and α is the absorption coefficient for the resulting radiation. In the evaluation of $L(V)$, D is arbitrarily set at 5 microns. At this point the excess carrier density is down several orders of magnitude from its peak value. Although $N(x)$ is the density of implant ions available for excess carriers through which to recombine, it is assumed that this density is proportional to the implant profile, any multiplying constant being absorbed into B.

Calculating the implant profile from the $L(V)$ curve is the basic motivation for this line of research. For this effort, though, the implant profiles are going to be assumed and the calculated $L(V)$ curves compared to the measured ones. Thus an implant profile must be measured by some other technique or calculated. The most common method of calculation is to use LSS theory[17] to determine an implanted impurity profile.

As the implanted ions penetrate into the target, they lose energy by two principal mechanisms. The first energy loss mechanism is due to elastic collisions of the ion with the nuclei of the substrate. These collisions account for the angular scattering of the ions with very little energy loss. The second energy loss mechanism is an inelastic interaction between the ion and the electrons of the substrate atoms. This mechanism accounts for the energy loss of the ions with very little angular deflection. These energy loss mechanisms are described by differential cross sections. The differential scattering cross sections are determined by the potential between the ion and the substrate and by the nature of the interaction. LSS theory uses the Thomas-Fermi potential

based upon a classical statistical model for the atom. The LSS results
are given in terms of the mean and various moments of a Gaussian distri-
bution function. The projected range, standard deviation, and moment
ratios are available in tables for various ions, energies, and sub-
strates. The available measurement techniques have been discussed in
the overview section of chapter I.

Computer Evaluation

Two programs have been written for use in solving the diffusion
equation. One actually solves the equation while the other is used to
evaluate that solution found by analytically solving the diffusion
equation (18).

The program that is used to solve the diffusion equation is called
LVCRV for L(V) curve versus voltage. Given the depth-dose curve from
EPIGA in the form of a data deck, LVCRV fits the depth-dose curve with a
least squares approximation by cubic splines with variable knots. It
prints out the voltage being run, the depth-dose curve from EPIGA and
the least squares depth-dose curve evaluated at the same points as in
EPIGA. The impurity profiles are computed in a subroutine called LSS.
There are provisions for handling five different profiles of any form.
Frequently, LSS profiles[17] (offset Gaussians) are used. The diffusion
equation is then solved for the excess carrier density. There is a
problem in that the boundary conditions are not specified at the begin-
ning of the problem. Thus one of the boundary conditions must be arbi-
trarily chosen. The equation is then solved. As the solution progresses,
the excess carrier density is checked for 'reasonableness." By "reason-
ableness" is meant that the solution does not go negative, nor increase

38

without bound. The solution should also transition into a decaying
exponential function after the depth-dose curve goes to zero. If the
solution does not meet these requirements, the initial condition is
corrected and the solution tried again. If the solution is not found in
fifty tries, that information is printed out along with the last attempt.
The next depth-dose curve is read in and the process repeated until all
of the depth-dose curves have been run. Finally, the L(V) curve is
calculated using the excess carrier densities and the impurity profiles
previously calculated. Each point on the L(V) curve is calculated from
equation (19) expressed in the form of

$$L(V) = \sum_{k=1}^{K_{MD}} LSSD(k) * EXN(k) * EXP[-ALPHA * X(k)]. \qquad (20)$$

LSSD(k) is the impurity density at depth X(k), EXN(k) is the excess
carrier density at the same depth, ALPHA is an absorption coefficient
and K_{MD} is the value for k that corresponds to $X(K_{MD}) = D$.

In order to remove variations in the experimental data from point
to point the experimental curves are normalized to an assumed uniformly
distributed impurity. When the analytical curves are normalized equa-
tion (20) is evaluated for a uniformly distributed impurity. Each point
on the normalized L(V) curve is computed by dividing the result of
equation (20) for the implanted impurity by the result for a uniformly
distributed impurity. After all of the points have been calculated, the
L(V) points are punched on cards to be plotted by another program,
PLOTLV.

The diffusion equation is solved using the Gear[75] ordinary differ-
ential equation solver package. The LVCRV program is capable of handling

39

both D_n and μ_n as functions of depth. This is the primary reason for using this approach. Since it takes LVCRV a very long time to execute even for constant D_n and μ_n (more than five (5) times program CHECK), another approach was developed that would execute faster.

This second approach is called CHECK. It utilizes the fact that the diffusion equation can be solved exactly. The solution to equation (18) is

$$\delta n(x) = N(o)[\cosh(X/L_n) + \frac{L_n S}{D^*}\sinh(X/L_n)] - \frac{L_n}{D^*}\int_0^X \sinh(\frac{x-y}{Ln})g_n(y)dy \quad (21)$$

where L_n = diffusion length = $\sqrt{D^*\tau_n}$ and

$$N(o) = \text{initial condition} = \frac{L_n}{D^*} (\int_0^\infty \exp[-y/L_n]g_n(y)dy)/(1 + L_n S/D^*)$$

This solution can be verified by substituting into equation (18).

Program CHECK is similar in many respects to LVCRV. The depth-dose curves are read into the computer in the same manner, the curves are fit by the same subprogram, and they both use the same criteria for a "reasonable" solution. There are differences. The first difference is that the initial condition can now be calculated. Unfortunately, the solution is very sensitive to the initial value. Thus the initial condition may have to be corrected in order to get a viable solution. The required changes, though, are very small, usually in the tenth to twelfth decimal place. The solution, $\delta n(x)$, also has problems when x gets greater than a few times L_n. The subtraction takes place between two almost identical numbers that are very large, to get a comparatively small $\delta n(x)$. Truncation error causes $\delta n(x)$ to oscillate badly under these circumstances. In order to avoid this condition, the decaying exponential solution is substituted for $\delta n(x)$. This solution matches equation (21) at the depth

at which the depth-dose curve has its last value prior to going to zero. The solution is checked to make sure it has peaked and started down before the exponential solution is forced on it.

The $\delta n(x)$ values calculated in CHECK are printed and stored in permanent files. An additional program, LVCRVA, accesses the permanent file, calculates the L(V) points as is done in LVCRV, scales the L(V) curves for plotting and plots them on the Cal-Comp plotter or other plotting device.

Results

As a confirmation of the correctness of the results of CHECK and LVCRV, L(V) curves were calculated. Figure (10) shows the results. The top curves are for LVCRV and the bottom curves from CHECK/LVCVRA. These curves are for various implant profiles. The bottom curve in each case is for a uniformly distributed profile. The next two curves are L(V) curves for two types of LSS profiles. The top two curves are the middle two curves normalized to the uniformly distributed profile as described earlier. The L(V) curves are the same in each case. In fact, both programs give the same results for $\delta n(x)$ to the five significant decimal places printed out.

Since neither D^*, τ_n or S are known in advance, a parametric study was performed to see how L(V) changes. A scaling relationship exists between the parameters that substantially reduces the number of runs required. Consider the diffusion equation (18) again,

$$D^* \frac{d^2 \delta n}{dX^2} - \frac{\delta n}{\tau_n} + g_n(x) = 0 \qquad D_n \frac{d \delta n}{dX}\bigg|_{X = 0} = S \delta n\bigg|_{X = 0}$$

41
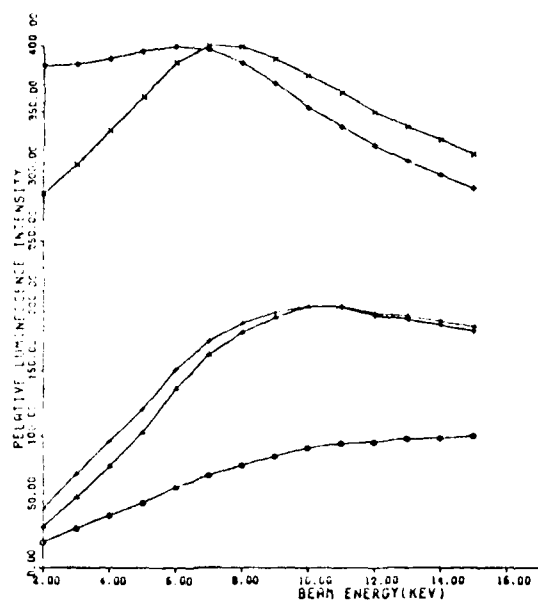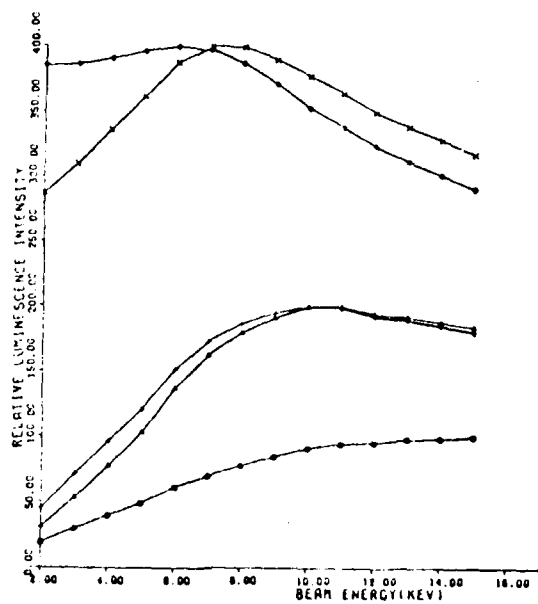
(a) LVCRV

(b) CHECK

Fig. 10 Comparison of L(V) Curves for LVCRV and CHECK

42

Let $D*$ increase by a factor of A, let τ_n decrease by a factor of $1/A$, and let S be expressed in units of $\sqrt{D*/\tau_n}$. Let y be the new solution. The diffusion equation becomes

$$AD*\frac{d^2y}{dx^2} - \frac{Ay}{\tau_n} + g_n(x) = 0 \qquad AD_n \frac{dy}{dx}\Big|_{x=0} = S\sqrt{A/(1/A)} \; y\Big|_{x=0} = ASy\Big|_{x=0} \qquad (22)$$

Let $\delta n = Ay$. Then (22) becomes

$$D*\frac{d^2\delta n}{dx^2} - \frac{\delta n}{\tau n} + gn(x) = 0 \qquad Dn\frac{d\delta n}{dx}\Big|_{x=0} = S\delta n\Big|_{x=0} \qquad (23)$$

This is the same equation as before. If $D*$ is multiplied by A, τ_n divided by A and S unchanged, then the solution δn is divided by A. Since the L(V) curves are arbitrary within a multiplicative constant, they appear unchanged. The physical significance is that the L(V) curves scale on the diffusion length given by $L_n = \sqrt{D*\tau_n}$ and not on $D*$ or δ_n individually. This also means that without an independent measurement of $D*$ or τ_n, fitting the L(V) curve does not indicate a value of either. This scaling was verified by running two programs with different $D*$ and τ_n, but with the same L_n and S.

The parametric study of the L(V) curves consists of runs where L_n, S, ALPHA (the absorption coefficient for the emitted luminescence) and the impurity profile are varied. The L(V) curves are the result of dividing the L(V) curve for the implant by the L(V) curve for a uniformly doped impurity. This is done on a point by point basis at each voltage where the L(V) curve is evaluated. This method of presenting the L(V) curves is dictated by experimental considerations where it is necessary to minimize variations from run to run by calibrating the

43
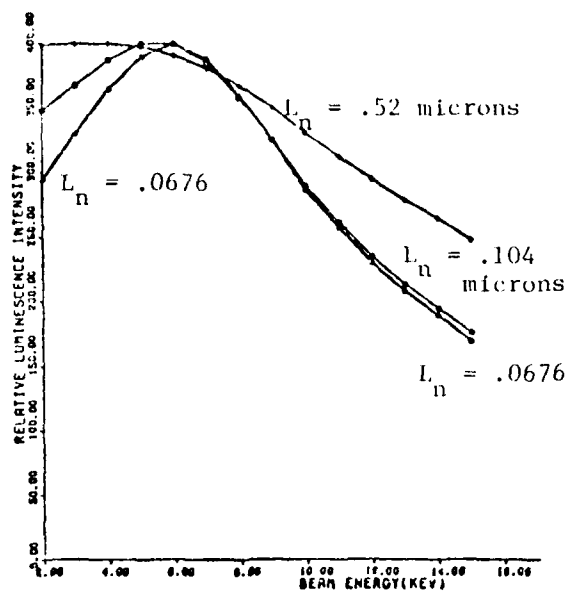
(a) Diffusion Length, L_n
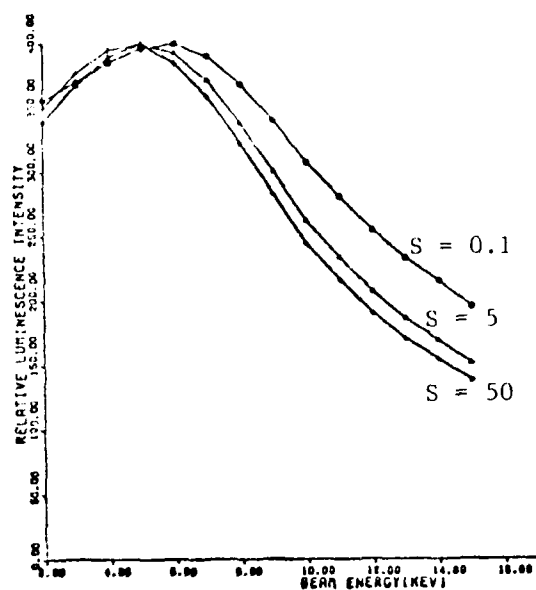
(b) Normalized Surface Recombination Velocity, S
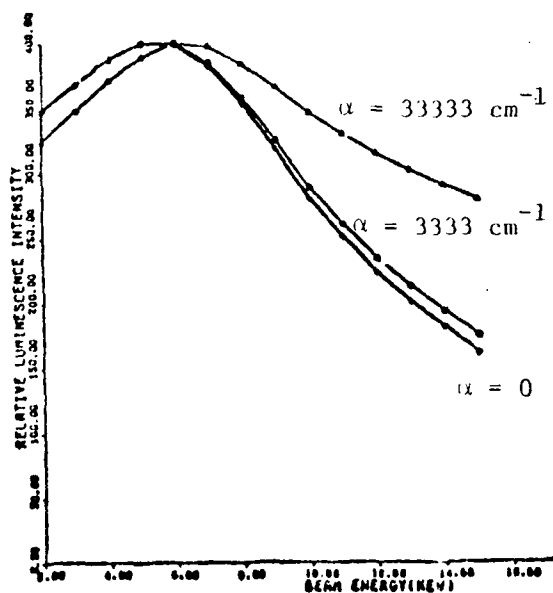
(c) Absorption Coefficient, α
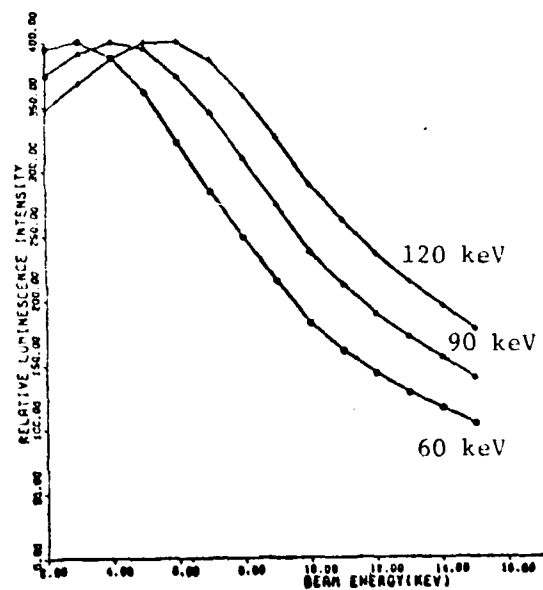
(d) Impurity Profiles

Fig. 11 L_n, S, α, and Impurity Profile Studies for L(V) Curves

44

system to a constant line. In figure (11) a series of runs with various combinations of L_n, S, ALPHA, and impurity profiles is shown. The peak values of all these curves are adjusted to 400 so that conclusions based on relative amplitudes between curves are meaningless.

The upper left hand figure shows how L(V) varies as L_n is changed over a factor of 30. The implanted impurity profile is the profile predicted by LSS theory[17, 20] for 120 keV Mg ions implanted into GaAs. As expected, the curve becomes more smeared out as L_n increases. This reflects a loss of detail in the implant profile. It also demonstrates what was obvious from the beginning: the shorter the diffusion length, the more detail of the impurity profile is indicated in the L(V) curve.

The upper right figure presents L(V) curves with S as a parameter. As the surface recombination velocity increases there is more non-radiative recombination at the surface so the initial parts of each of the excess carrier density curves (one for each beam energy) are reduced. This shifts the peak in the excess carrier density deeper into the GaAs. Now lower voltages are probing areas where higher voltages were probing before. The peak of the L(V) curve shifts to the left as S increases. The L(V) curve falls faster in the end because that is what happens to the excess carrier density as S increases. The curves are computed for L_n = .104 micron.

The figure in the lower left hand corner shows the variation of L(V) with ALPHA as a parameter. A higher ALPHA reduces the luminescence more from deeper parts of the GaAs to a greater degree than that from the surface. This effectively reduces the probing effect of the electron beam. Hence, higher voltages are required to probe deeper into the GaAs

45

to find the implant peak. The slope of the initial parts of the curve are the same; this indicates there has not been much change in this area. The overall reduction of the leading edge is due to an increase in the peak of the L(V) curve and the subsequent overall reduction that was done to scale the plot. The fact that the peak and tail of the L(V) curve is larger for higher ALPHA is at first surprising, since deeper effects are attenuated more. The reason is that the L(V) curve is actually the implant line divided by a uniformly doped impurity. The luminescence from the uniformly doped impurity is reduced more by the higher ALPHA than the implanted species. Thus the L(V) curves generated by the ratio of implant curve to doped curve stay higher for the higher ALPHA.

The last set of curves in figure (11) illustrates the variation of the L(V) curves with implantation profiles. The impurity profiles are LSS profiles for Mg ions implanted at 60, 90 and 120 keV into GaAs. The diffusion length is 0.104 microns. As expected, the L(V) curves for deeper implants peak at higher electron beam energies. The general shape of the curves are about the same.

In the beginning of this section it was shown that variations in the diffusion constant and recombination time do not change the shape of the L(V) curve as long as the diffusion length remains constant. Next, several parametric studies were made to see how the L(V) curves changed as the diffusion length, surface recombination velocity and absorption coefficient were changed. If these changes are all taken together, it is evident that some fairly complex changes can occur in the L(V) curves. Figure (11d) shows the possibility of distinguishing between different

46

profiles. This suggests that cathodoluminescence might be useful as a profiling technique on either an absolute basis where the profile is measured directly or on a qualitative basis where two samples are compared to see if there are any differences between them.

The next section, which is the last section of the chapter, summarizes the calculations necessary to compute the L(V) curve. That section is provided as a brief review of the chapter and as a quick reference for the calculation procedure.

Summary of Calculation

Figure (12) is a conceptual diagram of how the calculation of the luminescence versus beam voltage (L(V)) proceeds. As indicated in the introduction to this chapter, the calculation consists of three main parts. The first part is the Monte Carlo calculation. This is characterized by module (2). In this block the depth-dose curve, which is the rate of energy loss from the electron beam with respect to depth, is calculated. The calculation is done by a computer program called EPIGA. Two arbitrary parameters, η, the screening parameter for the nuclear charge by the orbital electrons and ΔS_o, the initial step size for the Monte Carlo simulation, are adjusted to give the best agreement with Wittry and Kyser's data for the backscattering fraction of a 30 keV electron beam penetrating into GaAs. This gives good agreement with Martinelli and Wang's data for electron beam penetration through thin films of GaAs.

Next, the depth-dose curves are used as inputs to block (3) which calculates the excess carrier density. This is the result of solving the diffusion equation. In this calculation both the diffusion constant

47

and recombination time are held constant. For depths below the depth at which the depth-dose curves to to zero, the excess carrier solution is forced to a decaying exponential. The implementation of this solution is done in two ways depending on which of the two methods is used to calculate the excess carrier density.

The first method solves the diffusion equation numerically using the Gear differential equation solver package. This method is capable of handling both a depth dependent diffusion constant and recombination time. These features are not presently used as the value of the calculation cannot justify its cost at the present time. In the second method, the diffusion equation is solved exactly and the solution evaluated numerically. This method is faster than method one, but cannot handle a depth dependent diffusion constant or recombination time. As explained earlier the program to implement the first method is called LVCRV and the second is called CHECK. The solutions for either method agree to within the accuracy of the computer.
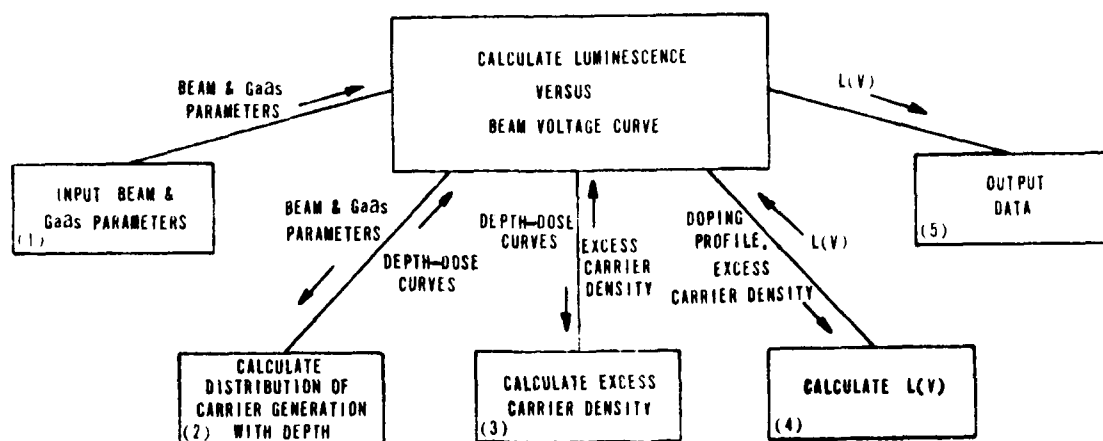
Fig. 12 Conceptual Diagram of How the Luminescence Calculation Proceeds

In module (4), the L(V) curve is calculated following equation (20). This requires the excess carrier density and the implantation profile be multiplied together at each depth into the GaAs. An exponential absorption factor is assumed for the recombination radiation. This module is contained in program LVCRVA if program CHECK is used to calculate the excess carrier density. It is a part of LVCRV if that program is used.

In module (5) the data output is produced. This consists of plots of the L(V) curves. The plots are all scaled so that they fit onto the same axis. This module is contained in LVCRVA if CHECK is used or in PLOTLV if LVCRV is used.

The modularization of all the separate parts of the calculation has made it easy to shuffle subprograms back and forth. Thus modules (4) and (5) were combined to produce LVCRVA and modules (3) and (4) were combined for LVCRV. The isolation of one module from another made this possible.

III. The Experiment

This dissertation has as its primary purpose the attainment of some quantitative agreement between the variation of the measured luminescent intensity as a function of electron beam energy and the same variation determined from a model of ion implanted GaAs. In order to do this, a facility needed to be designed that could measure luminescence from a particular set of lines. Certain features needed to be incorporated in this system in order to get any kind of consistent results. These include: an electron beam which can be easily and repeatably controlled, a beam current density which must be uniform across the sample, and an optical system which should be insensitive to small variations in position. These requirements were met to some extent by the system used by Walter[6]. The system was further modified to meet the particular needs of this experiment.

Epitaxial GaAs was chosen as the material into which to do the ion implantation. The epi-layer GaAs should have a simpler spectrum than the substrate material previously studied. Magnesium was selected as the implant species since it penetrates deeper into the GaAs than the common p-type dopants Zn and Cd[17, 20]. This was thought to give a better opportunity for profiling with cathodoluminescence. Also, Mg had not previously been studied in GaAs epi-layers, although it had been implanted into substrate quality GaAs.

In the first section of this chapter a description of the system that was set up to meet the particular needs of this experiment is given. Also included is a brief description of the operating procedures

used. The next section provides some background on Mg doped and implanted GaAs. The final section contains a discussion of the samples and how they were processed.

Experimental Arrangement

The cathodoluminescence system can be broken down into four parts. These are the electro-optical column, the vacuum system, the sample mounting and cooling system and the signal processing system. A description of each part of the system and how it interfaces with the other parts is given in the following sections. A short description of the operating procedures used with this system concludes this section.

Electro-optical Column

A sketch of the complete system is shown in figure (13). The electro-optical column consists of the vacuum chamber, the steering and focus coils, and the electron gun system. The electron gun is a B-91-16A35 unit manufactured by Hughes Aircraft Company. The electron gun is attached to a circular eight-pin connector which plugs into the eight pins of the glass envelope surrounding the gun. A centering clip is attached to the anode to center the gun in the glass envelope and also provide a ground connection for the anode. There are two grids on the electron gun. The grid voltages are variable but usually G1 is about -15 volts and G2 is +500 volts. The electron gun is operated at pressures ranging from 5×10^{-7} torr to 1×10^{-6} torr.

After the electron beam leaves the gun, it passes through an aperture positioned in the center of a 45° mirror. Interchangeable stainless steel apertures are provided with diameters of 5, 8, 10, 12 and 15 mil.

51
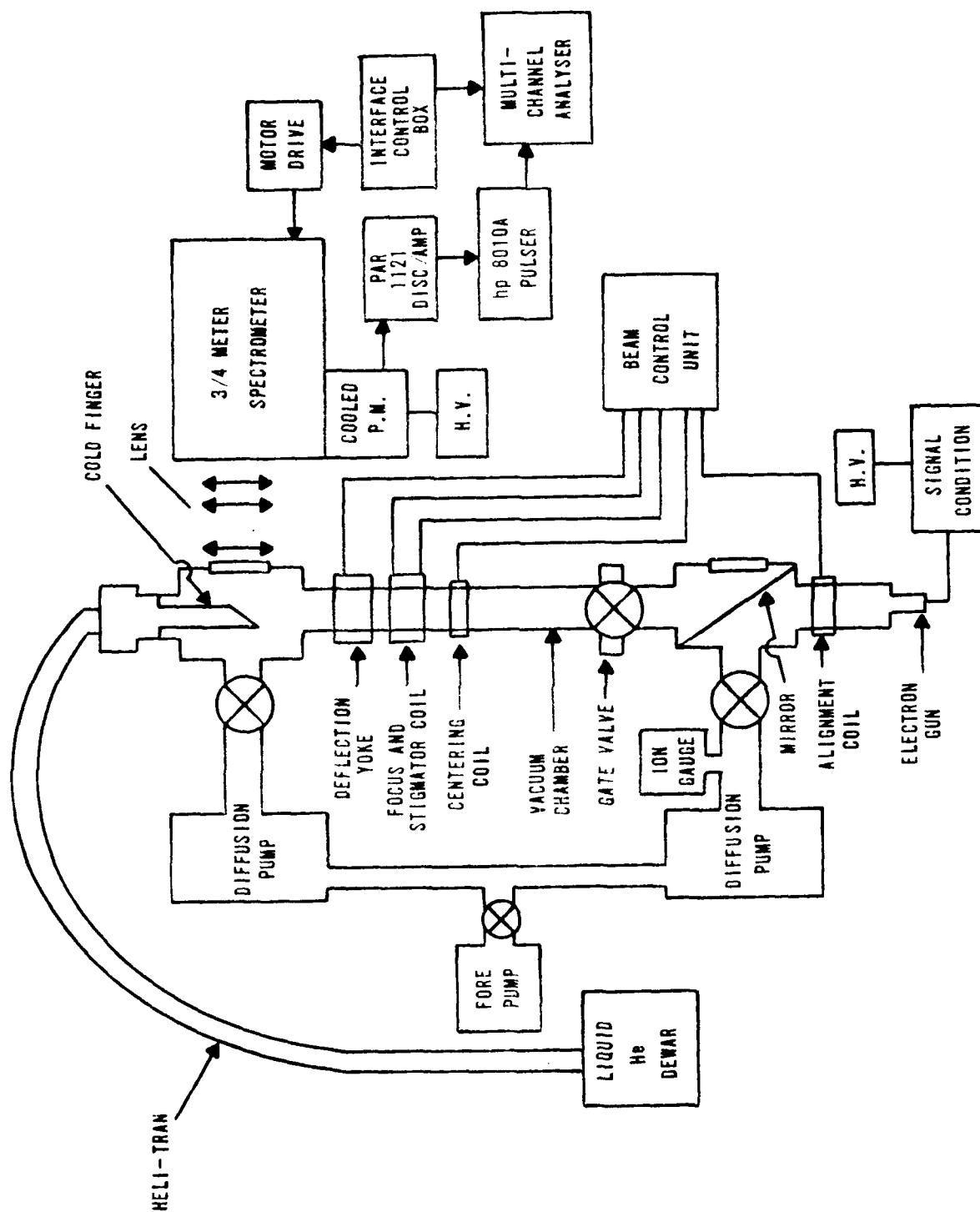
Fig. 13 Cathodoluminescence System Diagram

These apertures were not used since they reduce the amount of current the gun can deliver to the target. The mirror is positioned so that it is possible to look straight up the column to the samples. The electron gun housing is in a sliding mount below the mirror block. This mount may be moved transversely on a sliding O-ring seal. This corrects for misalignment of the electron gun.

There are five sets of magnetic coils that the beam passes through before it reaches the target. They are the alignment coils, centering coils, focus coil, stigmator coils, and deflector coils. The coils are all connected to D.C. power supplies capable of providing at least 200 milliamps into the coils. All but the focus coil have coils for both horizontal and vertical beam adjustments. The alignment coils are on the electron gun housing and slide with it. Coupled with manually sliding the gun, the alignment coils are used to get the maximum current and most uniform spot through the aperture. This is determined by viewing the electron beam on a movable flap that has a zinc-oxide crystal mounted on it. The flap is located at a position immediately after the beam passes through the aperture. The centering coils are used to position the beam on the axis of the focus coil so as to get the most uniform spot on the target. The current through the focus coil is adjusted so that the beam is defocused. The spot size is enlarged until the spot covers the entire sample exposed to the beam. This is necessary so that the current density at the surface of the GaAs can be approximately controlled. Later, it will be shown that failure to control the current density makes a considerable difference in the spectrum. The stigmator coils correct for any stigmatism in the beam. It was not necessary to

use the stigmator coils. The deflection coils are used to steer the beam onto the target and into the Faraday cup. A switch is used to select which of two sets of two power supplies is connected to the coils. This allows the beam to be conveniently switched from the sample to the Faraday cup and back. The focus coil and the stigmator coils are located on a micropositioner that features pitch and yaw tilt adjustment and two axis translation. The deflection yoke is mounted on a similar micropositioner that also allows for rotation of the coils.

The beam current is measured by means of a Faraday cup and a Keithley 414A picoammeter. The beam enters the cup through an 1/8 inch diameter hole. This is the same size hole that is in the shield that holds the samples in place. By defocusing the beam so that it covers the entire hole and by assuming the beam to be uniform across the spot, the current density can be adjusted to any desired value. Any variation in the uniformity of the beam cross-section is accounted for by adjusting the position of the beam on the cup to maximize the current reading and on the sample to maximize the luminescence to the photomultiplier. This adjustment allowed the amplitude measurement of the luminescence to be repeated to within 10% for subsequent measurements that were immediately repeated. The shield over the entryway to the Faraday cup is kept at the negative grid voltage of the suppression screen.

Vacuum System

Figure (13) includes the major components of the vacuum system. Reference to this diagram shows how the system components interrelate. The two diffusion pumps allow the samples to be changed without bringing the gun up to atmospheric pressure.

54

Sample Mounting and Cooling

The sample mounting is the same as has been used in the past. Four GaAs samples are mounted on the face of a copper block that has been cut at a 45° angle to the electron beam axis and the horizontal axis of the spectrometer. The samples are held in place with copper brackets that are attached with screws to the copper block. The brackets have an 1/8 inch diameter hole in them to allow the electron beam to strike the sample and the luminescence to be collected. The brackets are coated with aquadag to minimize reflection from the electron gun filament. A Faraday cup is mounted at the top of the face of the copper block.

An Air Products Heli-Tran system is used to cool the samples. Liquid helium flows through the tip of the transfer tube, cooling the copper block. The temperature of the copper block is monitored with a chromel vs. gold .07 atomic % iron thermocouple using a liquid nitrogen reference. A Data Precision 3500 digital voltmeter is used to record the temperature in microvolts.

Signal Processing

The luminescence from the sample is collected by a three lens system as shown in figure (13). The lens closest to the samples has a focal length of 10 cm and is positioned approximately this distance from the samples. The other lenses are in the same mount with a fixed separation of 8 cm. They were positioned near the spectrometer slit and adjusted to maximize the output signal. The lens closest to the slit has a focal length of 6.5 cm and the other lens a focal length of 25 cm. Between the second and third lenses is a number 650 Spectracoat Varipass filter. It is used to prevent any of the incident radiation below 6500 $\overset{\circ}{A}$ from entering

55

the spectrometer. Stray light from the filament is also reduced by sur-

rounding the electron gun with a shroud made from a black cloth.

The luminescence is focused onto the input slits of a Spex model

1702 Czerny-Turner spectrometer. A 200 micron slit opening is used. A

600 grooves/millimeter Bausch and Lomb grating blazed at 1.6 microns is

used in second order to disperse the luminescence. The efficiency of the

grating is estimated to vary by about 10% over the range of wavelengths

of interest here, being more efficient at the longer wavelengths. The

luminescence is detected by an RCA C7000A photomultiplier tube with an S-

1 response. The response changes by about 10% over the same wavelength

range, decreasing for longer wavelengths. Thus the two responses tend to

cancel each other, making the response of the system relatively flat over

the frequency range used here. The tube is cooled to -50°C using liquid

nitrogen. The temperature is maintained at this value by a Products for

Research temperature controller. The output of the detector is amplified

by a PAR 1121 discriminator/amplifier. While the discriminator/amplifier

provides many other functions such as pulse height analysis, window

scaling, and pulse pile-up correction, the unit is operated in the single

mode. In this mode only pulses greater than a pre-set level are detected

and sent on to the next stage. The pre-set level is determined by a

trial and error procedure that maximizes the number of signal counts

while minimizing the number of noise counts. Once this level is selected,

it is not changed during the experiment.

The next step in processing the signal is to shape the pulses so

that they are compatible with the input to the multichannel analyzer.

The Hewlett-Packard 5400A multichannel analyzer used in this experiment

requires pulses of at least 4 volts height and 25 nanoseconds width. A
Hewlett-Packard 8010A pulser operating in the negative, external trig-
gered mode is used for pulse shaping and interfacing between the dis-
criminator/amplifier and the multichannel analyzer.

The multichannel analyzer is operated in the MCS mode. In this mode
the pulses from the pulse generator are counted for a specified length of
time either with an internal or external time base. The number is stored
in one channel of the unit's memory. This process is repeated over and
over until all of the channels have numbers stored in them. The analyzer
has 1024 channels of memory. For this experiment, the multichannel
analyzer is operated under the external controls of an interface control
box (see figure 13). This device determines the length of time in which
pulses are counted for each channel. This controller is also used to
drive the spectrometer, thus synchronizing the spectrometer and the
multichannel analyzer. The controller has been described elsewhere[4]
and hence will not be repeated here.

The data stored in the multichannel analyzer is read out on to paper
tape. The paper tape is taken to a computer terminal site where the tape
is converted to punched cards. The cards are used in a computer program
that produces an output via a Cal-Comp or similar plotter. The plots are
of arbitrary intensity versus wavelength. The abscissa of the plots is
calibrated using a mercury lamp to provide a calibration line over the
spectrum when the original GaAs luminescence is recorded. The 4046.6 $\overset{\circ}{A}$
Hg line is used in second order for the calibration line.

Operating Procedures

In this section the procedures used during the experiment are explained. The purpose of the section is, (a) to simplify follow-on experiments that use the equipment and, (b) to describe the operating conditions under which the data is taken.

The first step is to choose the four samples to be measured and put them in place. The samples already in the chamber (assuming there are samples in the chamber) are isolated from the vacuum pumps by means of the gate valves. That portion of the chamber containing the samples is isolated from the electron gun section and brought up to atmospheric pressure by filling the chamber with nitrogen. The cold finger is removed and the samples changed. The procedure is reversed to get the samples back into the chamber.

The samples are then cooled using the Heli-Tran system. The system temperature is let fall to its lowest level. The liquid helium flow is then reduced to just maintain this temperature. The estimated sample temperature is 10°K.

Next, the electron beam is directed onto a sample. The optical system is aligned using the luminescence from the sample as a source. With the system aligned, the electron beam is switched to the Faraday cup (see the Electro-optical Column section). The beam current is adjusted to the desired level (usually 5.0 microamps) with the beam spot defocussed to cover the entire opening in the Faraday cup shield. The beam is steered onto the cup to give the maximum reading. The beam is then switched back to the sample and the current to the deflection yoke adjusted to steer the beam into a position of maximum luminescence at a particular line.

The data is now recorded in an hp-5400A multichannel analyzer. Sometimes the entire band of luminescence from 1.3 to 1.5 eV is recorded. At other times only certain lines, as for example, the Mg complex and the copper complex, are recorded. When all 1024 channels of the analyzer are filled, the data is transferred to punched paper tape and then to punched cards. These cards can be used in a program for plotting the data.

Plots of the luminescence are then analyzed on a Dupont 310 line-shape simulator. This device takes up to six waveshapes and combines them together to get a composite line. This composite line can then be compared to the real line. Thus competing lines can be resolved by adjusting the individual lines making up the manufactured composite line until it matches the complex waveshape. The other lines can be switched off leaving only the one line to study. The device also determines the area under the curve. This is the integrated lineshape and corresponds to the total number of transitions through that center per unit time. The L(V) curves are calculated by taking the ratio of the area under the Mg curve to the area under the Cu curve at each voltage.

Mg/GaAs Luminescence: Previous Results

The first reported case of Mg being implanted into GaAs seems to have been by Hunsperger et al[76]. They implanted Be and Mg at 45 keV into n-type ($n = 1.0 \times 10^{16}/cm^3$) GaAs substrates. The implantation was done at room temperature with subsequent annealing at temperatures from 100-900°C. The implanted GaAs was capped with a 2000 Å thick layer of SiO_2 prior to annealing. They determined that the p-type layer was approximately 0.4 microns, whereas LSS theory predicted 0.12 microns. They concluded that some ion channeling or diffusion had occurred and

59

that it could not be assumed that the implanted layer had a Gaussian shape as predicted by LSS theory.

Yu and Park[77] used photoluminescence to study the luminescent behavior and the annealing characteristics in Mg ion implanted substrate materials. Si-doped and Cr-doped semi-insulating substrates were used, with the Mg ions being implanted directly into the substrates. Emission spectra were obtained at 4.2K for implanted doses of from $5 \times 10^{12}/cm^2$ to $1 \times 10^{15}/cm^2$ and for annealing temperatures of 450 to 900°C. The conclusions were that the optical ionization energy of Mg is 28 ± 2 meV and that annealing temperatures from 750-900°C are enough to optically activate implanted Mg ions and to remove lattice damage. The luminescence from the Si-doped GaAs showed three bands. One band at 1.513 eV was attributed to impurity-exciton complexes. The middle band that occurred at various places between 1.493 to 1.489 eV was identified as free electrons recombining with holes bound to acceptors. The lower band comes from electrons bound to donors recombining with holes bound to the same acceptors as before. The position of this band was very much intensity dependent, centered around 1.464 eV. Similar results were obtained for the Cr-doped substrate except that the lowest band did not occur at a lower annealing temperature (750°C).

In a follow-on paper[78] the temperature dependence of photoluminescence from Mg implanted GaAs was studied. The same samples as in reference (77) were used. In addition, an undoped, n-type substrate implanted with Mg was studied. Again the major observed bands were from free electrons recombining with holes bound to Mg acceptors and from donor-acceptor pair recombination. The dose dependence of the emission characteristics,

60

the temperature dependence of emission bands involving Mg, and the donor-acceptor pair band were all studied. The depth distribution of Mg acceptors obtained by successive etchings indicated that Mg acceptors were distributed to about 0.65 microns for samples annealed at 900°C. The LSS depth for the 100 keV implant is 1030 $\overset{o}{A}$ with a straggling of 460 $\overset{o}{A}$. Yu and Park conclude that the disparity is caused by diffusion of the Mg ions during annealing.

In a more recent paper, Yu[79] discussed the excitation dependent emissions in Mg, Be, Cd, and Zn implanted GaAs with respect to changes in temperature and excitation intensity. He observed the donor-acceptor pair emission in the impure-compensated crystals shift to lower energy with a temperature increase in the range of 4-50K while the donor-acceptor pair emission in pure crystals behaves in the usual manner. The large shift of the emission peaks is thought to occur in the impure, compensated regions.

Zolch et al[80] studied implants of Be, Cd, Mg and Zn in GaAs and $GaAs_{1-x}P_x$. For Mg implants of doses between 10^{14} and $10^{16}/cm^2$ they observed a reverse annealing at temperatures between 650°C and 750°C. By this they mean the effective mobility decreased for annealing temperatures in this range. They also observed that a higher electrical activation and a smaller reverse annealing effect can be obtained if Si_3N_4 passivation is used rather than SiO_2. Annealing was done in a nitrogen atmosphere. The reverse annealing effect was attributed to outdiffusion of Mg and not complex formation since outdiffusion is reduced with Si_3N_4. Annealing above 800°C was required before the mobility of the implanted layer approaches the bulk value. They found the diffusion constant of Mg to be (kT in eV)

$$D = 4.4 \times 10^{-4} \exp (-1.87/kT) \ cm^2/sec.$$

Unfortunately, they did not report their profile measurements for Mg.

Samples

Mg implanted epitaxial GaAs was chosen for study to compare experimental with theoretical results for the luminescence versus voltage (L(V)) curves. Epitaxial GaAs was chosen since the spectrum from epilayers should be simpler to interpret as there are less competing losses. Mg was picked for the implant for two reasons. First, no previous work had been done with Mg implanted, epitaxial GaAs. Second, the LSS projected range (appendix A) of Mg ions is from .06 to .12 micron for the implant energies available to us. This is about the same depth as that of the peak of the depth-dose (see fig. 3 and 5-9). Having the peak of the depth-dose curve shift through the peak of the implant profile increases the chances of profiling.

GaAs epilayers were implanted at fluences of 1E12, 5E12, 1E13, 5E13 and 1E14/cm^2. The implant energies used were 60, 90 and 120 keV. The samples were then capped with a layer of Si_3N_4, annealed, and stripped of the Si_3N_4 layer. Finally, some were profiled using Hall measurements coupled with repeated etchings. These topics in more detail in the following sections.

Growing

The epi-layers were grown on a chromium doped GaAs substrate using a vapor phase epitaxial growth technique. They were grown by G. McCoy of the Electronics Research Branch of the Air Force Avionics Laboratory at Wright-Patterson Air Force Base. An open flow chemical vapor transport

62

system employing the reagents arsenic trichloride, gallium, and hydrogen was used. The system is described in more detail in reference (83). The epilayers were p-type with a room temperature carrier concentration of 7.94×10^{14} cc^{-1} and an effective mobility of 399 cm^2/v sec as determined by Hall measurements.

Implanting

The epilayers were implanted by J. Ehret of Systems Research Laboratories using the ion implantation system at the Avionics Laboratory. Before implanting, the samples were cleaned in methanol. A hot cathode ion source of solid Mg was used as a source of Mg. The Mg ions were separated from the other ions by a magnetic separator. The Mg ions were then accelerated to the required energy for implantation into the samples. More information on the system is contained in reference (84).

Table II provides a listing of the GaAs samples available for study. A large number of samples was needed since it was not known beforehand which implant energy and fluence would give the best L(V) curve. It was felt that the mid-range doses would be best since too low a dose decreases the amount of luminescence and too large a value leads to impurity banding (which is another complication in the interpretation of the data). The unimplanted/annealed and the unimplanted/unannealed samples were used as references to see the effects of implanting and annealing and to aid in the identification of the lines in the implanted samples.

Annealing

Table II shows the conditions under which the samples were annealed. Si_3N_4 caps were used since at the time chose were giving the most repeatable

Table 11

Samples Available for Study

Implant Energy (keV)	Dose (cm^{-2})	Annealing Condition
60	1E12	A
	5E12	A
	1E13	A
	5E13	A
	1E14	A
90	1E12	A
	5E12	A
	1E13	A
	5E13	A
	1E14	A
120	1E12	A
	5E12	A
	1E13	A
	1E13	B
	1E13	C
	1E13	D
	5E13	A
	1E14	A
None	None	A
None	None	None

A – Si_3N_4 cap/15 minute anneal at 850°C/cap removed

B – Same as A but 750°C anneal

C – Same as A but 800°C anneal

D – Same as A but 900°C anneal

results[85]. The 850° anneal for fifteen minutes was somewhat arbitrarily set. It has been shown[76, 77] that annealing at temperatures greater than 750°C is sufficient to obtain excellent electrical properties and efficient luminescence from Mg acceptors. The usual anneal time has been fifteen or twenty minutes[76, 77, 78]. The samples to be annealed were covered with a pyrolytically grown film of Si_3N_4 approximately 1000 Å thick. They were then placed in a spectrosil boat and annealed at the required temperature in flowing hydrogen. After the samples cooled, the caps were removed using hydrofluoric acid with trichloroethylene, acetone and de-onized water rinses. It was decided to remove the caps in order for the peak of the electron beam to probe as deeply as possible into the sample.

Electrical Profiling

After the L(V) curves were obtained, the 5E13 cm^{-2} at 120 keV and the 5E13 cm^{-2} at 90 keV samples were profiled using a Hall system with repeated chemical etchings. The implant density was determined about every 150 to 200 Å. The volume concentration of charge carriers and the mobility can then be calculated as a function of depth. The profiles were measured by Y. K. Yeo of the Electronics Research Branch. Figure (14) shows the results for the 120 keV, 5E13 cm^{-2} and the 90 keV, 5E13 cm^{-2} implant. The points show considerable scatter compared to other profiles on similar samples. The implications of this will be developed further in the chapter on results. With this equipment and these samples, the required data can be acquired. This data is reported in the next chapter.
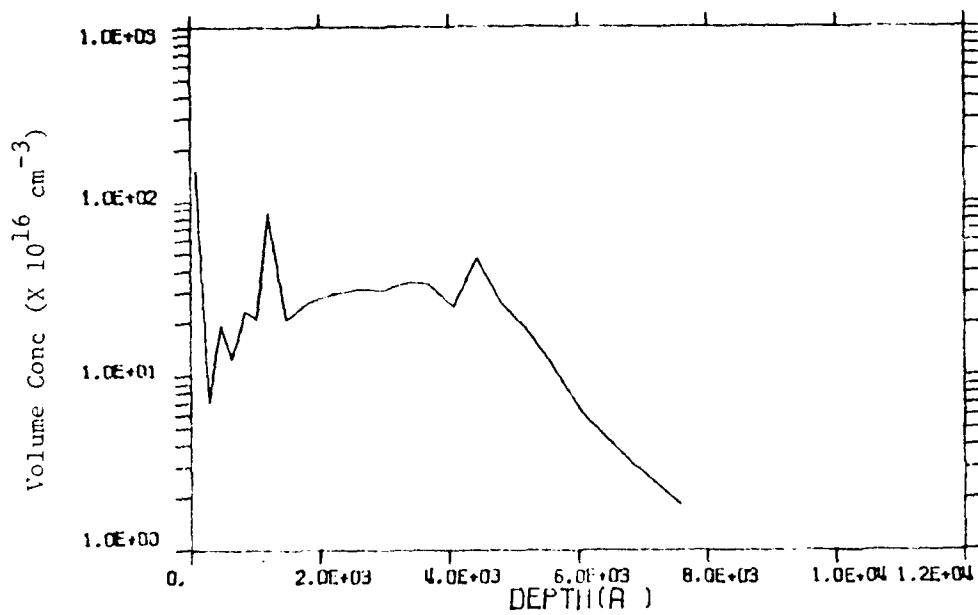
(a) 90 keV
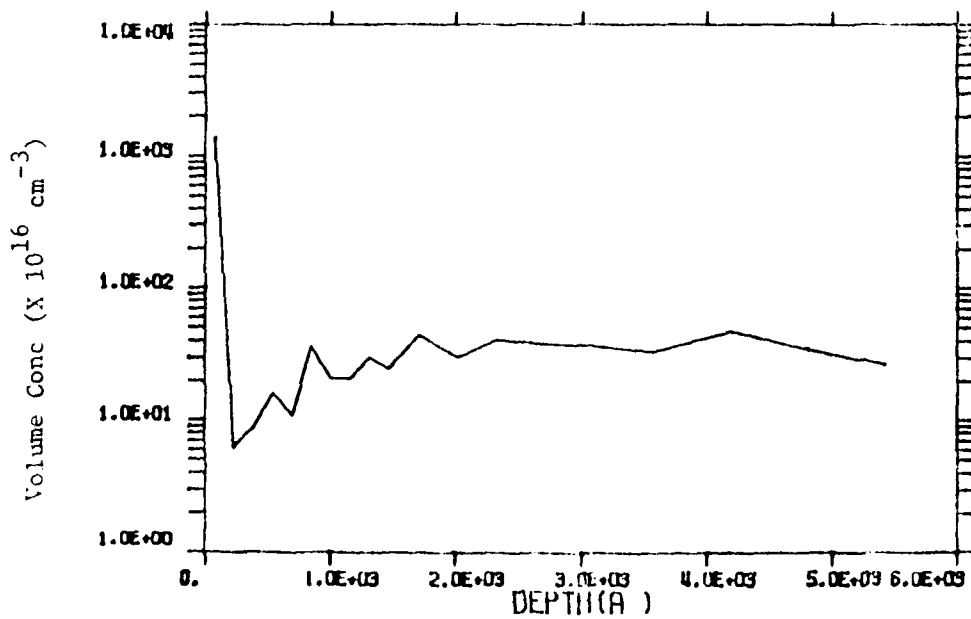
(b) 120 keV

Fig. 14 90 and 120 keV Mg Implanted GaAs Profiles by Yeo[74]

66

IV. Results

This chapter contains both the results obtained using the system described in the last chapter and the comparison of the experimental and analytical L(V) curves. First, the spectrum from Mg ion implanted GaAs is analyzed. Various lines between 1.3 and 1.5 eV are identified. It is shown how depth resolved cathodoluminescence can be used to identify lines by determining where the concentration of the impurity is maximum. Next, a study is conducted of the spectral variation with current density. A possible explanation for this variation is given. The reason that this variation is important to depth resolved cathodoluminescence is discussed and the proper action taken to minimize its impact is given. The L(V) curves are presented in the third section. In the final section the analytical and experimental L(V) curves are compared. The physical parameters chosen for the analytical curves are justified based on other workers' results.

Spectrum Identification

Figure (15) shows the spectrum obtained from a GaAs epilayer implanted at 120 keV to a dose of $5E13$ cm^{-2} with Mg ions. The spectrum was obtained with a 15 keV beam of electrons at a 5 microamp Faraday cup current. (The total cup current will usually be specified instead of the current density. In all cases, the beam of electrons was defocused to cover the entire entrance aperture to the cup so that when the total cup current is the same, so is the current density for a uniform beam is also identical.) The spectrum has not been corrected for the response of the detector, although the response should be approximately flat over this frequency range.

ENERGY (ELECTRON VOLTS)

1.55 1.48 1.42 1.37 1.31 1.26 1.22

1.513
1.492
1.455
1.408
1.960

RELATIVE MAGNITUDE (ARB UNITS)

X5

800.   896.   872.   908.   944.   980. 1016.
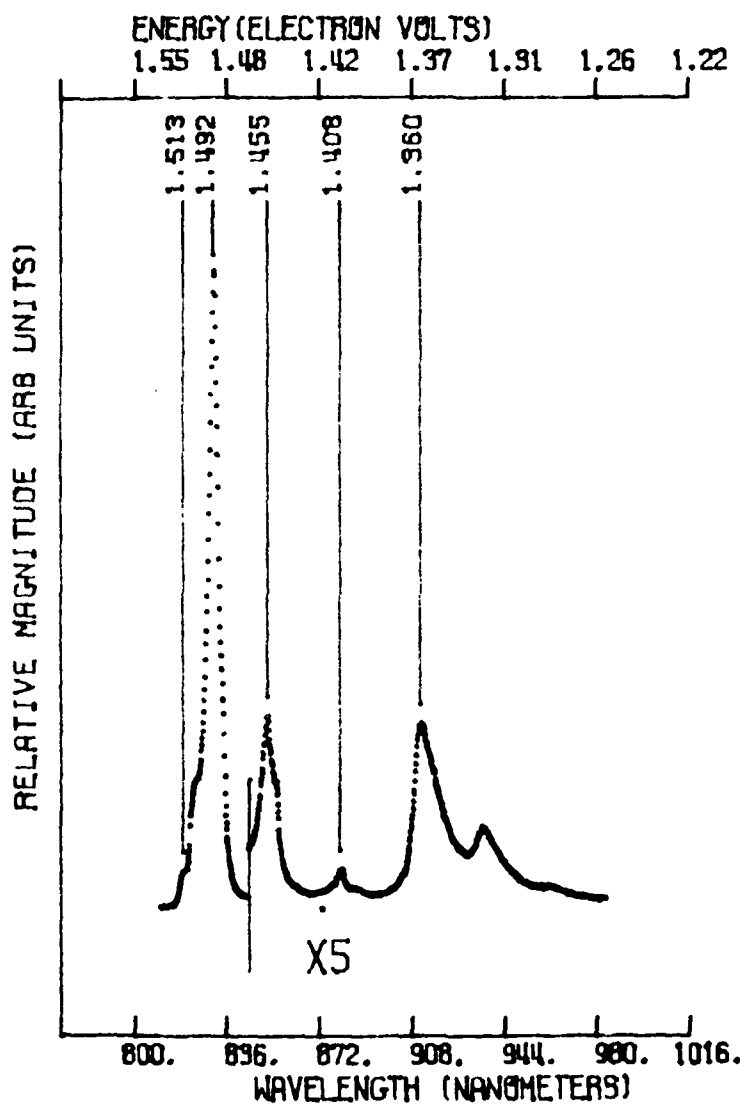
WAVELENGTH (NANOMETERS)

Fig. 15   GaAs Spectrum - 120 keV/5E13 cm^{-2} Mg Implant
15 keV/5 microamp Electron Beam

68

In general, there are four or five bands of luminescence. The 1.360 eV line has been attributed either to copper[77, 86, 88, 102] or to an As vacancy bound to an acceptor[103]. A 1.350 eV line[108] has been identified but it is too far from 1.36 eV to be considered. Chiang and Pearson found that the peaks could be enhanced with Cu diffusion or annealing in Amersil quartz, but were absent in samples annealed in Spectrosil quartz. The peaks at 1.325 and 1.288 eV are longitudinal optical phonon replicas of the 1.360 eV line. References (87) and (89) show that the peaks they studied follow a Poisson distribution. The ratio of the peaks in this study approximately follows that ratio (see table III). Thus the line at 1.36 eV is the same line as the copper line identified by Queisser and Fuller.

Table III

Ratio of 1.288 eV and 1.324 eV Peaks to 1.360 eV Peak

Peak	Experimental Ratio	Poisson Ratio
1.325 eV	.424	.43
1.288 eV	.118	.09

The identity of the line at 1.408 eV is not clear. It is present in the unimplanted/capped and annealed sample and all of the implanted/capped and annealed samples. It is absent in the unimplanted/unannealed sample. The line is not associated with a vacancy complex as the annealing process would be expected to reduce its intensity. A line at 1.408 eV has been associated with Mn or Pb[88]. The line at 1.400 eV is considered a transverse acoustic (TA) phonon replica of the 1.408 eV line.

69

In addition to its energy spacing, it is not present in the spectrum when the 1.408 eV is not there. Other samples measured have a weak LO phonon replica from the 1.408 eV line. This structure is similar to that shown in references (87) and (90) for Mn. Otherwise there does not seem to be any particular reason to choose Mn or Pb. Since the spectrum of the unimplanted/unannealed samples does not have the 1.408 eV line, it must originate in the implantation or annealing process. Examining the ratio of the 1.408 eV line's intensity to the copper line's intensity as the beam voltage (and hence probing depth) is varied should give some idea whether the intensity originates primarily near the surface or from deeper into the epilayer. This would indicate whether the impurity diffused into the epilayer from the surface or the substrate. Table IV shows the ratios for two samples. The conclusion is that the impurity diffused into the epilayer from the front surface during either the capping or annealing.

Table IV

Ratio 1.408 eV/Cu Line

Beam energy (keV at 5 microamp)	Sample 1	Sample 2
5	.453	x
7.5	.247	x
10	.178	.25
12.5	.117	.216
15	.104	.132

Sample 1: 90 keV Mg/1E13 cm^{-2}

Sample 2: 90 keV Mg/1E14 cm^{-2}

The complex around 1.49 eV is made up of lines at 1.486, 1.490, and 1.492 eV. The 1.490 eV peak seems likely to be due to Zn since Ashen et al[91] reported finding zinc in over 95% of their vapor phase samples with the other 5% probably having it. They report the peak at 1.4888 eV but pulling of the peak by the much stronger peak at 1.492 eV seems likely. The Zn line is present in all of the samples including the unannealed/unimplanted and the annealed/unimplanted. The 1.492 eV line is assigned to Mg. The line energy to four significant digits is 1.4918 eV. The assignment in Ashen, et al is 1.4911 eV (± .0003 eV). The uncertainty in the position of the peak is about ±1 channel (± .0004 eV). The thermal distribution of electrons in the conduction band subtracts $\frac{1}{2}kT$ from the energy of the line (see Ashen). This brings the energy assignment well into agreement. This line is absent in both the unannealed/ unimplanted and annealed/unimplanted samples.

The line at 1.486 eV could be Si[91], Cd[91] or a donor-acceptor pair with the 1.492 eV line[98]. Since the line at 1.486 eV is present when the 1.492 eV is not, the donor-acceptor pair assignment is ruled out. As for Si or Cd, the line is assigned to Si. In the unimplanted/ annealed sample the 1.486 line is much stronger than the 1.486 line in unimplanted/ unannealed sample. This is attributed to diffusion of Si into the sample during the capping and annealing. Also if the Si is coming in from the cap, the silicon line should grow compared to the other lines as the electron beam probes shallower depths. This is clearly seen in the sequence of runs shown in figures (17) and (18). In these figures the 1.486 eV line clearly increases compared to the Zn line as the beam energy decreases, hence probing shallower depths. Figures

(17) and (18) not only support the Si assignment, they also demonstrate the profiling possibilities of cathodoluminescence.

The line at 1.449 is a TO phonon replica of the line at 1.486 eV. The energy spacing is .037 eV which is approximately the LO phonon energy [87]. The lines at 1.455 and 1.453 eV are also .037 eV below the lines at 1.492 and 1.490 eV, respectively, and are also phonon relicas. In some samples the lines around 1.45 eV showed the exact shape of the lines around 1.49 eV (see figure 16). When the 1.492 eV line is absent from the spectrum, so is the line at 1.455 eV.

The line at 1.504 eV is unknown at present. It is absent from the samples that were not implanted with Mg, leading to the conclusion that it is associated with Mg. On the other hand, it is also missing from some of the Mg implanted samples. It is 9 meV from the 1.513 eV line, which suggests it might be a TA phonon replica of that line. The problem is that the 1.513 line is present in the unimplanted samples and the 1.504 line is not. The line has not been reported in the other studies of Mg-doped or implanted GaAs. When the 1.49 eV complex was resolved on the Dupont 310 lineshape simulator, the 1.504 line was found to be fairly broad compared to the other lines. There is no guarantee however of the uniqueness of the fit obtained from the simulator in resolving the lineshape into its component lines.

The 1.5133 eV line has been identified by Yu and Park[77] and Bogardus and Bebb[92] as an impurity exciton complex. In particular, it is associated with some unknown donor or donors[92]. At one time this line was thought to come from a free-exciton emission. The energy of the line is closest to the exciton-ionized donor line in Bogardus and Bebb[92].
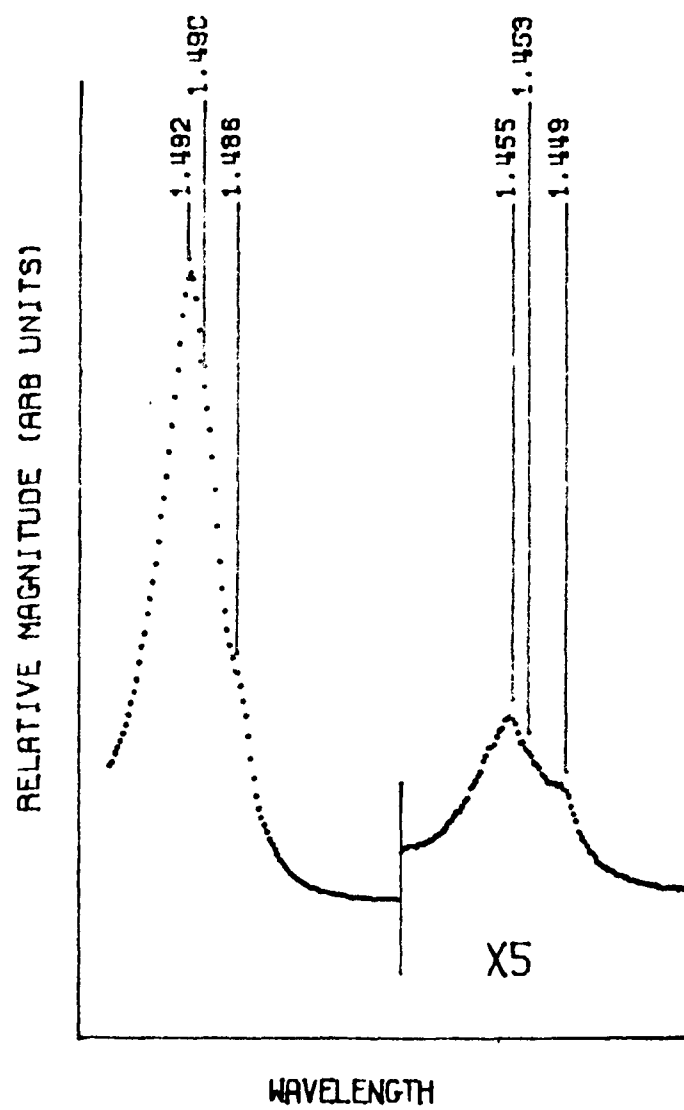
Fig. 16 Expanded View of Fig. 15. 120 keV/5E13 cm^{-2} Mg
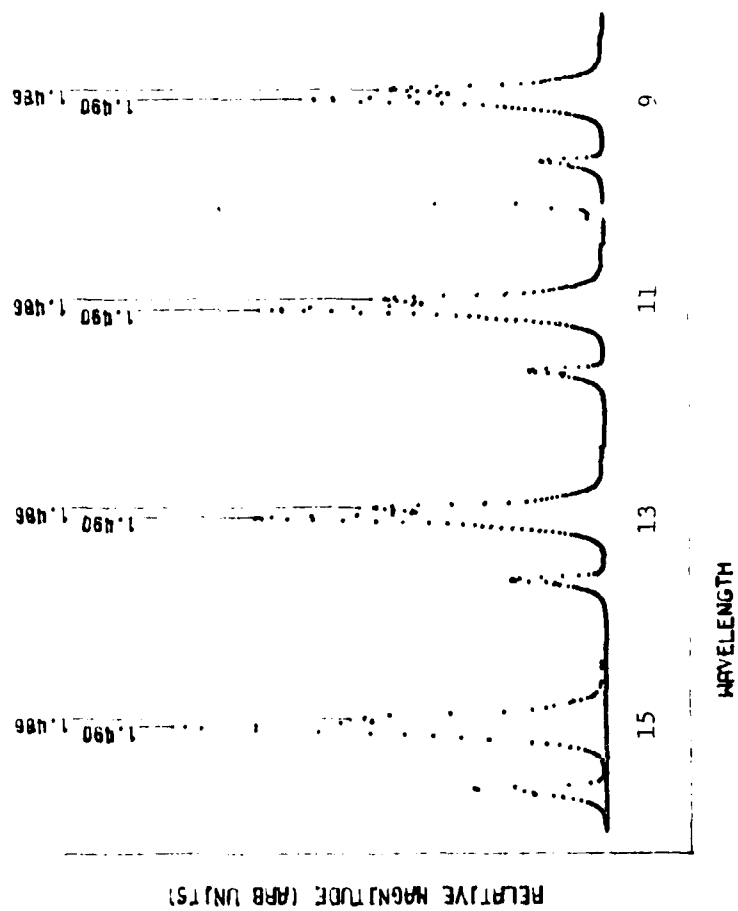Implanted GaAs

Fig. 17 Zn and Si Lines Taken with 15, 13, 11, and 9 keV Electron Beams at 5 microamp Beam Current
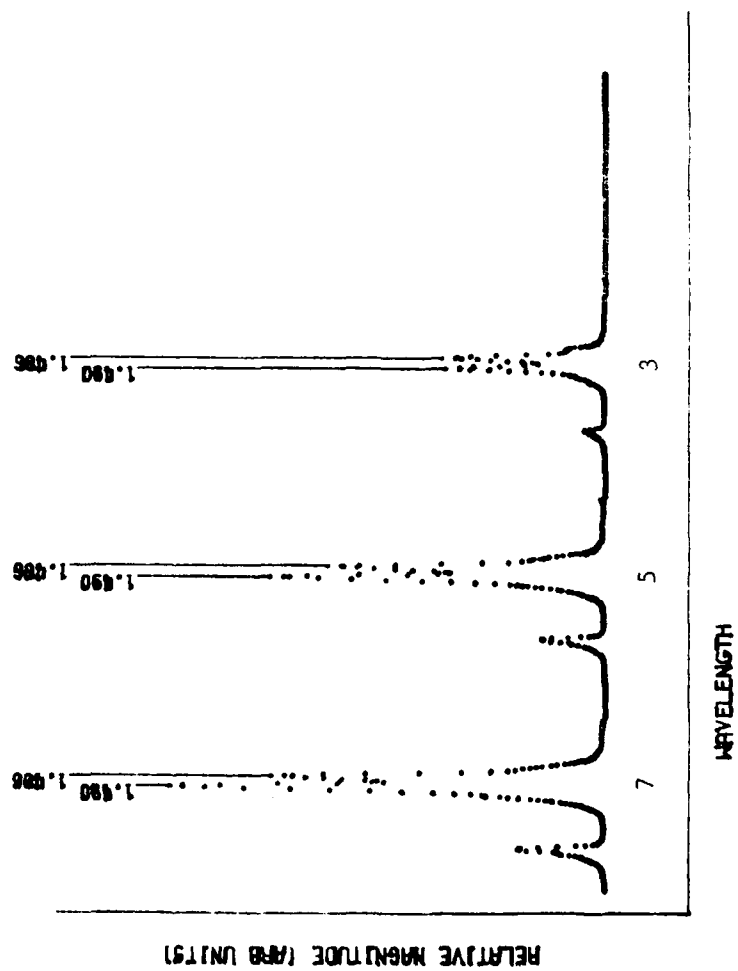
Fig. 18   Zn and Si Lines Taken with 7, 5, 3 keV Electron Beams at 5 microamp

75

They also indicate that this line might come from a free hole to neutral donor recombination.

These are only suggested assignments. It is felt that the free to bound line for Mg at 1.492 eV is definite. The Zn line at 1.490 eV, the Si line at 1.48 eV and their phonon replicas are also reasonably certain. The others are less so. For this study the only line of major importance is the Mg line. While the copper line is used for normalizing, it is not important to know what caused it as long as it is known that the source of this line is uniformly distributed over the depth of the epilayer.

Spectral Variation with Current Density

In this section it will be illustrated how the spectrum changes as the current density on the sample varies. The current density is specified in terms of the total current collected by the Faraday cup. This is the quantity that is measured. As the cross sectional area of the electron beam is held constant (by virtue of the cross section of the beam always being bigger than the aperture for the Faraday cup), constant total current implies constant current densities, assuming the beam has a uniform crosssection. Since a cross section of the beam suffers some nonuniformities, the following procedure was adopted to minimize its effect. The electron beam is first steered onto a Faraday cup into a position that maximizes the beam current into the cup. Then the beam is switched to the sample and the amount of luminescence at a particular line is maximized by moving the beam around on the sample. This procedure tends to place the same part of the beam on the sample that was measured in the cup and to locate the beam on the sample in the same place as was used for the previous measurement. Figure (19) is the

76

luminescence from a 90 keV Mg implant into epitaxial GaAs at a fluence of $1E13$ cm^{-2}. The spectra were taken with 5.0, 1.0 and 0.1 microamp beam currents and a 15 keV electron beam energy.

The first plot, figure (19-a), is of the spectrum taken with a 5 microamp beam current. Figure (19-b) expands the spectrum around the 1.492 and 1.455 eV lines. The Mg line at 1.492 eV is the major line in that spectrum. The line at 1.504 eV is missing in all three spectra. The peak at 1.455 eV is the major peak in the phonon replica structure. This supports the earlier identification of the 1.455 eV line as a phonon replica of the 1.492 line. As the beam current is decreased to 1.0 microamp, (figures (19-c, d)), the amplitude of the 1.492 line drops relative to the other lines. In fact, the Zn line is almost as large as the Mg line. Simultaneously, the 1.455 eV line drops relative to the 1.449 line. A new line at 1.453 eV appears that is 37 meV below the 1.490 eV line. This line is a phonon replica of the zinc line. It could not been seen before because the zinc line was relatively too small. The third spectrum is at 0.1 microamp. Now the Mg line is smaller than the Zn line. Similarly, the intensity of the 1.455 line has dropped below the 1.453 eV line. The lineshapes also appear to be more clearly resolved at the lower currents.

The reason for the dramatic change with current density is not at all clear. The trends were the same in all of the samples examined. A possible explanation is that the probability for recombination is higher for the deeper lying acceptors, that is, the probability for the free to bound transition involving Zn is more probable than the same transition with Mg. As the current density increases, the recombination path through
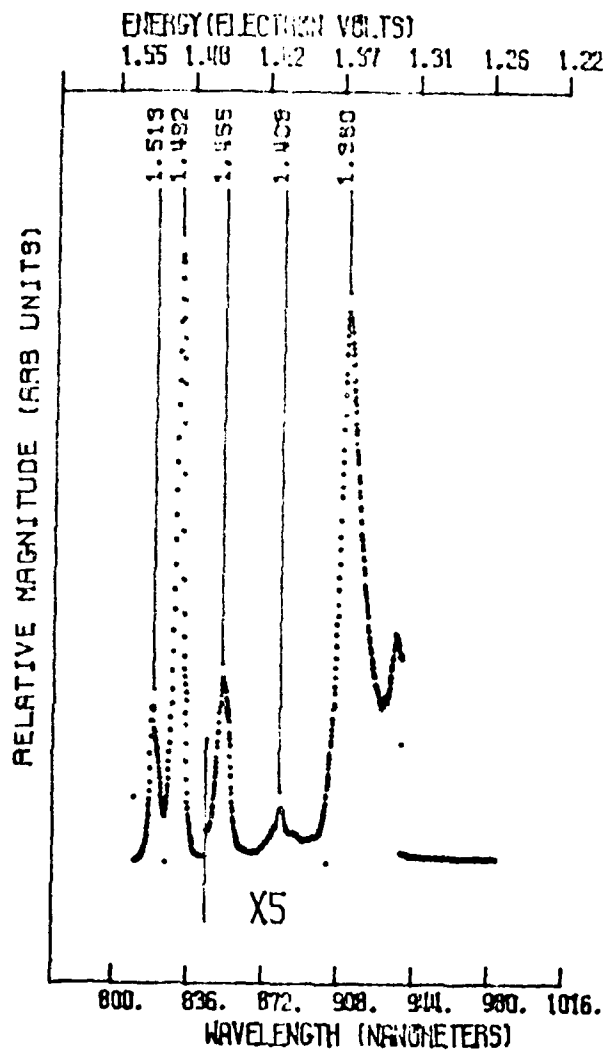
(a) Microamp beam current

Fig. 19 Luminescence from 90 keV Mg implant into GaAs at
a Fluence of 1E13 cm^{-2}, 15 keV Electron Beams at
5, 1, and 0.1 microamps

78

Fig. 19 (b)   Expanded 5 microamp spectrum

ENERGY (ELECTRON VOLTS)

1.55 1.48 1.42 1.37 1.31 1.26 1.22

1.513
1.492
1.455
1.408
1.360

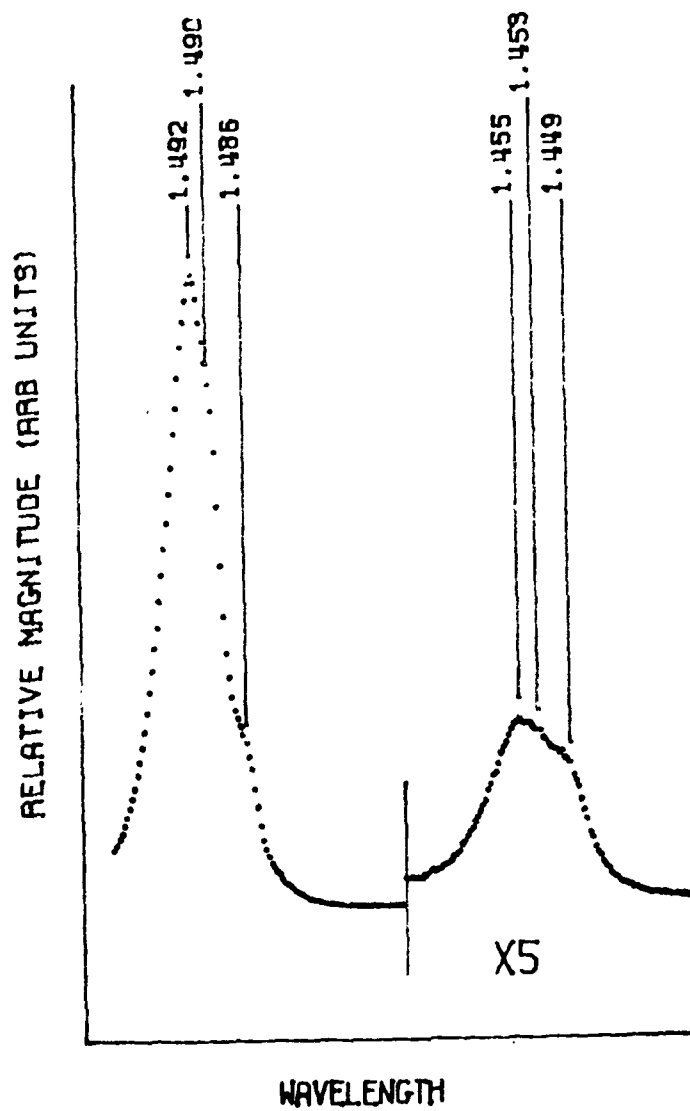RELATIVE MAGNITUDE (ARB UNITS)

X5

800. 896. 872. 908. 944. 980. 1016.
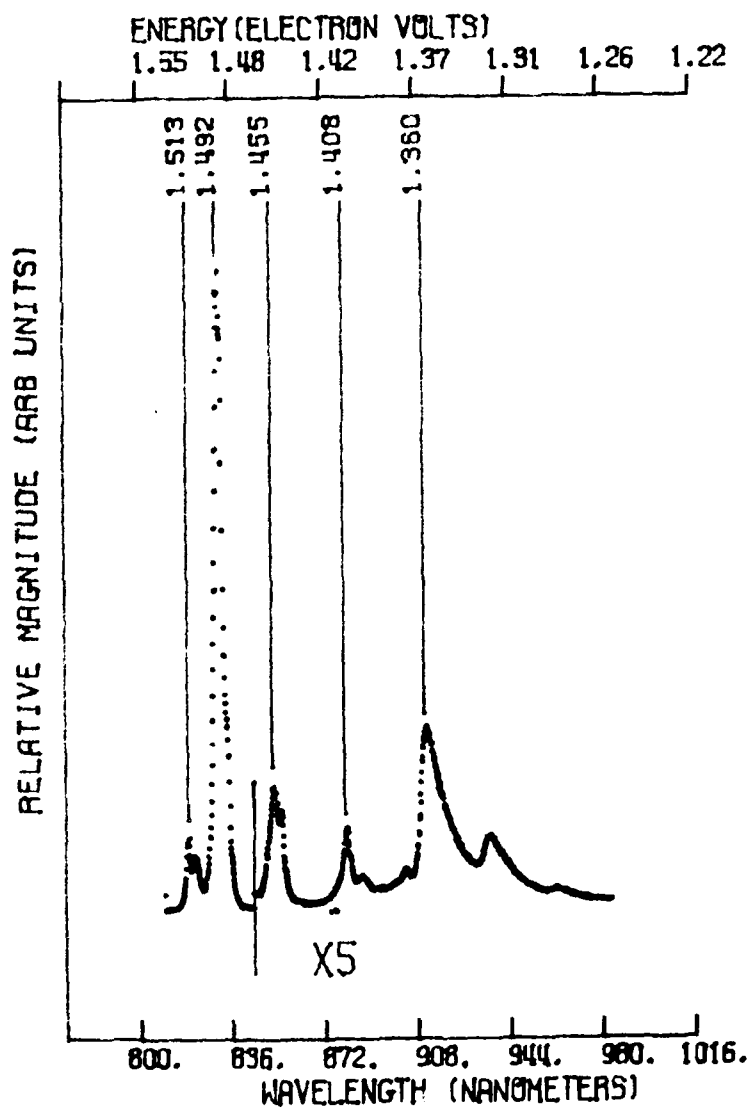
WAVELENGTH (NANOMETERS)
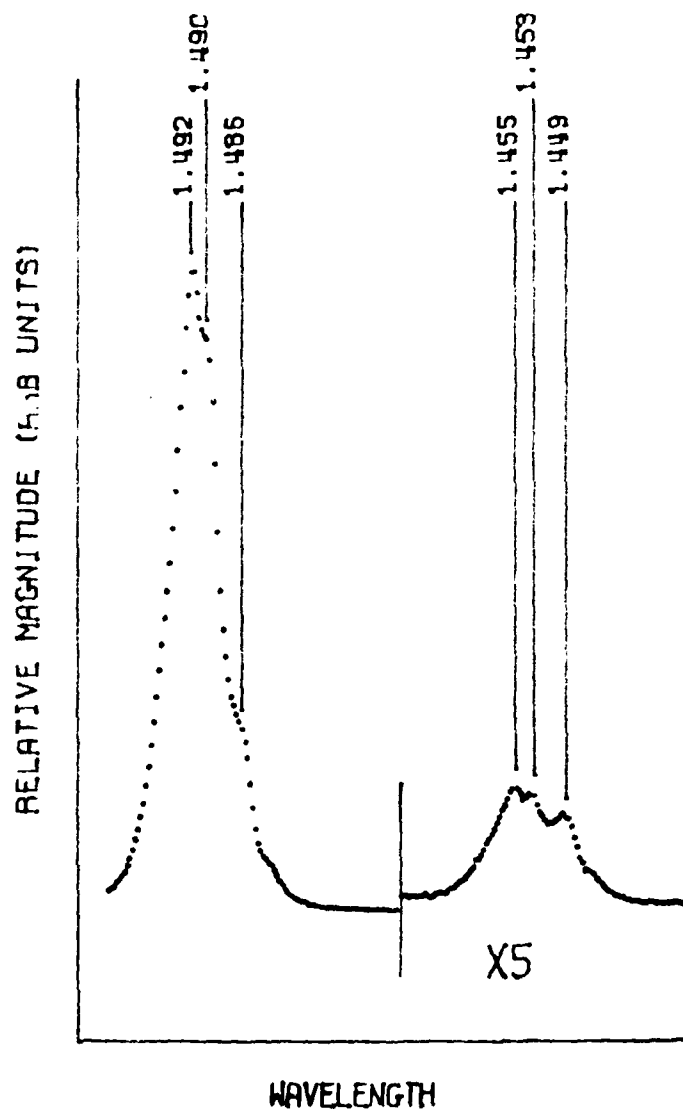
Fig. 19 (c) 1 microamp beam current

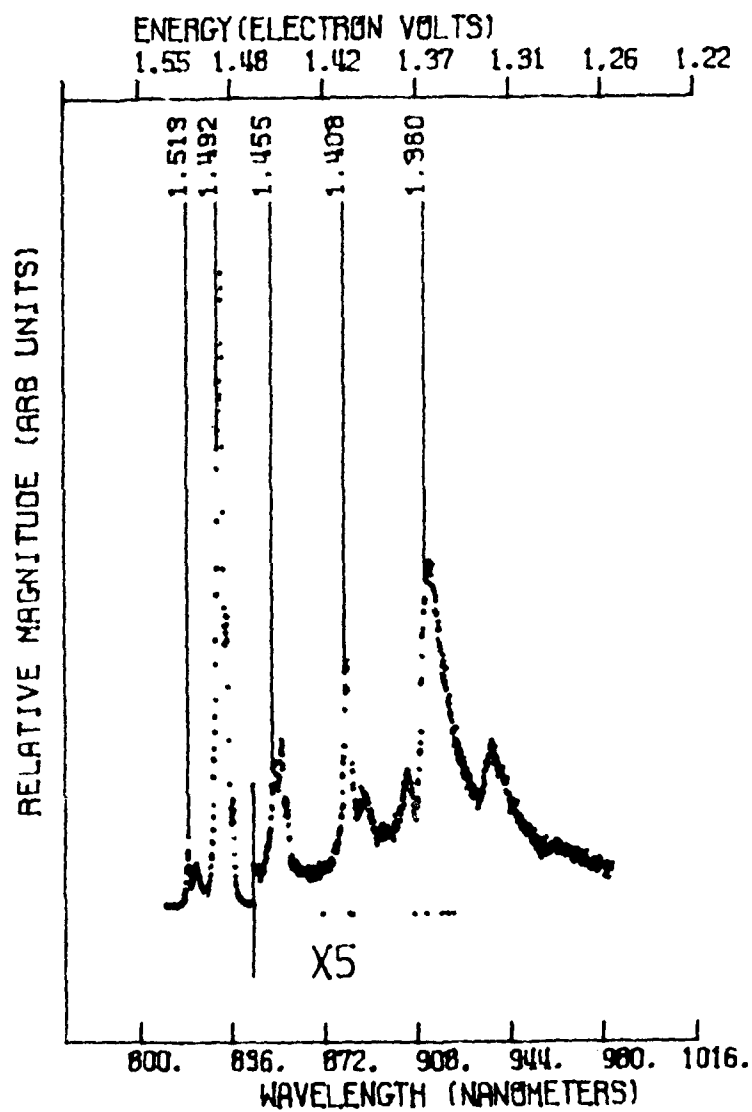Fig. 19 (d) Expanded spectrum for 1 microamp beam current

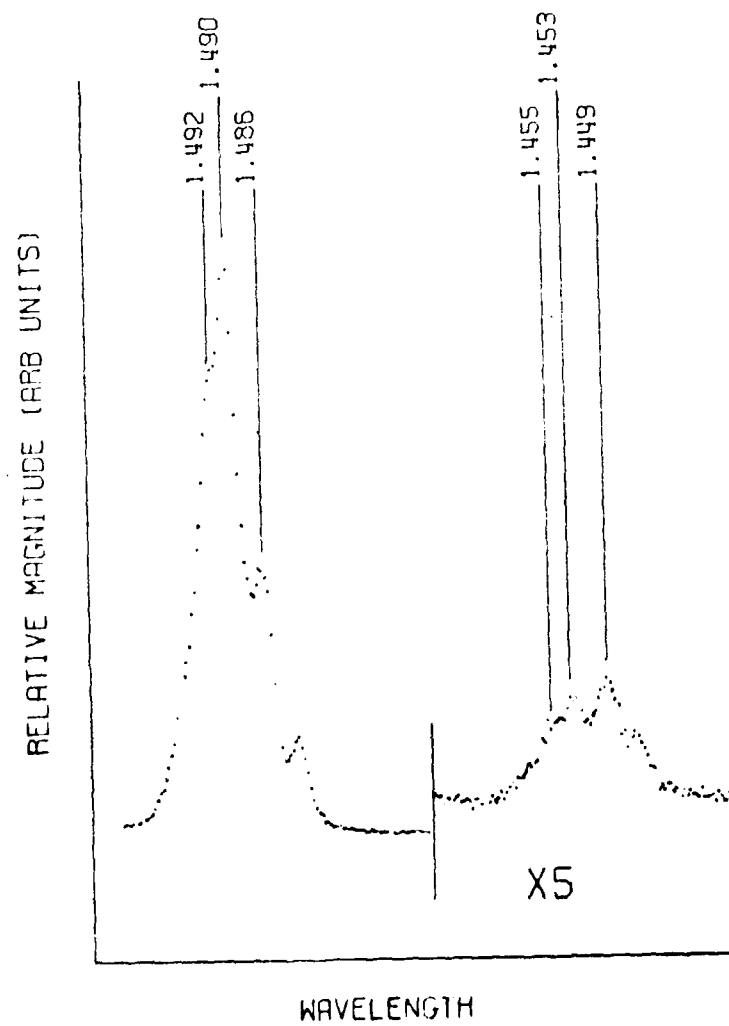Fig. 19 (e) Spectrum for a 0.1 microamp beam current

Fig. 19 (f) Expanded spectrum for 0.1 microamp beam current

Zn saturates before the Mg, since there are less Zn impurities than Mg.
At this point, the Mg line takes over and becomes the more important
line. According to Dumke's[93] theoretical approach for the recombina-
tion time, τ, of electrons with acceptor-bound holes at low temperatures,

$$\tau \propto E_A^3/P_A. \qquad (24)$$

E_A is the acceptor binding energy and P_A the concentration of bound
holes. Since E_A is larger for Zn than Mg, P_A must also be larger for Zn
by enough to make τ for Zn smaller than τ for Mg. What happens is that
the holes bound to the impurities seek out the higher impurity line in
the energy gap (Zn over Mg) as this is the state of lower energy for
holes. Thus, if the density of Zn impurities is large enough compared to
the Mg density, the Zn free to bound transition has a shorter lifetime
than the Mg transition due to the larger concentration of bound holes.
As the beam current increases there are more holes available to be bound.
Eventually the Zn recombination path is saturated as the number of bound
holes approaches the number of Zn impurities. As there are more Mg ions
than Zn ions available to bind the holes, P_A for Mg starts to increase
and the lifetime for Mg decreases to the point where Mg is the more
important line. A similar effect should hold for the Zn and Si lines.
As the current density goes down, the Si line intensity should increase
compared to the Zn line. Table V shows the results for the unimplanted/
unannealed sample. This sample was chosen so that the presence of the Mg
line does not affect the results. The data is taken at 10 keV. The Si
line is increasing faster than the Zn line as the current increases. The
change is more pronounced from 1.0 to 0.1 microamps since the larger Zn

84

1.0

1.1

1.25

2.8

3.2

3.6

4.0

2.5

2.2

2.0

1.8

1.4

1.6

MICROCOPY RESOLUTION TEST CHART
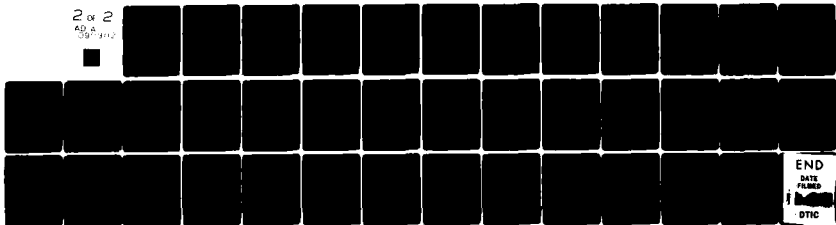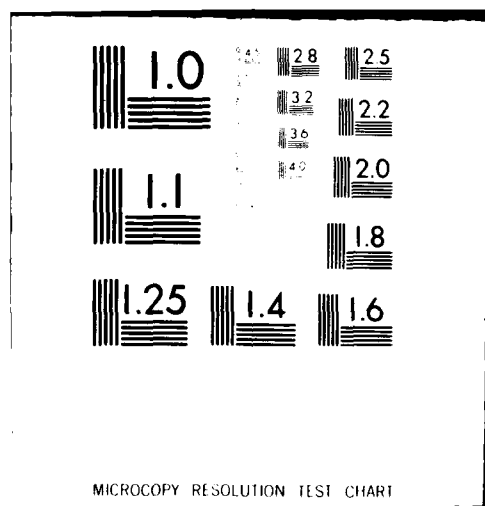
peak overshadows the Si peak at 5 microamps. The ratio is based on the

peak of the line as measured. The peaks do not have the effects of the

other lines subtracted out before the ratio is calculated. To do so

would make the changes more dramatic. Other samples show similar trends.

The spectrum shows in figure (19) shows a similar trend in the ratio from

1.0 to 0.1 microamp. The trend is reversed from 1.0 to 5.0 microamps.

This reversal is caused by the Si and Zn lines being swamped by the much

larger Mg line. The reason the ratios at 1.0 and 0.1 microamp follow the

proper trend is that the lines are better resolved at these beam currents,

hence the Mg line has less effect.

Table V

Ratio of Peak Intensity of Si to Zn Free-to-Bound Transition

Beam Current (microamp)	Unimplanted/ Unannealed Sample	90 keV/1E13 cm^{-2} Mg/GaAs Sample*
5.0	.26	.32
1.0	.29	.29
0.1	.58	.46

*Spectrum shown in figure (19).

Another point to be made is that the peaks are better resolved at

the lower current densities. This is attributed to less local heating of

the sample at the lower electron beam current densities. Also the abso-

lute intensities of all lines decrease as the current density drops

because there are less electroncs and holes available for recombination.

Kurbatov et al[104] also studied the influence of the excitation

level on GaAs luminescence. Their data was taken at 60 keV beam energy

with current densities from 0.6 to 20 amps/cm^2. This is four times the

maximum beam energy used here and about 1000 to 320,000 times the current density. Thus their results are not directly related to those reported here. Still, they observed new lines emerging as the beam current density increased. These lines tended to be associated with different types of transitions instead of the same type of transition through different impurities. For instance, at 10°K in n-type GaAs the line dominant at low current densities is a free-to-bound transition through an acceptor, while the dominant line at higher current densities appears to be an exciton bound to a donor. For the data in this report, the type of transition is a free electron to a hole bound on an acceptor; the different lines are associated with different acceptor impurities.

The reason that the variation with current density is important to profiling is that the profile information is contained in the variation of the Mg line with beam energy. The higher current densities are required in order to force the Mg line to be the major contributor to the 1.49 eV complex. If it is not, the profile information is further obscured by the adjacent lines. This results in fewer details of the profiles being resolved and reduces the confidence factor in the final result. While a larger current density produces a larger ratio of intensities of Mg to Zn lines, a smaller current density is easier to achieve experimentally. The reason for this is that at the lower beam energies the electron gun becomes space charge limited and the maximum gun current is reduced. With the present experimental arrangement 5 microamps at 2.5 keV is the best that could be done and only occasionally could this result be reached. Frequently 3 or 4 keV at 5 microamps is the best that could be done. The L(V) curves were determined at 5 microamps since this

86

seemed the best compromise between low energy response and high intensity Mg lines.

Luminescence versus Beam Voltage Curves

This section contains the primary results of the investigation. The goal of this research is to determine the feasibility of using cathodoluminescence as a depth probing tool. In this section the experimental results are described and compared with the theoretical results of the last chapter.

First, it is necessary to describe again how the data was taken and presented. As noted above, the beam current was kept at 5 microamps when the L(V) curves were to be determined using the Mg line. In order to cancel any variations from run to run, such as changes in the optics, changes in beam position, etc., the Mg line was normalized to the copper line. Since the calculation predicts the total number of photons per second to be observed, it is necessary to determine the integrated line intensity. If the lineshapes are Gaussian,

$$f(x) = c \frac{a}{\pi} e^{-ax^2} \tag{25}$$

then the integrated line intensity is

$$A = \int_{-\infty}^{\infty} c \frac{a}{\pi} e^{-ax^2} \, dX = c \tag{26}$$

If the lineshapes are of the form suggested by Eagles[94] for band to acceptor recombination,

$$f(x) = cx^{\frac{1}{2}} \exp^{-ax} \tag{27}$$

where c and a are constants, then the integrated line intensity is,

87

$$A = \int_0^\infty cx^{\frac{1}{2}} e^{-ax} dX = \frac{c\Gamma\frac{3}{2}}{a^{\frac{3}{2}}} = \frac{.886C}{a^{\frac{3}{2}}} \tag{28}$$

In either case, the peak of the line should be proportional to the integrated line intensity provided that the lineshape is either of the form of equations (25) or (27), that "a" is not a function of beam energy, and that the lines are clearly resolved. If "a" in equations (25) and (27) is a function of beam energy then the proper way to scale the peak line intensity to the integrated line intensity is

$$\text{AREA} \ \alpha \ \text{PEAK}/\sqrt{a} \tag{29}$$

for a Gaussian lineshape and

$$\text{AREA} \ \alpha \ \text{PEAK}/\frac{1}{a} \tag{30}$$

for Eagle's lineshape. It will be shortly demonstrated that both the peak intensities and the integrated lineshapes yield approximately the same L(V) curves.

L(V) curves determined from the peak and area of the lineshapes are compared in figures (20) and (21). The data points for the area curves are determined by resolving the Mg line from the 1.49 eV complex using the Dupont 310 lineshape simulator. The Mg integrated line intensity can then be read from the machine. The area of the copper line can also be determined using the simulator. A point on the L(V) curve is determined by dividing the area of the Mg line by the area of the copper line and scaling the result so that the peak of the L(V) curve is at 400.

The peak L(V) curve is calculated by determining "a" from the data and scaling the peak according to equation (29). The Gaussian scaling

88

factor was chosen since Gaussian curves were used to determine the area
L(V) curves. A data point on the L(V) curve is calculated by dividing the
Mg line by the Cu line and scaling to 400 as before. The results for the
60 keV implant at 5E13 cm^{-2} dose are presented in Table VI. The ratios
have been scaled to 400 for the largest ratio in each column. Table 6 is
plotted in figure (20). The curves are very close considering the arbi-
trariness with which the area of the Mg line is determined. Figure (21)
shows the results for the 90 keV implant at 5E13 cm^{-2}. While the results
are not as close as before, the same trends are evident. Thus, although
the integrated line intensity plot is necessary for quantitative agree-
ment, the peak intensity curves are at least qualitatively right. The
curves are not expected to agree exactly since the peak intensity curves
are determined from the peaks that include the effects of all the competing
lines in the 1.490 eV complex.

Table VI

Beam Energy (keV)	Peak Ratio	Area Ratio
4	400	400
5	292	295
7	267	273
9	201	212
11	181	195
13	174	177
15	130	138

Comparison of L(V) Curves for Peak vs Integrated Line-
shape Techniques Mg implanted into GaAs at 60 keV/5E13 cm^{-2}
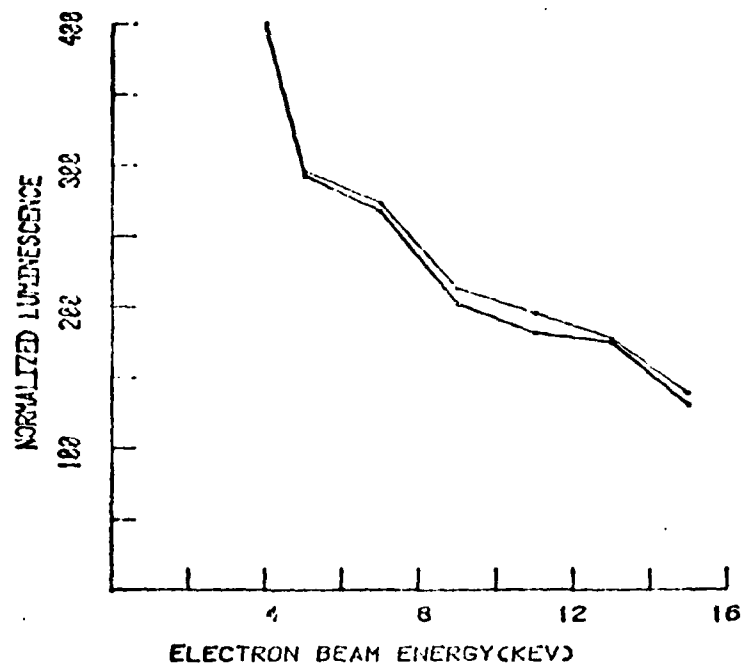
89

Fig. 20   Comparison of 60 keV/5E13 cm^{-2} Mg Implanted GaAs
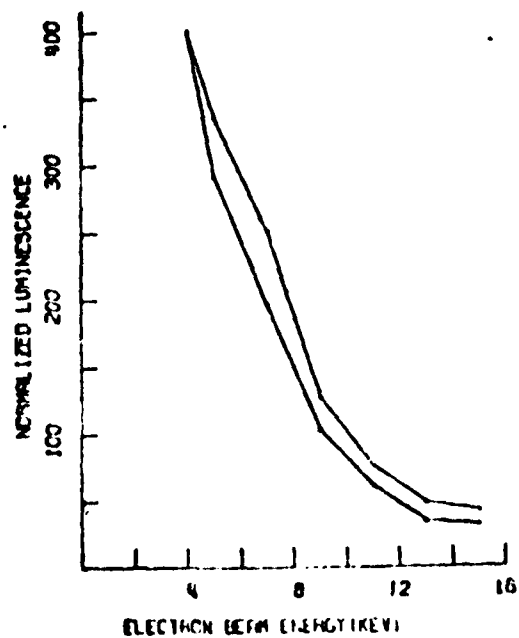

Fig. 21   Comparison of 90 keV/5E13 cm^{-2} Mg Implanted GaAs

Several peak intensity curves were obtained in order to get a qualitative feel for how the L(V) curves might vary. The reason for obtaining peak curves instead of the integrated line intensity curves is that they can be obtained much faster.

Figures (22) and (23) are peak L(V) curves for 5E13 and 1E14 cm^{-2} dose Mg implanted GaAs. The peak curves for 5E13 cm^{-2} show the sort of trends expected. The 120 keV sample yields more luminescence from higher energy beams than does the 60 or 90 keV sample. The 90 keV curve comes next and then the 60 keV curve. While the curves do not look exactly like the curves in figure (11-d) the same general trend is evident. All the curves show the type of fall off predicted in figure (11). There are two apparent problems with the 5E13 cm^{-2} curves. The first one is that the 90 keV curve falls off much faster than the 60 or 120 keV curves. The other is that the 60 keV curve has somewhat of a peak in the tail of the curve. These problems will be addressed in the next section.

The 1E14 cm^{-2} curves in figure (23) are very similar to the 5E13 cm^{-2} curves. The 120 keV curve shows more luminescence coming from the higher energy beams thus reflecting the fact that more implanted ions exist at deeper depths than are reached with the 90 keV beam. Again the same type of fall off is seen, although the 120 keV curve appears to turn up slightly at the end.

Earlier, it was shown that the higher current densities enhance the Mg free-to-bound line. By the same token, lower current densities favor the Zn line. Figure (24) shows a comparison of the L(V) curves determined from the peak of the Mg line at 5 microamps with the L(V) curve from the peak of the Zn line at 0.1 microamps. The Mg line clearly shows
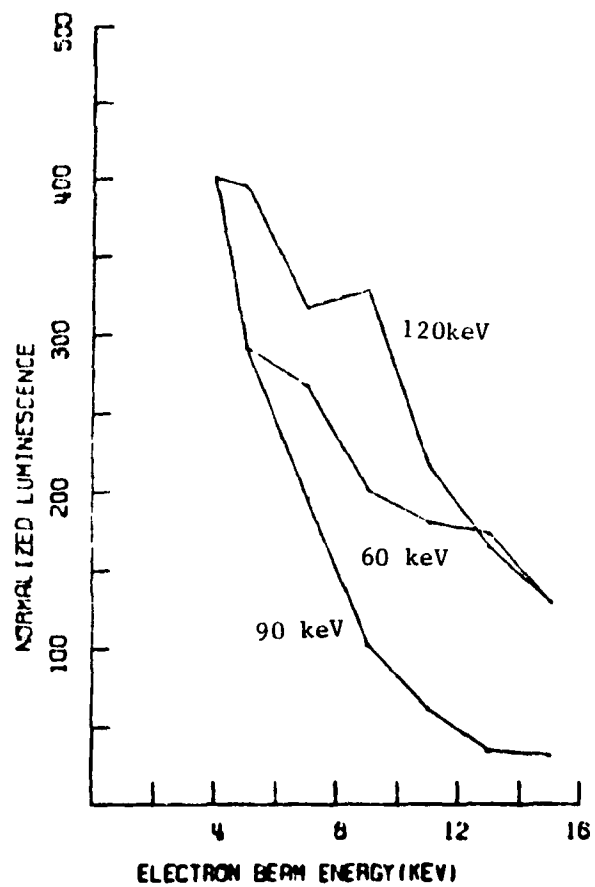
91

Fig. 22 Peak L(V) Curves 5E13 cm^{-2}/60, 90, 120 keV Mg Implanted GaAs

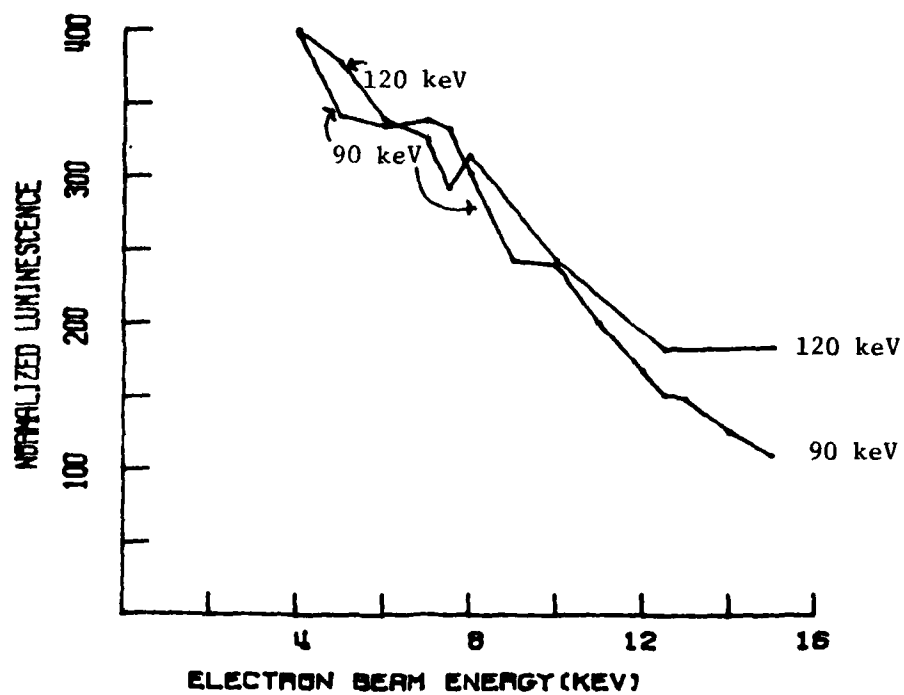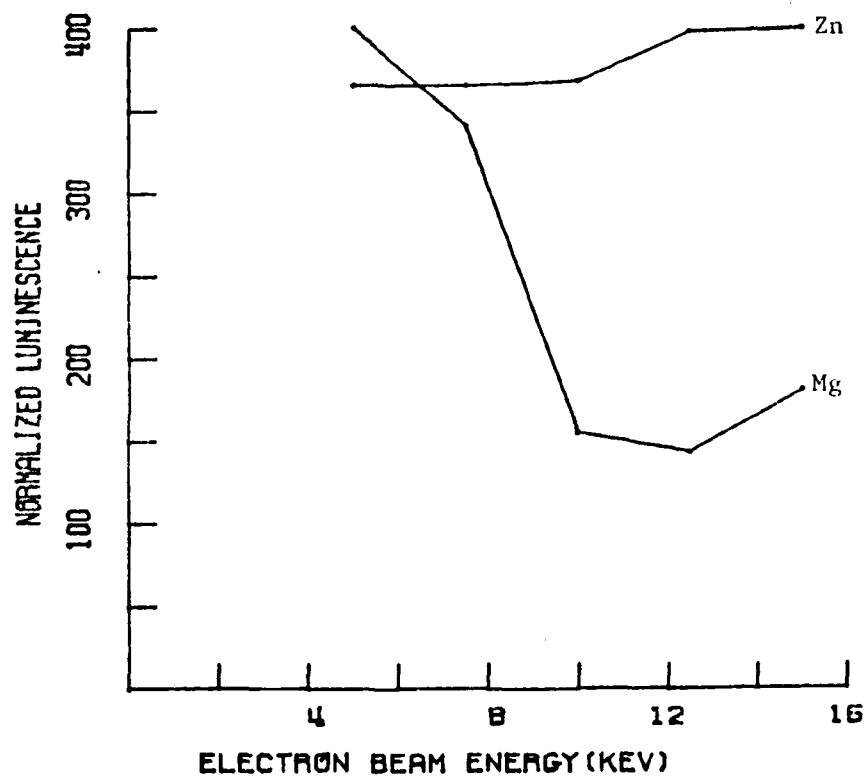Fig. 23 Peak L(V) Curves 1E14 cm^{-2}/90, 120 keV Mg Implanted GaAs

93

Fig. 24   Peak L(V) Curves 1 14 cm^{-2}/120 keV Mg Implanted GaAs.
Mg Line at 5 microamps Beam Current and Zn Line at
0.1 microamps.

the effect of the implant, while the Zn line is essentially flat. This

behavior would suggest that the Zn is uniform with depth, as the ratio of

the intensities of the lines from two uniformly doped impurities should

be a constant. Since Zn was present in the epilayer before implantation,

this seems like a valid result.

In figure (25) the computer simulation is presented for two uniform

implants with a diffusion length of .21 microns, a surface recombination

velocity of 1.65×10^6 cm/sec and absorption coefficients for Zn and Cu

of 70 and 1.5 cm^{-1} respectively. The results are reasonably close.

While the data points bend slightly up for the Zn line, the simulation is

flat. The increase may reflect a slight increase in the Zn density with

depth (less than 9% change), the uncertainty in the data points, or a

superlinear variation of cathodoluminescence intensity with net carrier

generation rate[19]. In any case, there is a clear distinction between

the appearance of the Zn line and the Mg line both in theory and experiment.

Figure (26) presents the three L(V) curves considered the most

likely to give quantitative agreement with theory. These were the last

ones taken after most of the experimental problems had been worked out.

Many of the same observations made for the peak L(V) curves apply here

since the peak and integrated lineshape curves agree quite well. The

peak in the tail of the 60 keV curve as well as the rapid fall off of the

90 keV curve will be addressed in the next section where the model and

the data will be put together to see how well they agree.

Reliability of Results

Depth profiles were made by Y. K. Yeo of the U.S.A.F. Avionics

Laboratory on the 5E13 cm^{-2}/90 and 120 keV implants. The depth profiles
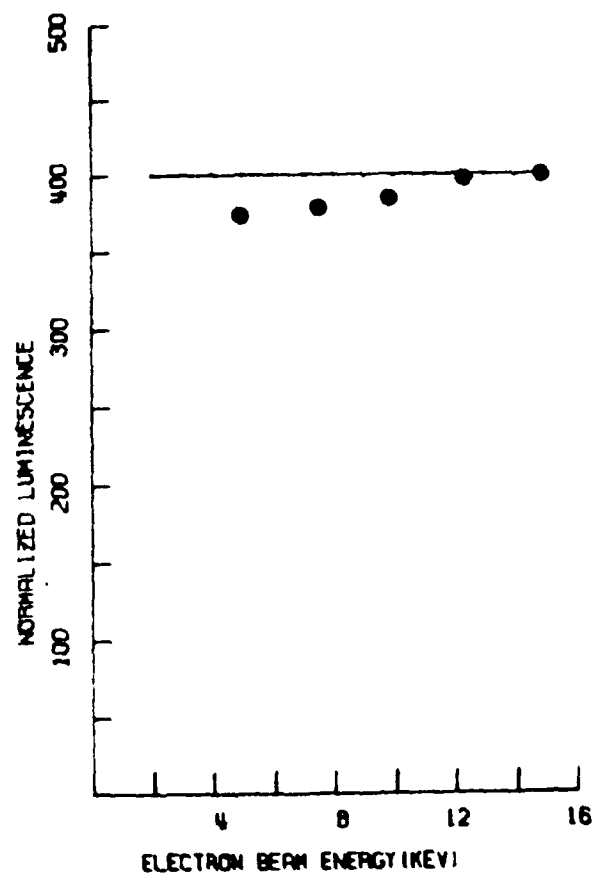
95

Fig. 25   Comparison of Calculated and Experimental L(V) Curves
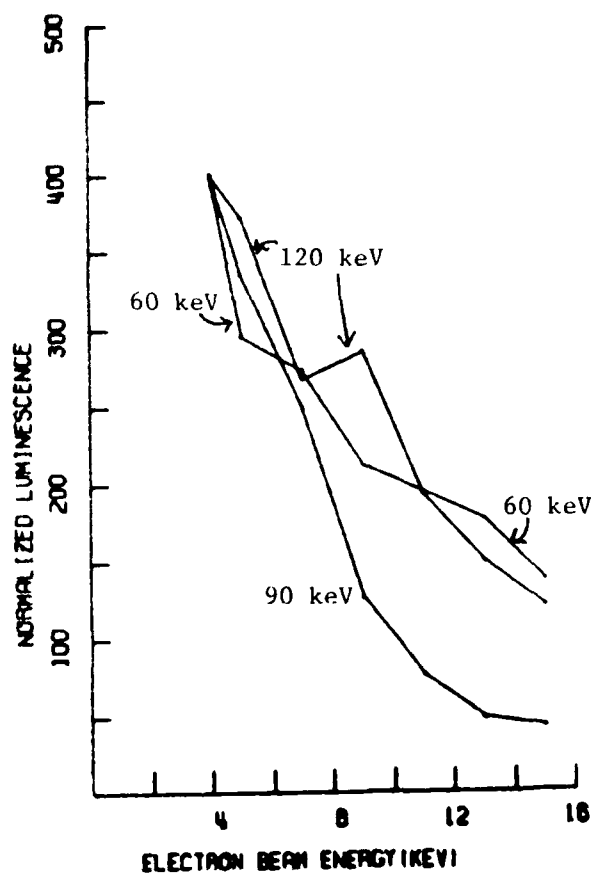for Two Uniform Impurities. Dots are experimental
points.

Fig. 26   Integrated Lineshape L(V) Curves for
60, 90, 120 keV Mg Implanted GaAs at
$5E13$ cm^{-2} Fluence

97

showed a considerable scatter in the data points, although they did vaguely resemble profiles determined by him earlier for other Mg implanted samples. There was a discoloration left on the samples after the L(V) curves had been obtained. In fact, as the GaAs was etched away from one sample, the discoloration actually seemed to get bigger. It had been supposed that this was a thin film of carbon resulting from the interaction of the electron beam and the hydrocarbons from possible backdiffusion of the diffusion pump oil or the aquadag that covered the copper shield that holds the samples in place. Further inquiry then turned up the fact that the etch would not dissolve carbon. A surface height measurement was made with a Dektak stylus which confirmed that a 2 to 5 micron layer had built up on the surface. As the sample was etched, the GaAs not protected by the film was etched away. This leads to the appearance of profiling, but does not accurately reflect the impurity profile. This explains the scatter in the data points as different parts of the surface are etched at different times and rates. It also explains the apparent increase in the spot size because of the shadowing effect of the film protective layer as the GaAs is etched away around it.

This brings up the question of how the L(V) curves are affected by the film layer. First, a carbon layer does not noticeably attenuate the incident electrons[95]. What it does to the emerging luminescence is another question. Fortunately, since the L(V) curve is determined by dividing the Mg by the Cu line, the only assumption needed to ignore the absorption effect of the carbon is that the absorption coefficients for luminescence from the Mg and Cu impurities have the same functional dependence with film thickness. If they do, then taking the ratio of two

lines cancels out any effects of absorption from the film. Nagy et al[96] show the transmittance of a carbon film in the 8000 to 10,000 $\overset{o}{A}$ range as smoothly varying from 50 to 60%. It seems unlikely that the variation of the absorption coefficients with film thickness will be significantly different for Mg and Cu. Therefore, the L(V) curves are assumed unaffected by the possible existence of a carbon film.

Figure (27) shows the calculated and experimental L(V) curves for the 120 keV/5E13 cm^{-2} sample. All things considered the agreement is remarkable. The values used in the calculation are:

$$L_n = 0.21 \text{ microns}$$
$$ALPHA_{Mg} = 70 \text{ cm}^{-1}$$
$$ALPHA_{Cu} = 1.5 \text{ cm}^{-1}$$
$$s = 1.65 \times 10^6 \text{ cm/sec}$$

where L_n is the ambipolar diffusion length, ALPHA is the absorption coefficient and s is the surface recombination velocity.

The question arises as to whether these are reasonable values to use. Values at 10°K are hard to find. The diffusion length can be calculated from

$$L = \frac{kT}{e} \mu\tau \tag{31}$$

where k is Boltzmann's constant, T is temperature, e the electronic charge, and μ the mobility. Bolger[98] et al measured electron mobilities down to 4.2°K. At 10°K they found mobilities ranging from 1×10^4 to 4×10^4 cm^2/v sec for donor impurity concentrations from 4.9×10^{14} to 3.0×10^{15} cm^{-3}. Radiative recombination times for impurities to the valence or conduction band can be estimated from Dumke's theoretical result. Assuming the number of acceptors to be 3×10^{17} cm^{-3} which is
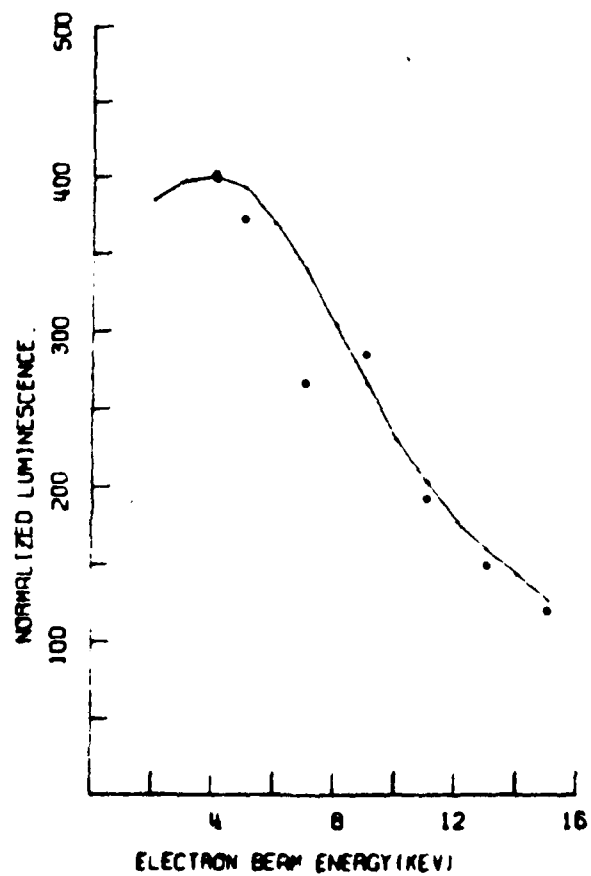
99

Fig. 27 Comparison of Calculated and Experimental L(V) Curves for 120 keV/5E13 cm^{-2} Mg Implanted GaAs. Dots are experimental points.

consistent with Yeo's measured result and a 5E13 cm^{-2} dose spread over

1.67 microns, the radiative lifetime at 10°K is 6.9 x 10^{-9} seconds.

Since nonradiative and other radiative channels shorten this figure it

has to be considered an upper limit. Using both upper limits for τ and

mobility and calculating the diffusion length from equation (31) leads to

the conclusion that the maximum diffusion length should be 0.28 microns.

This is not far from the 0.21 microns used in the computer fit. Since

0.28 microns is considered an upper limit the 0.21 micron figures seems

very reasonable.

The absorption coefficients in high resistivity GaAs were measured

by Sturge[107] from 10° to 294°K. From 0.6 to 1.4 eV the absorption

coefficient is small, staying under 4 cm^{-1}. As the band gap of GaAs is

approached the absorption coefficient rises rapidly to a value around 1 x

10^4 cm^{-1}. The absorption coefficient at 10°K around 1.49 eV is between 60

and 80 cm^{-1}. These values are consistent with the values measured by

Redfield and Afromowitz[100] for p type GaAs at 5°K. Thus the values

used in the computer fit for the absorption coefficients are supported by

other reported values. In addition the results are not particularly

sensitive to changes in the copper absorption coefficient. It can shift

by an order of magnitude either way and not significantly change the

results.

The surface recombination velocity falls right on the curve given by

Jastrzebski et al[101] for similarly doped samples. Their value for a

mid 10^{17} cm^{-3} doped sample is about 1.8 x 10^6 cm/sec. This result is for

room temperature but Vilms and Spicer observed that the surface recombina-

tion velocity did not change much over the 80° to 300°K range. Assuming

101

that the surface recombination velocity does not change with temperature then this value, too, is considered about right.

The final conclusion concerning the values chosen for the computer fit is that they are reasonable based on other workers results and theoretical calculations. The two other 5E13 cm^{-2} dose curves show similar results.

The 90 keV curve is fitted using the same diffusion length, coefficients and surface recombination velocity as the 120 keV sample. The results are shown in figure (28). The fit is not nearly as good as before. The fit can be improved by going to a much shorter diffusion length and higher surface recombination velocity. A shorter diffusion length can be supported in the literature; a higher surface recombination velocity is, however, much harder to justify. A good computer fit to the experimental data could not be obtained since below a diffusion length of about 0.1 micron the simulation failed to converge.

The 60 keV L(V) curve is fitted assuming a slightly different impurity profile. This profile consists of two LSS profiles added together. The first is the LSS profile predicted by LSS theory for a 60 keV implant. The second profile has the same shape as the first but is centered around a 0.5 micron depth instead of the 0.0615 micron depth predicted by LSS and has an amplitude equal to 0.55 times the first peak. With this change and assuming the same parameters as the 120 keV implant gives the fit shown in figure (29). Figure (30) shows the profile used in figure (29). The physical nature of the second hump is unknown but could be caused by a component of the implant beam penetrating down a crystalline axis (channeling).

The experience with the 60 keV implant brings up a question as to the resolution possibilities of this technique as regards double peaks. In order to address this question a study was undertaken to determine the range over which two peaks make measurable changes in the L(V) curves for a double profile as is found in the 60 keV sample. The details are considered in Appendix B. The results indicate that with the parameters used here, peaks separated from 0.25 to slightly less than 10. microns could be distinguished.

An important point to note in figures (27), (28), and (29) is that data points below 4 keV play an important part in distinguishing one profile from another. It is anticipated that a experimental setup capable of yielding data points down to election beam energies of 2 keV is very important in identifying different implant profiles.

Summary of Important Results

This section is a summary of the most important results of this study. The first result obtained is in the depth-dose curves for electron beam penetration into GaAs. These curves are important for both cathodoluminescent and microprobe work as they help to quantify models of both processes.

The next result is the spectra from various samples of Mg implanted epitaxial GaAs. These spectra had not been studied before. Several lines of the spectra between 1.3 and 1.5 eV were identified. The effect on the spectra of changing the current density was studied. In this section, it was shown how dramatically the intensity of various lines change with current density. A proposed explanation of this variation was given for the free-to-bound transitions.

103
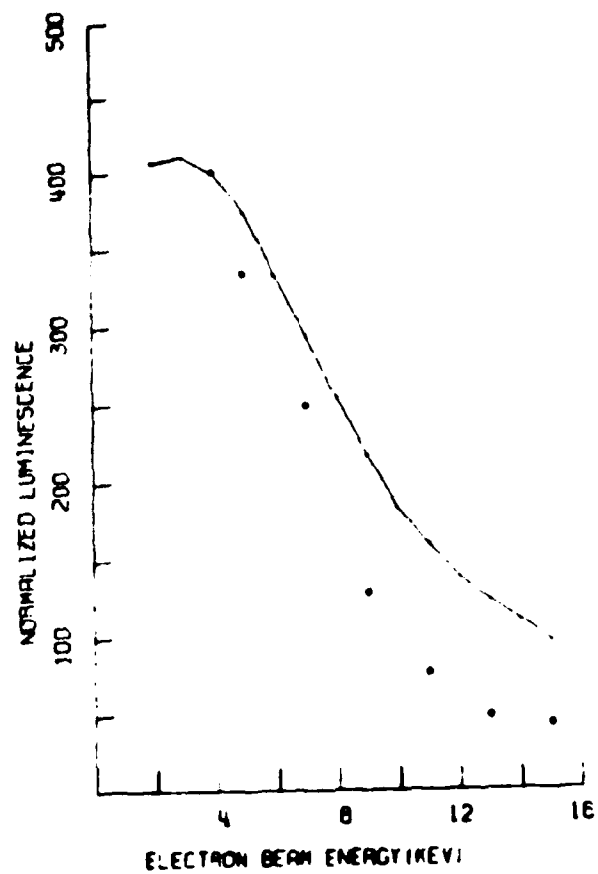
Fig. 28 Comparison of Calculated and Experimental
L(V) Curves for 90 keV/5E13 cm^{-2} Mg Implanted
GaAs. Dots are experimental points.

104
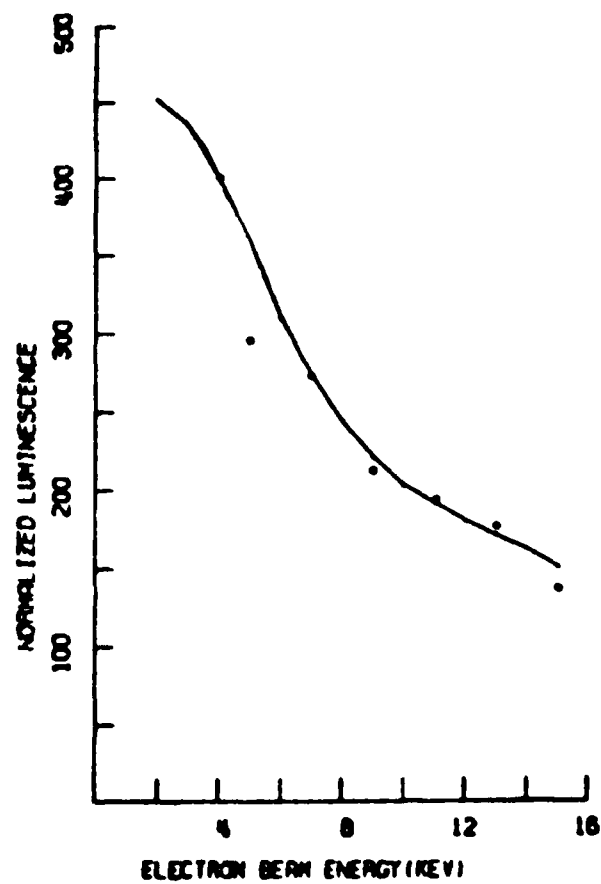
Fig. 29 Comparison of Calculated and Experimental
L(V) Curves for 60 keV/5E13 cm^{-2} Mg Implanted
GaAs. Dots are experimental points.
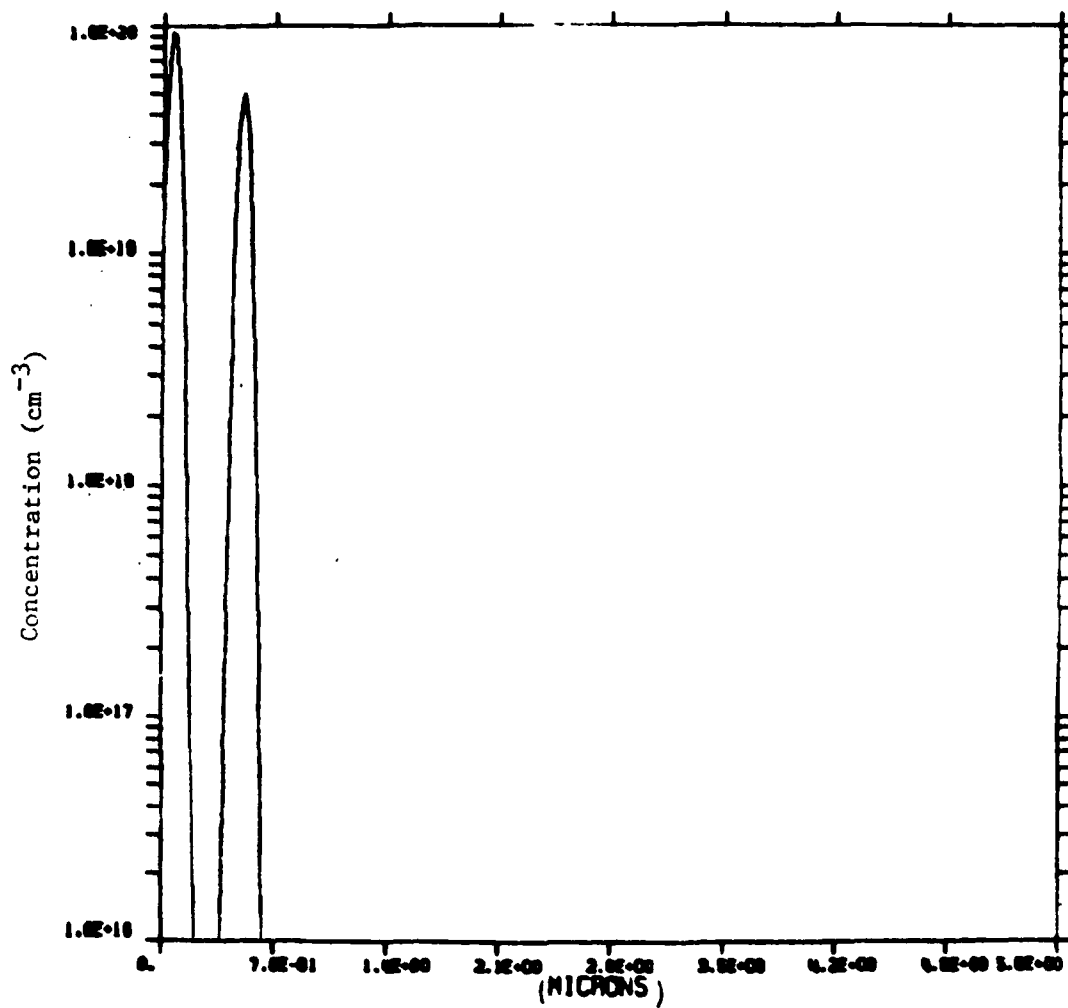
Fig. 30 LSS Profile used for fig (29).

In the section on the luminescence versus beam voltage curves, it is shown how the integrated lineshape is proportional to the peak of the line for a Gaussian lineshape and the lineshape proposed by Eagles. Next, the theoretical and experimental curves were compared. Good agreement is found for these curves providing the proper parameters are chosen. The reliability of these choices is discussed and it is concluded that the parameters chosen are reasonable.

V. Conclusions and Recommendations

The purpose of this research is to "establish a quantitative basis for cathodoluminescence" in GaAs. To that end a computer model was developed of the process and data was taken in an effort to validate the model. As demonstrated in the last section of the previous chapter the agreement is very good. The conclusion is that a basis has been established for quantitative cathodoluminescence.

There are several other conclusions that can be drawn from the results of this study. The first is that depth-resolved cathodoluminescence can be used not only to identify what impurities are present in GaAs, but also where the concentration is highest. This was demonstrated for the Si impurity where it was shown that Si diffused into the epitaxial layer from the surface and not from the substrate.

Next, a relation between the diffusion length, recombination time, diffusion constant and surface recombination velocity was found. This results in a great reduction in the number of combinations of parameters that need be examined in order to fit experimental and theoretical curves. It also means that without some independent determination of one of the parameters, they cannot be absolutely determined from cathodoluminescence data.

The study of the spectra from several samples failed to turn up any donor-acceptor pair transition. This supports the contention of Bishop et al[106] who interpreted Yu and Park's data as an implant depth gradient effect and not a donor-acceptor pair transition.

In the section of the effect of changing the current density on the spectra, the dramatic changes in the spectra that can take place were

108

shown. Unless some care is taken to make sure that the current density is held constant, conclusions drawn from spectral changes must be questioned. Setting the total beam current to a constant value is not as important as maintaining a constant current density at the surface.

By implication, the diffusion lengths for annealed Mg implanted GaAs at 10°K must be very short. The best fit for the luminescence data was at a .21 micron diffusion length, much shorter than that suggested in reference 106. This short diffusion length means the excited carriers recombine shortly after excitation. The volume of GaAs in which radiative recombination occurs is thus not much greater than the volume excited by the electron beam. Thus, the spatial resolution of cathodo-luminescence is about that of the electron energy loss curves. Profiling should thus be possible for any impurity implant profile whose dimensions are on the order of, or more than those spanned by the energy loss curves.

The recommendations generally concern improvements in the experimental facilities and theoretical model. They are:

(1) Improve the electron gun design so that a uniform beam can be obtained from 1 to 15 keV.

(2) Improve the gun design so that more than 5 microamps of beam current can be provided at 1 keV when the beam is defocused to cover the entire entrance aperture to the Faraday cup.

(3) Include the effects of the depth dependence of the diffusion length in the calculation.

(4) Work on solving the inverse problem of deducing the profile, given the L(V) curve.

(5) Study more samples under different conditions to establish a

109

larger data base on which to draw conclusions.

Of these recommendations, numbers (4) and (5) are the most important.

Bibliography

1. B. J. Pierce, Unpublished dissertation, Wright-Patterson Air Force
   Base, Ohio: Air Force Institute of Technology (Sept 1974).

2. C. R. Daniels, Unpublished thesis, Wright-Patterson Air Force Base,
   Ohio: Air Force Institute of Technology (March 1975).

3. D. L. Boulet, Unpublished thesis, Wright-Patterson Air Force Base,
   Ohio: Air Force Institute of Technology (Dec 1975).

4. G. V. Boyd III, Unpublished thesis, Wright-Patterson Air Force Base,
   Ohio: Air Force Institute of Technology (June 1976).

5. J. Dumoulin, Unpublished thesis, Wright-Patterson Air Force Base,
   Ohio: Air Force Institute of Technology (Dec 1976).

6. M. Walter, Unpublished thesis, Wright-Patterson Air Force Base,
   Ohio: Air Force Institute of Technology (Dec 1977).

7. D. F. Kyser and D. B. Wittry in: The Electron Microprobe, Ed. by
   T. D. McKinley, D. F. J. Heinrich, D. B. Wittry: John Wiley and
   Sons, 691 (1966).

8. D. A. Shaw and P. R. Thornton, J. of Materials Science $\underline{3}$, 507 (1968).

9. D. B. Wittry and D. F. Kyser, J. of Appl. Phys. $\underline{38}$, 375 (1967).

10. W. H. Weisenberger, H. Gray, G. K. Hubler, K. L. Dunning, J. Comas,
    12th Annual Reliability Physics Proceedings, (1974).

11. W. H. Hackett, Jr., J. of Appl. Phys. $\underline{43}$, 1649 (1972).

12. D. R. Heath and C. E. E. Stewart, Solid State Electronics $\underline{15}$, 21 (1972).

13. C. B. Norris, E. E. Barnes, and W. Beezhold, J. Appl. Phys. $\underline{44}$, 3209
    (1973).

14. B. J. Pierce and R. L. Hengehold, J. Appl. Phys. $\underline{47}$, 644 (1976).

15. J. M. Woodcock and D. J. Clark in: Gallium Arsenide and Related
    Compounds, 1974: The Institute of Physics, 47 Belgrave Square,
    London, England, 331 (1975).

16. D. A. Cusano, Solid State Comm. $\underline{2}$, 353 (1964).

17. J. F. Gibbons, Proceedings of the IEEE, $\underline{56}$, 295 (1968).

18. Gy. Gergely, Acta Phys. Hung., $\underline{12}$, 221 (1960).

19. T. S. Rao-Sahib and D. B. Wittry, J. of Appl. Phys. 40, 3745 (1969).

20. Private communication from Y. S. Park following reference (17).

21. U. Fano, Phys. Rev., 58, 544 (1940).

22. W. van Roosbroech, J. of Appl. Phys. 26, 380 (1955).

23. D. B. Brown and R. E. Ogilivie, J. of Appl. Phys. 37, 4429 (1966).

24. D. B. Brown, D. B. Wittry, and D. F. Kyser, J. of Appl. Phys. 40, 1627 (1969).

25. M. Green, Proc. Phys. Soc. (London) 82, 204 (1963).

26. H. E. Bishop, in: X-Ray Optics and Microanalysis, R. Castaing, et al: Eds (Hermann and Cie., Paris, 1966) p. 112.

27. R. Shimizu, T. Ikuta, and K. Murata, J. of Appl. Phys. 43, 4233 (1972).

28. G. Wentzel, Z. Phys. 46, 590 (1927).

29. N. F. Mott and H. S. W. Massey, The Theory of Atomic Collisons (Oxford: Clarendon, 1965).

30. T. E. Everhart, J. of Appl. Phys., 31, 1483 (1960).

31. W. Bothe, Z. Phys. 5, 63 (1921).

32. W. Bothe, Hand. d. Phys. 22/2, 1 (1933).

33. G. Wentzel, Ann. Phys. Lpz. 69, 335 (1922).

34. G. Moliere, Z. Naturf. 2a, 133 (1947).

35. F. Lenz, A. Naturf. 9a, 185 (1954).

36. G. H. Smith and R. E. Burge, Proc. Phys. Soc., 81, 612 (1963).

37. V. E. Cosslett and R. N. Thomas, Brit. J. Appl. Phys. 15, 235 (1964).

38. W. Bothe, Z. Phys. 54, 16J (1929).

39. H. A. Bethe, M. E. Rose, L. P. Smith, Proc. Amer. Phil. Soc. 78, 573 (1938).

40. S. Goudsmit and J. L. Saunderson, Phys. Rev. 57, 24 (1940).

41. H. W. Lewis, Phys. Rev. 78, 526 (1950).

42. L. V. Spencer, Phys. Rev. $\underline{98}$, 1597 (1955).

43. L. V. Spencer, "Nat. Bur. Stand. Monograph 1" (Washington: National Bureau of Standards, 1959).

44. H. Meister, Z. Naturf. $\underline{13a}$, 809 (1958).

45. V. E. Cosslett and R. N. Thomas, Brit. J. Appl. Phys. $\underline{15}$, 883 (1964).

46. G. Moliere, Z. Naturf. $\underline{3a}$, 78 (1948).

47. F. Lenz, Proc. Phys. Soc. $\underline{76}$, 714 (1960).

48. D. B. Brown and R. W. Ogilivie, J. Appl. Phys. $\underline{37}$, 4429 (1966).

49. D. B. Brown, D. B. Wittry and D. F. Kyser, J. Appl. Phys. $\underline{40}$, 1627 (1969).

50. M. J. Berger in: Methods in Computational Physics, ed. by B. Alder, S. Fernbach and M. Rotaenberg, Academic Press 135 (1963).

51. M. Green, Proc. Phys. Soc. $\underline{82}$, 204 (1963).

52. H. E. Bishop, Brit. J. Appl. Phys. $\underline{18}$, 703 (1967).

53. R. Shimizu, T. Ikuta, and K. Murata, J. Appl. Phys. $\underline{43}$, 4233 (1972).

54. R. Shimizu, Y. Kataoka, T. Ikuta, T. Koshikawa and H. Hashimoto, J. Phys. D: Appl. Phys. $\underline{9}$, 101 (1976).

55. A. J. Green and R. C. G. Leckey, J. Phys. D: Appl. Phys. $\underline{9}$, 2123 (1976).

56. M. Stimler, Applied Optics $\underline{4}$, 626 (1965).

57. W. W. Anderson, Applied Optics $\underline{5}$, 167 (1966).

58. C. A. Klein, Applied Optics $\underline{5}$, 1923 (1965).

59. C. Schiller and M. Boulou, Philips Tec. Rev. $\underline{35}$, 239 (1975).

60. D. F. Kyser and D. B. Wittry, Proced IEEE $\underline{55}$, 733 (1967).

61. W. E. Ehrenberg and D. King, Proc. Phys. Soc. (London) $\underline{81}$, 751 (1963).

62. M. J. Berger and S. M. Seltzer in Studies in Penetration of Charged Particles into Matter, NBS Publication 1133 (National Research Council, Washington, D.C., 1964) pp. 205-268.

63. G. Shinoda, K. Murata, and R. Shimizu in: Quantitative Electron Probe Microanalysis, K. F. J. Heinrich, ed., National Bureau of Standards Special Publication 298, Washington, D.C. (9168) p. 155.

64. B. P. Nigam, M. K. Sundaresan, T. Y. Wu, Phys. Rev. 115, 491 (1959).

65. V. E. Cosslett and R. N. Thomas, Brit. J. of Appl. Phys., 15, 883 (1964).

66. J. M. Hammersley and D. C. HAndscomb, Monte Carlo Methods, Methuen and Co. Ltd., London (1964).

67. H. A. Bethe, Ann. Phys. (Leipz) 5, 325 (1930).

68. F. Rohrlich and B. C. Carlson Phys. Rev. 93, 38 (1954).

69. A. Nelms, Energy Loss and Range of Electrons and Positrons, NBS Circular 577 (1956).

70. M. L. Cone, R and D Status Report for Project No. 2306-R2-70, Nov. 1977.

71. R. U. Martinelli and C. C. Wang, J. of Appl. Phys. 44, 3350 (1973).

72. J. P. McKelvey, Solid State and Semiconductor Physics, Harper and Row, New York (1966).

73. J. Vilms and W. E. Spcier, J. of Appl. Phys. 36, 2815 (1965).

74. Private communication from Y. K. Yeo.

75. A. C. Hindmarsh, Gear: Ordinary Differential Equation System Solver, Dec. 1974 UCID-30001 Computer Documentation, Lawrence Livermore Laboratory.

76. R. G. Hunsperger, R. G. Wilson and D. M. Jamba, J. Appl. Phys. 43, 1318 (1972).

77. P. W. Yu and Y. S. Park, Appl. Phys. Ltrs. 30, 14 (1977).

78. P. W. Yu and Y. S. Park, J. Appl. Phys. 48, 2434 (1977).

79. P. W. Yu, J. Appl. Phys. 48, 5043 (1978).

80. R. Zölch, H. Ryssel, H. Kranz, H. Reichl, and I. Ruge in Ion Implantation in Semiconductors, S. Namba Ed., Plenum Press, New York (1976) p. 593.

81. P. A. Sullivan, Hughes Research Laboratories, Technical Report AFAL-TR-72-391, Jan 1973, AD907498.

82. Operating Manual for Model LT-3-110 Liquid Transfer Heli-Tran Refrigerators, Air Products and Chemicals, Inc., Allentown, Pennsylvania.

83. J. E. Stangel, Unpublished thesis, Wright-Patterson Air Force Base, Ohio: Air Force Institute of Technology (Dec 1974).

84. R. P. Lyons, Unpublished thesis, Wright-Patterson Air Force Base, Ohio: Air Force Institute of Technology (Dec 1974).

85. Private communication from Y. S. Park.

86. H. J. Queisser and C. S. Fuller, J. Appl. Phys. 37, 4895 (1966).

87. E. W. Williams, Brit. J. Appl. Phys. 18, 253 (1967).

88. E. W. Williams and H. B. Bebb in Semiconductors and Semimetals, Vol. 8, Academic Press, New York (1972).

89. T. C. Lee and W. W. Anderson, Solid State Commun. 2, 265 (1964).

90. M. S. Lin, K. Gamo, K. Masuda, and S. Namba, Jap. J. of Appl. Phys. 15, 53 (1976).

91. D. J. Ashen, P. J. Dean, D. T. J. Hurle, J. B. Mullin, and A. M. White, J. Phys. Chem. Solids 36, 1041 (1975).

92. E. H. Bogardus and H. B. Bebb, Phys. Rev., 176, 993 (1968).

93. W. P. Dumke, Phys. Rev., 132, 1998 (1963).

94. D. M. Eagles, J. Phys. Chem. Solids 16, 76 (1960).

95. L. S. Birks, Electron Probe Microanalysis, Interscience Publishers, New York (1963).

96. Z. Nagy, Z. Samsoni, and K. Benkö, Spectrochimica Acta, 10, 2057 (1963).

97. J. Vilms and W. E. Spicer, J. Appl. Phys. 36, 2815 (1965).

98. D. E. Bolger, J. Franks, J. Gordon and J. Whitaker, 1966 Symp. on GaAs, Reading, Sept 1966.

99. G. A. Acket and J. Scheer, Solid St. Electron 14, 167 (1971).

100. D. Redfield and M. A. Afromowitz, Appl. Phys. Ltrs. 11, 138 (1967).

101. L. Jastrzebski, J. Lagowski, and H. C. Gatos, Appl. Phys. Ltrs. 27, 537 (1975).

102. S. Y. Chiang and G. L. Pearson, J. of Luminescence, 10, 313 (1975).

103. C. J. Hwang, Phys. Rev., 180, 827 (1969).

104. L. N. Kurbatov, N. N. Mochalkin, and A. D. Britov, Soviet Physics-Semiconductors 4, 47 (1970).

105. S. G. Bishop. J. Comas, S. Sundaram, and B. D. McCombe, Appl. Phys. Ltrs., 31, 845 (1977).

106. B. Monemar and J. M. Blum, J. Appl. Phys. 48, 1529 (1977).

107. M. D. Sturge, Phys. Rev. 127, 768 (1962).

108. P. K. Chatterjee, K. V. Vaidyanathan, M. S. Durschlag, and B. G. Streetman, Solid State Commun., 17, 1421 (1975).

Appendix A

LSS RANGE STATISTICS FOR MAGNESIUM
IN GALLIUM ARSENIDE

SUBSTRATE PARAMETERS-

	GALLIUM	ARSENIDE
Z	31	33
M	69.720	74.920
N	.2214E+23	.2214E+23
RHO/R	.7747E+01	.7273E+01
EPS/E	.1668E-01	.157.E-01
CNSE	.1650E+02	.1656E+02
MU	2.958	3.082
GAMMA	.7658	.7399
SNO	.3023E+03	

ION-MAGNESIUM

Z	12
M	24.312

CROSS SECTION SUB. E= 7.00
ELECTRONIC CROSS SECTIONS OF
LINDHARD,SCHARFF,SCHIOTT

| ENERGY (KEV)	PROJECTED RANGE (MICRONS)	PROJECTED STANDARD DEVIATION (MICRONS)	RANGE (MICRONS)	STANDARD DEVIATION (MICRONS)	NUCLEAR ENERGY LOSS (KEV/MICRON)	ELECTRONIC ENERGY LOSS (KEV/MICRON)
10	.0127	.0171	.0285	.0092	.7656E+03	.1502E+03
20	.0222	.0140	.0407	.0135	.3752E+03	.1492E+03
30	.0321	.0190	.0572	.0182	.3733E+03	.1627E+03
40	.0417	.0233	.0748	.0224	.3656E+03	.2110E+03
50	.0515	.0266	.1119	.0263	.3523E+03	.2354E+03
60	.0616	.0303	.1260	.0299	.3727E+03	.2504E+03
70	.0714	.0342	.1357	.0341	.3655E+03	.2741E+03
80	.0855	.0383	.1522	.0366	.3030E+03	.3100E+03
90	.0952	.0425	.1685	.0399	.2201E+03	.3165E+03
100	.1029	.0461	.1847	.0429	.2201E+03	.3335E+03
110	.1133	.0487	.2006	.0497	.2310E+03	.3463E+03
120	.1237	.0530	.2164	.0463	.2725E+03	.3554E+03
130	.1342	.0563	.2329	.0508	.2441E+03	.3503E+03
140	.1447	.0595	.2---	.0533	.2771E+03	.3475E+03
150	.1552	.0627	.2527	.0559	.2075E+03	.3765E+03
160	.1657	.0653	.2774	.0578	.2165E+03	.4213E+03
170	.1763	.0695	.2425	.0599	.2165E+03	.3475E+03
180	.1868	.0718	.3077	.0620	.2266E+03	.4755E+03
190	.1977	.0746	.3225	.0639	.2230E+03	.4588E+03
200	.2079	.0774	.3370	.0658	.2176E+03	.4717E+03
220	.2289	.0827	.3505	.0703	.1972E+03	.4972E+03
240	.2497	.0876	.3752	.0723	.1255E+03	.5262E+03
260	.2703	.0922	.4425	.0751	.1695E+03	.5372E+03
280	.2909	.0967	.4755	.0772	.1565E+03	.5775E+03
300	.3115	.1011	.5019	.0806	.1565E+03	.5832E+03
320	.3321	.1054	.5286	.0832	.1942E+03	.5105E+03
340	.3526	.1094	.5535	.0855	.1275E+03	.6105E+03
360	.3731	.1134	.5782	.0878	.1247E+03	.6322E+03
380	.3935	.1172	.5757	.1004	.1721E+03	.6507E+03
400	.4141	.1206	.5622	.1039	.1292E+03	.7097E+03
420	.4440	.1253	.5922	.1059	.1192E+03	.6705E+03
440	.4541	.1277	.6765	.1093	.1125E+03	.7154E+03
460	.4740	.1309	.7001	.1120	.1665E+02	.7305E+03
480	.4937	.1340	.7233	.1142	.9412E+02	.7--5E+03
500	.5132	.1359	.7593	.1163	.1721E+03	.7524E+03
550	.5609	.1438	.7795	.1100+	.1039E+03	.6124E+03
600	.6070	.1499	.8343	.1059	.1491E+03	.8175E+03
650	.6514	.1555	.8509	.1094	.1451E+03	.6019E+03
700	.6953	.1603	.9351	.1120	.1005E+03	.3--2E+03
750	.7386	.1655	.9001	.11-2	.2915E+03	.9153E+03
800	.7612	.1705	1.0368	.1163	.9412E-02	.9463E+03
850	.8233	.1743	1.0945	.1182	.3915E+02	.37255E+03
900	.8648	.1790	1.1516	.1199	.3765E+02	.10016E+4
950	.9055	.1829	1.1756	.1210	.9125E+02	.10264E+4
1000	.9457	.1865	1.2212	.1231	.7745E+02	.10552E+4

117

Appendix B

In order to fit the computer model profile to the 60 keV/5E13 cm^{-2} Mg implanted GaAs sample it was necessary to add two LSS profiles together. This brings up the question as to how well can two peaks be resolved by measuring the L(V) curve. In order to give some insight into this problem a series of L(V) curves for the 60 keV implant were calculated. For these curves the same values of diffusion length, surface recombination velocity and absorption coefficients are used as previously used for the 60 keV implant.

Figure (B-1) shows the results as the first Gaussian is held at 0.0615 micron and the second Gaussian is moved from 0.0615 micron to 3.0 microns. The Gaussians both have the same amplitude and standard deviation as the LSS, 60 keV Mg implant. Two curves are shown in each plot. Where the two can be distinguished the upper curve is the result of two Gaussians. The lower curve is the L(V) curve resulting from a 60 keV, LSS implant. Thus the effect of the second peak can be compared to the LSS profile in each case.

In the initial plot the two Gaussian implant profiles lie on top of one another. Since there is an arbitrary amplitude scaling done on the L(V) curve the two L(V) curves are identical. As the second peak moves farther into the crystal the L(V) curve begins to show the effect of the second peak. With as little as .0635 micron separation of the peaks a significant change in the calculated L(V) curve results. There seems to be an optimal depth at which the two peaks can be resolved. For the values used here it is about 0.5 of a micron depth for the second peak. As the second peak penetrates even deeper into the GaAs, the impact of
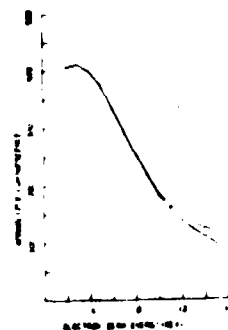
118
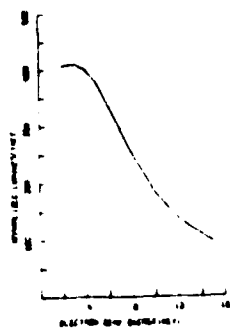
(a) RP1 = .0615 micron
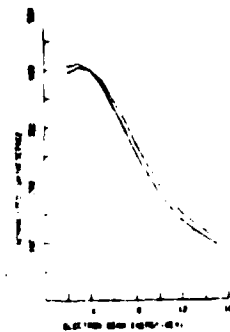
(b) RP1 = .125 micron
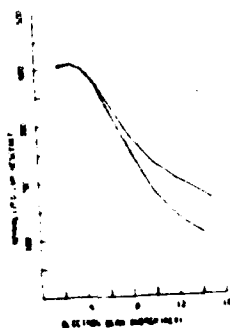
(c) RP1 = .5 micron

(d) RP1 = 1.0 micron

(e) RP1 = 3.0 microns

Fig. B-1 L(V) Curves for Twin Peak Profiles. RP1 = Depth of Second Peak

119

the second peak diminishes. This is because less of the electron beam

penetrates to this depth and more of the luminescence is absorbed before

it reaches the surface. In the limit of 3.0 microns there is no effect

of the second peak reflected in the L(V) curve.

While only one specific set of parameters have been considered here

two general conclusions are evident. First, there is little or no

effect on the L(V) curve for very closely spaced or very widely spaced

peaks. Second, there is an optimal separation of the first and second

peaks at which the L(V) shows the biggest change compared to the single

LSS profile.

Vita

Milton L. Cone was born 27 May 1945, in Sedalia, Missouri. He graduated in 1963 as valedictorian from Holden High School, Holden, Missouri. In 1967, he graduated Cum Laude from the University of Missouri with a Bachelor of Science in Electrical Engineering. Upon graduation, he entered Officers' Training School and received a commission in December 1967 as a 2nd lieutenant in the USAF. In January of 1968, he returned to the University of Missouri under AFIT sponsorship for a Masters of Science degree in Electrical Engineering. Following graduation, he served as an electrical engineer in AFLC at Tinker Air Force Base, Oklahoma, and as an instructor in mathematics and electrical engineering at the USAF Academy. He was then selected to the School of Engineering, Air Force Institute of Technology, in July 1975, as a candidate for the Doctor of Philosophy degree. He is a member of Eta Kappa Nu, Tau Beta Pi and Pi Mu Epsilon honorary societies.

Permanent address: Route 2

Holden, Missouri 64040

REPORT DOCUMENTATION PAGE		READ INSTRUCTIONS BEFORE COMPLETING FORM
1. REPORT NUMBER AFIT/DS/PH/80-1	2. GOVT ACCESSION NO. AD-A090 302	3. RECIPIENT'S CATALOG NUMBER
4. TITLE (and Subtitle) CATHODOLUMINESCENCE CHARACTERIZATION OF ION IMPLANTED GaAs		5. TYPE OF REPORT & PERIOD COVERED Ph.D. Dissertation
		6. PERFORMING ORG. REPORT NUMBER
7. AUTHOR(s) Milton L. Cone, Major, USAF		8. CONTRACT OR GRANT NUMBER(s)
9. PERFORMING ORGANIZATION NAME AND ADDRESS Air Force Institute of Technology (AFIT-EN) Wright-Patterson AFB, Ohio 45433		10. PROGRAM ELEMENT, PROJECT, TASK AREA & WORK UNIT NUMBERS
11. CONTROLLING OFFICE NAME AND ADDRESS Air Force Wright Aeronautical Laboratories (AFWAL/AADR) Wright-Patterson AFB, Ohio 45433		12. REPORT DATE March 1980
		13. NUMBER OF PAGES 132
14. MONITORING AGENCY NAME & ADDRESS(If different from Controlling Office)		15. SECURITY CLASS. (of this report) Unclassified
		15a. DECLASSIFICATION DOWNGRADING SCHEDULE

16. DISTRIBUTION STATEMENT (of this Report)

Approved for public release; distribution unlimited.

17. DISTRIBUTION STATEMENT (of the abstract entered in Block 20, If different from Report)

18. SUPPLEMENTARY NOTES   Approved for public release; IAW AFR 190-17

FREDERIC C. LYNCH, Major, USAF
Director of Public Affairs

19. KEY WORDS (Continue on reverse side if necessary and identify by block number)

Cathodoluminescence   GaAs:Mg
Ion Implantation   Monte Carlo Simulation
Depth Profiling   Depth-dose Curves
GaAs

20. ABSTRACT (Continue on reverse side if necessary and identify by block number)
    Depth-resolved cathodoluminescence was used to study ion implanted GaAs.
This was done in a two step process. First a model for the luminescence from
ion implanted GaAs was developed. This model includes a detailed Monte Carlo
simulation of electrons penetrating into GaAs. The result of this calculation
is a prediction of luminescent intensity as a function of electron beam energy.
This calculation differs from preceeding ones in that the ion implanted profile
is specifically included in the analysis. Second, the model was validated by a
suitable experiment that confirms the theoretical predictions.

DD ₁ FORM ₇₃ 1473   EDITION OF 1 NOV 65 IS OBSOLETE

The luminescence measurements were made on Mg ions implanted into epitaxial GaAs. Mg was chosen since it had not been previously studied in epitaxial GaAs.

The results of this research include the identification of many of the lines in the Mg implanted GaAs spectrum from 1.32 ev to 1.52 ev, a study of the effect of changing the current of the electron beam on the spectra and a comparison of the theoretical and experimental luminescence curves. These results show that changing the current density at the sample surface dramatically changes the spectra and that good agreement exists between the theoretical and experimental luminescence curves.